

Doctoral Dissertation (Censored)

博士論文 (要約)

Study on quantum-dot single-photon sources

hybrid integrated on optical circuits

(光回路上にハイブリッド集積された

量子ドット単一光子源に関する研究)

A Dissertation Submitted for the Degree of Doctor of Philosophy

December 2020

令和2年12月博士(理学)申請

Department of Physics, Graduate School of Science,

The University of Tokyo

東京大学大学院理学系研究科

物理学専攻

Ryota Katsumi

勝見 亮太

Abstract

Single photons are very promising candidates of carriers for quantum information processing. A powerful approach for future scalable quantum photonic devices is integrated quantum photonics by leveraging the strength of mature modern photonic integrated circuits (PICs) technologies. For future quantum applications based on single photons, however, it is vital to introduce single-photon sources (SPSs) which are able to deterministically operate with pure and indistinguishable single-photon generation. Among the various SPSs, the use of semiconductor quantum dots (QDs) is highly promising because they have been shown to fulfill these stringent requirements imposed on SPSs. In this context, the development of QD-based SPSs on PICs is attractive for constructing large-scale integrated quantum optical circuits. Several techniques have been developed for the hybrid integration of QD SPSs onto PICs based on various material platforms, including silicon photonics, and silicon nitride photonics.

However, there remain lots of challenges in the hybrid integrated QD SPSs. One of the most significant issues is the low coupling efficiency of single photons into the photonic waveguide. Toward the scalable operation of quantum optical circuits, it is essential to realize highly efficient coupling of single photons into the optical circuits. Efficient use of waveguide-coupled single photons is also crucial. In addition, the efficient interface of integrated quantum optical circuits with optical fibers is of great importance to realize fiber-based long-distance quantum photonic networks.

Another significant issue is the compatibility of hybrid integration technology with current mature PIC platforms. Particularly, silicon photonics is a powerful platform for large-scale PICs using advanced complementary-metal-oxide-semiconductor (CMOS) technology. Silicon photonics also provides various well-developed nanophotonic elements that allow us to construct highly functional and robust integrated quantum optical circuits. However, the hybrid integration of QDs is inherently difficult and often lacks compatibility with current CMOS technology.

Spectral and spatial randomness inherent in QDs is also the challenge. For the practical quantum applications, the integration of multiple identical SPSs is impor-

tant to perform two-photon interference using them on chip. However, the QD's random emission property hinders the implementation of desirable QD SPSs on preferred locations of a PIC.

To overcome these major challenges in QD SPSs, this thesis presents original research works on QD SPSs hybrid integrated on optical circuits toward scalable and advanced integrated quantum photonics. To solve the issues mentioned above, a deep investigation of transfer printing technology has been done. This technique is based on the pick-and-place manner using an adhesive and transparent rubber stamp.

Firstly, the theoretical work for an efficient QD SPS structure is presented. Since transfer printing allows the individual fabrication of each optical component, it is possible to design on-chip SPS structure flexibly. The numerical simulations show that our SPS structure's design enables the coupling of single-photon emission from QDs into the waveguide over 99%. Notably, this near-unity efficiency can be maintained even under the position misalignment of transfer printing or even under the material change.

Secondly, the hybrid integration technique based on transfer printing is presented. To perform hybrid integration of QD SPSs with high position accuracy at high yield, lots of efforts are paid to develop transfer printing technology. Experimentally, the device exhibits efficient coupling of single photons with coupling efficiency over 70%. Our transfer printing approach further makes it possible to integrate two SPSs into a single photonic waveguide. Details of the nanofabrication technique required for this whole study are also introduced.

Thirdly, hybrid integration of a QD SPS on a silicon PIC processed by a CMOS foundry is studied. Since the integration of photonic devices is based on van der Waals adhesion, transfer printing enables us to assemble QD SPSs after the completion of the entire CMOS process. To unveil a method to integrate QD SPSs on a silicon CMOS chip, QD SPSs are transfer-printed onto a dry-etched glass surface of a CMOS chip. It is confirmed that integrated QDs are cooled down even on a foundry-processed silicon chip. Intensity correlation measurement also verifies single-photon generation from an integrated QD on silicon with $g^{(2)}(0) = 0.30$. Its efficient waveguiding in the CMOS-processed photonic chip with the coupling efficiency of $\sim 70\%$ is also confirmed in experiment.

Fourthly, in-situ fine wavelength tuning of QD SPSs on a CMOS-processed silicon PIC is demonstrated. Optically-driven heater pads are utilized to tune the emission wavelengths of integrated QDs thermally. Transfer printing enables us to integrate these functional components as well as QD SPSs in a simple pick-and-place manner. The obtained maximum possible tuning range of QD emission wavelength is 0.9 nm.

Furthermore, this approach is leveraged for the spectral matching of two dissimilar integrated QD sources on the same silicon CMOS chip, which is a significant step toward on-chip two-photon interference with dissimilar QD-based SPSs.

Fifthly, the efficient output of QD SPSs hybrid integrated on a silicon waveguide terminated with a PhC mirror is examined. The numerical calculation reveals that our designed SPS structure can support the QD-to-waveguide coupling efficiency over 99% with unidirectional output. By employing a subwavelength grating structure as a waveguide, the SPS structure can maintain near-unity output efficiency in the waveguide, even considering the finite positioning accuracy accompanied by transfer printing. Experimentally, the overall output efficiency of the QD emission in the waveguide is estimated to be $\sim 74\%$. Observation of single-photon generation from an integrated QD is also performed with $g^{(2)}[0]$ value of 0.28.

Sixthly, fiber-pigtailed QD SPSs hybrid integrated on a silicon CMOS chip is presented. To achieve the efficient fiber output of single photons, a telecom QD SPS is integrated on a fiber-pigtailed silicon CMOS chip using transfer printing, which enables us to take full advantage of mature silicon photonics components. Observation of Purcell-enhanced QD emission through the optical fiber is demonstrated with the single-photon generation in the fabricated device. Fabrication technique of InP-based photonic crystal nanobeam cavities is also introduced.

Finally, the conclusion of this thesis is presented. An outlook for prospects is also discussed.

Acknowledgment

This thesis compiled the research content of the Ph.D. course in the Department of Physics, Graduate School of Science, University of Tokyo.

First of all, I would like to express my deepest and sincerest appreciation to my supervisor, Prof. Hidefumi Akiyama, for his fruitful discussions and advice throughout my Ph.D. course. He supported my study life whole with the Ph.D. course, enabling me to devote myself to my own research. He also provided me great opportunities to attend many domestic and international conferences, which allows me to see my research field from a better viewpoint. All his support encouraged and motivated me to concentrate on my researches. I really appreciate his warm mentorship.

I owe a deep debt of gratitude to Prof. Satoshi Iwamoto for all his earnest support throughout my Ph.D. thesis. He always gave me clear, insightful, and thoughtful advice based on his keen insight, broad knowledge, and a great variety of his experience. He also offered me an outstanding research environment and precious opportunities, such as interacting with other research groups and visiting overseas laboratories related to my research topics. I have learned a lot from his attitude and passion for the research and obtained variable experiences under his leadership. Without his patient guidance and mentorship, this work would not be completed.

I want to express my deep gratitude to Prof. Yasuhiko Arakawa for his support and advice. He was initially my supervisor during my master course and has given precious comments and the excellent research environment necessary for conducting my research. His instruction and valuable feedback helped me to do my research smoothly. He also provided me ample opportunities to join many domestic and international conferences, enabling me to see my research area from a better perspective. I am really grateful for his generosity.

I would like to strongly express my special thanks to Prof. Yasutomo Ota for his technical support and fruitful advice. He has always been my role-model of the researcher: he covers broad research fields in detail and has a wide variety of experiences regarding nano-photonics. I benefited from many discussions with him not only about my research targets but also about many other interesting topics related to integrated photonics. He always supported me in making a strategy of experiments, writing papers, blushing up presentations, etc. I believe that it would be impossible for me to achieve this research without his excellent guidance.

I show my sincere gratitude to my close collaborators in Arakawa-Iwamoto group. Dr. Masahiro Kakuda provided me a lot of high-quality quantum dot samples. Dr. Kazuhiro Kuruma and Dr. Takeyoshi Tajiri taught me the basics of nano-fabrication and characterization of my samples. Dr. Alto Osada gave me a lot of helpful advice about the physics of cavity quantum electrodynamics and optical measurement. Mr. Wenbo Lin, who is the same grade as me, provided me with technical support regarding numerical simulations. Mr. Takuto Yamaguchi helped me do the dry etching of silicon. I also want to acknowledge Dr. Kazuya Takemoto and Dr. Toshiyuki Miyazawa for helpful comments and suggestions. Besides, I would like to thank Prof. Mark Holmes, Mr. Masao Nishioka and Dr. Satomi Ishida for their technical and mental supports.

I would like to thank the University of Kassel group led by Prof. Mohamed Benyoucef in collaboration with Prof. Johann Peter Reithmaier, for providing me with high-quality InP/InAs quantum dot samples.

Moreover, I want to acknowledge all of my former and current colleagues in Arakawa and Iwamoto group: Prof. Takeshi Kamijoh, Dr. Munetaka Arita, Dr. Toshio Saito, Mr. Koya Otokozawa, Dr. Jun Tatebayashi, Dr. Shun Takahashi, Dr. Takeo Kageyama, Dr. Kenji Kamide, Dr. Jinkwan Kwoen, Dr. Bongyong Jang, Dr. Katsuyuki Watanabe, Dr. Takahiro Doe, Dr. Natalia Morais, Dr. Chee Fai Fong, Dr. Gao Kang, Dr. Ingi Kim, Dr. Natsuko Ishida, Dr. Tianji Liu, Dr. Feng Tian, Mr. Hirofumi Yoshikawa, Mr. Huy Vo Quoc, Mr. Akihito Tamada, Mr. Joohang Lee, Mr. Takeshi Ishida, Mr. Fumio Maehara, Ms. Siyuan Gao, Mr. Sangmin Ji, Mr. Hironobu Yoshimi, Mr. Sun Zhaoyin, Mr. Tatsuya Takemori, Mr. Pholsen Natthajuks, Mr. Ryosuke Miyazaki, Ms. Yeting Yang, Mr. Mei Yang and Ms. Sun Xiaoxiao.

I would like to thank Ms. Ritsuko Nara, Ms. Miwa Ouchi, Ms. Miwa Kitagawa in Arakawa and Iwamoto group and Ms. Tomoko Aida in Akiyama group for their kindness and help regarding the accounting processes, office procedure and so on.

I gratefully acknowledge financial support from the Japan Society for the Promotion of Science (JSPS) and Advanced Leading Graduate Course for Photon Science (ALPS). I also thank my secondary supervisor of the ALPS course, Prof. Takao Someya, for fruitful discussions.

Finally, I would like to offer my special gratitude to my family and friends, especially my twin brother, mother, and father for their generous support.

Contents

Abstract	i
Acknowledgment	v
1 Introduction	1
1.1 Research background	1
1.2 Research objective	4
1.3 Outline of this thesis	5
2 Fundamentals of quantum-dot single photon source in photonic crystal cavity	7
2.1 Quantum dot (QD)	7
2.1.1 Epitaxial growth of QD	7
2.1.2 Energy level and excitation schemes of QD	8
2.2 Purcell effect	10
2.3 Photonic crystal (PhC)	12
2.4 Photon statistics with second-order correlation function	15
2.4.1 Classical case	16
2.4.2 Quantum case	17
3 Design for integrated single-photon source with near-unity waveguide coupling	21
3.1 Introduction	21
3.2 Transfer printing	21
3.2.1 Principle of transfer printing	22
3.3 Device design for near-unity QD-waveguide coupling	24
3.3.1 Cavity-waveguide coupling efficiency (η)	24
3.3.2 Emitter-cavity coupling efficiency (β)	30
3.4 Direct simulation of $\eta\beta$ using point dipole source	31

3.5	Robustness against misalignment of cavity with respect to waveguide	34
3.6	Simulated coupling efficiency with different material platforms	36
3.7	Summary	37
4	Fabrication and characterization of QD single-photon source transfer-printed on photonic waveguide	39
4.1	Overall integration procedure based on transfer printing	39
4.1.1	Fabrication of GaAs photonic crystal nanobeam cavity	41
4.1.2	Fabrication of GaAs photonic waveguide embedded in glass . .	47
4.2	Transfer printing-based integration of nanocavity on photonic waveguide	50
4.2.1	Home-made transfer printing machine	50
4.2.2	Fabrication of patterned rubber stamp	52
4.3	Optical characterization setup	56
4.4	Optical characterization of waveguide-integrated quantum-dot single-photon source	59
4.4.1	PL image	59
4.4.2	PL spectra from exit port and above cavity	59
4.4.3	Evaluation of experimental cavity-waveguide coupling efficiency (η_{exp})	62
4.4.4	Observation of Purcell enhancement	64
4.4.5	Overall emitter-waveguide coupling efficiency ($\eta_{exp}\beta_{exp}$)	67
4.4.6	Measured evolution of spontaneous emission rate as a function of QD-cavity detuning	68
4.4.7	Observation of single-photon generation	69
4.5	Integration of two QD SPSs on a single chip	70
4.5.1	Single-photon transport under the presence of two cavities on a single waveguide	70
4.5.2	Demonstration of efficient cavity-waveguide coupling	71
4.5.3	Demonstration of efficient emitter-cavity coupling	72
4.5.4	Observation of single-photon generation	72
4.6	Summary	74
5	Hybrid integrated QD single-photon source on silicon CMOS photonic chip	75
5.1	Introduction	75
5.2	Device design for near-unity coupling of QD emission into silicon photonic waveguide	76

5.3	Procedure of integrating QD SPS on silicon CMOS chip based on transfer printing	79
5.3.1	Fabrication of air-bridged GaAs PhC nanobeam cavity	79
5.3.2	Preparation of CMOS-processed silicon photonic waveguide	79
5.3.3	Integration of QD SPS on CMOS-processed silicon waveguide using transfer printing	82
5.4	Optical characterization of QD SPS on CMOS silicon waveguide	85
5.4.1	PL image	85
5.4.2	PL spectra from exit port and above cavity	85
5.4.3	Evaluation of experimental cavity-waveguide coupling efficiency (η_{exp})	88
5.4.4	Observation of Purcell-enhanced QD emission	88
5.4.5	Observation of single-photon generation on silicon	89
5.5	Summary	92
6	In-situ spectral tuning of QD single-photon source on silicon CMOS chip	93
6.1	Introduction	93
6.2	Device structure for on-chip spectral tuning of QD SPS	94
6.3	Fabrication of investigated device structure	96
6.3.1	Preparation of waveguide-integrated QD SPS	96
6.3.2	Integration of laser-driven heater pad using transfer printing	96
6.4	Optical characterization of the fabricated device	99
6.4.1	Optical measurement setup	99
6.4.2	Tunability of integrated QD SPS	100
6.4.3	Single-photon generation under heat tuning	103
6.4.4	Stability of the fabricated device	104
6.5	Spectral matching between dissimilar integrated two QD sources	104
6.6	Summary	108
7	Efficient QD single-photon source transfer-printed on silicon photonic waveguide with unidirectional output	111
8	Fiber-pigtailed QD single-photon source integrated on silicon CMOS chip	127
8.1	Introduction	127
8.2	Device structure for efficient InP based QD SPS on silicon	128
8.2.1	Simulated output efficiency of InP-based QD SPS	128
8.3	Fabrication of InP PhC nanobeam cavity	130

8.3.1	Sample growth of InP slab containing InAs QDs	130
8.3.2	Sputtering SiO ₂ hard mask	130
8.3.3	EB Resist for preparing SiO ₂ hard mask	131
8.3.4	Dry etching SiO ₂ hard mask	131
8.3.5	Dry-etching InP layer	132
8.3.6	Removing EB resist and SiO ₂ hard mask	136
8.3.7	Wet chemical etching	136
8.4	Implementation of pigtail fibers into silicon CMOS chip	137
8.4.1	Dry etching clad while protecting SSCs	137
8.4.2	Implementation of lensed fibers into SSCs	138
8.5	Fabrication of the device using transfer printing	138
8.5.1	Pre-characterization of the InP/InAs QD SPS	140
8.5.2	Transfer printing with improved machine	140
8.5.3	Integration of InP/InAs QD SPS on processed silicon chip . .	141
8.6	Optical characterization of fiber-pigtailed QD SPS	141
8.6.1	PL spectra extracted from optical fibers	144
8.6.2	Observation of Purcell-enhanced QD emission from optical fiber	145
8.6.3	Estimation of total fiber output efficiency of single photons . .	145
8.6.4	Quasi-resonant excitation of integrated QD	146
8.6.5	Observation of single-photon generation	147
8.7	Summary	148
9	Conclusion and future prospect	149
9.1	Conclusion	149
9.2	Future prospect	150
9.2.1	On-chip two-photon interference with dissimilar QD SPSs . . .	150
9.2.2	Automation of transfer printing	151
9.2.3	On-chip boson sampling	152
A	Details of improved transfer printing apparatus	153
A.1	Control panel	155
A.2	Preparation	155
A.3	Operation for pick up	157
A.4	Operation for placement	157
	Bibliography	158
	Research achievements	179

Chapter 1

Introduction

1.1 Research background

The unique property of quantum systems, such as superposition and entanglement, can promise information processing technologies that are inherently more powerful than their classical counterparts, including quantum computing [1], quantum communications [2], and quantum sensing [3]. For all these applications, the starting point is quantum bits (qubits), the elementary unit of information represented by a quantum mechanical two-level system. Many qubit architectures have been under investigation, as represented by a variety of physical systems [4] including atoms [5], trapped ions [6], superconducting circuits [7] and so on. Among these candidates, single photons, single particles of light, are promising to realize quantum information processing applications thanks to their low decoherence, long-distance propagation, multiple available degrees of freedom (e.g., polarization, path, and orbital angular momentum), compatibility with classical photonic technology [8–10]. After decades of intensive theoretical and experimental efforts, the field of quantum photonic information processing has been reaching a critical stage, such as quantum computers and special-purpose quantum information processors which may solve problems that classical computers cannot [11], quantum networks over continental distances [12–14], and loop-hole free Bell tests [15, 16].

To scale up quantum photonic systems, integrated quantum photonics is a particularly desirable technology because they exhibit a huge potential to reach the level of component integration and performance required for quantum information processing. By leveraging the rapid evolution of photonic integrated circuits (PICs), as represented by the current flourish of silicon photonics [17, 18], integrated quantum

photonics enables the chip-scale manipulation of quantum states of light, demonstrating orders of magnitude improvements in component density, optical loss, and phase stability compared to bulky table-top experiments. Such advances have enabled proof-of-principle demonstrations of quantum protocols, including foundational tests of quantum mechanics [19], quantum simulations [20, 21], quantum communications [22], and quantum machine learning [23, 24].

For quantum photonic information processing, one of the fundamental components is a single-photon source (SPS). Toward scalable quantum information processing and other quantum applications, SPSs must fulfill various strict requirements. The main requirements are as follows; (i) Ideal SPSs always emit light pulses that contain only one photon with no vacuum component $|0\rangle$, and such sources are called deterministic SPSs. This criterion is important for secure and high-speed quantum communication as well as for the high success probability of quantum information processing protocols. (ii) Ideal SPSs should also produce light pulses in a pure quantum state of $|1\rangle$. This means that the generated light pulses should not contain more than one photon, which can be characterized by the second-order intensity correlation function $g^{(2)}(0)$. A light pulse with only a quantum state of $|1\rangle$ leads to $g^{(2)}(0) = 0$. The high purity of SPSs guarantees the security of quantum communications and minimizes errors in quantum computation and simulation. (iii) Finally, for most applications in quantum information processing, all photons should be identical regarding the wavelength, pulse width, polarization, and spatiotemporal property (i.e., photons are indistinguishable). This property is key for observing two-photon interference (or so-called Hong-Ou-Mandel interference) at a beam splitter, which is mandatory for many quantum applications, such as the realization of quantum gates.

Currently, most of the demonstrations rely on SPSs based on nonlinear parametric processes, including spontaneous parametric down-conversion (SPDC) [25]. However, for such SPSs, high quality of purity (i.e., very low $g^{(2)}(0)$ value) can be obtained only for very low source brightness: to limit the contribution of multiple photon states, SPDC-based sources are strongly attenuated, resulting in an extremely low mean number of photons. Although several approaches have been proposed to overcome the limitations of purely silicon-based SPSs using spatial [26] and time multiplexing [27], there still remains a difficulty in building a deterministic SPS with these approaches.

An attractive and fascinating solution for this issue is the use of solid-state SPSs based on atom-like systems [28], including colour centers in diamond [29–32], silicon carbide [33, 34], carbon nanotubes [35, 36], and defects in two-dimensional materi-

als [37, 38]. Particularly, semiconductor quantum dots (QDs) are highly promising since they have been proven to generate single photons with excellent properties deterministically [39–41]. For the single-photon purity, several reports of using QDs have demonstrated the single-photon generation of extremely low $g^{(2)}(0)$ values [42–47]. Very recently, a record low $g^{(2)}(0)$ value of 7.5×10^{-5} without any background subtraction or data processing was achieved [48]. Regarding the photon indistinguishability, several demonstrations have achieved measured indistinguishability of photons close to unity thanks to the enhancement of spontaneous emission rates (Purcell effect) based on micropillars [42, 44, 49] and photonic crystals (PhCs) [50–52]. Moreover, there are already several reports of two-photon interference between dissimilar remote QD-based SPSs off chip [53–57]. Recently, two-photon interference using dissimilar QD-based SPSs on the same chip was also demonstrated [58], though the interference was done off chip. Indeed, QD-based SPSs have already shown their premise for quantum key distribution [59], quantum algorithms [60], and boson sampling [61, 62], which is a strong candidate to show “quantum supremacy” by calculating the output distribution of an input arrangement of n bosons in m optical modes after a linear unitary transformation ($m > n$). The very recent bulk-optical experiment of boson sampling demonstrated 20 photons in a 60 mode fixed interferometer using single photons demultiplexed from a QD [63].

In this context, the development of QD-based SPSs on hybrid optical circuits is very promising toward the scalable quantum photonics [64–66]. To date, several techniques have been developed for the hybrid integration of QD SPSs onto PICs based on silicon [67], lithium niobate [68] and silicon nitride photonics [69–72]. In these demonstrations, QD-based SPSs are either directly placed above waveguides or encapsulated inside waveguides. However, there remain lots of issues in the hybrid integrated QD SPSs: (I) single-photon coupling efficiency, (II) compatibility of the integration process with other PIC technology, and (III) inherent randomness in QDs.

- (I) Toward the scalable operation of quantum optical circuits, it is vital to realize near-unity coupling of single photons into the optical circuits. However, the experimental waveguide coupling efficiencies of previously demonstrated hybrid QD SPSs have been limited to below 50%: M. Davanco *et al.*, demonstrated the experimental QD-to-waveguide coupling efficiency of $\sim 20\%$ in InAs/GaAs QDs on a Si_3N_4 waveguide with wafer bonding approach [69]. J. H. Kim *et al.*, demonstrated the coupling efficiency of $\sim 15\%$ in InAs/InP QDs on a Si waveguide with microprobes [67]. I. E. Zadeh *et al.*, demonstrated the coupling efficiency of $\sim 24\%$ in InAs/GaAs QD nanowires with a Si_3N_4 waveguide with

nanomanipulators [70]. Thus, the improvement of single-photon coupling is one critical issue in this field. Besides, there remains a challenge for efficient output of waveguide-coupled single photons, which is essential for realizing scalable and complex quantum photonic network.

- (II) To exploit the strength of mature PIC technologies, the hybrid integration technique should be compatible with various PIC platforms. For example, silicon photonics is a powerful platform for large-scale PICs using advanced complementary-metal-oxide-semiconductor (CMOS) technology. However, the process of the hybrid QD integration often lacks compatibility with such sophisticated CMOS technology: introduction of hybrid integration processes (e.g., conventional wafer bonding [69]) into existing CMOS foundry platforms is generally difficult since it is challenging to modify CMOS foundry processes solely for new materials. Thus, the development of hybrid integration techniques friendly with high-end PIC technology is of great importance.
- (III) Regarding the property of QDs, they inherently have spectral and spatial randomness. Such random properties will hinder the implementation of QD SPSs with desirable emission property on preferred locations of a PIC. In addition, the implementation of SPSs on chip with perfect spectral matching is also required for scalable quantum photonic applications, where the operation relies on the interference of photons in the optical circuits.

1.2 Research objective

The main object of this thesis is to overcome these major challenges in QD SPSs based on hybrid integrated quantum photonics. To this end, the new hybrid integration technique called transfer printing is deeply investigated. This approach is the pick-and-place technique using an adhesive and transparent rubber stamp. Based on this technique, we mainly address the following three main issues in this thesis.

Firstly, the demonstration of efficient QD-waveguide coupling is addressed both theoretically and experimentally. Since the transfer printing approach is based on the pick-and-place operation, each required optical component can be separately prepared, allowing us to design the SPS structure for efficient single-photon coupling at will. The numerical calculation shows that our designed SPS structure enables the near-unity single-photon coupling from QDs into photonic waveguides. For the

hybrid integration with high position accuracy at high yield, much effort has been paid to build a transfer printing apparatus. Experimentally, the devices, which are fabricated with our transfer printing machine, exhibit efficient single-photon coupling efficiency. Moreover, the improvement of single-photon output efficiency on chip is also addressed with the unidirectional light output. By further elaborating on designing the SPS structure, the efficient single-photon output is possible even under the finite position misalignment of transfer printing.

Secondly, the process compatibility of our transfer printing technique with other PIC platforms is investigated. Since transfer printing relies on van der Waals force, the integration of QD SPSs can be done after finishing the entire CMOS process. We develop QD SPSs hybrid integrated on a CMOS silicon optical circuits by employing transfer printing. Integrated QDs can also be cooled down enough to emit single photons on a foundry-processed silicon chip, showing the possibility to combine QD SPSs and highly functional silicon quantum photonics. In addition, for the efficient fiber output of single photons, the efficient fiber-pigtailed QD SPSs on a silicon PIC is addressed by taking the full advantage of well-developed nanophotonic components in silicon photonics.

Finally, on-chip QD SPSs with spectral tuning is studied. Transfer printing allows for the on-chip hybrid integration of not only QD SPSs but also required components for wavelength tuning.

In this thesis, we show our original experimental and theoretical works on the above issues. The original contributions of the author to the field are briefly summarized in the following thesis outline.

1.3 Outline of this thesis

Chapter 2 introduces the fundamentals of QDs, SPSs, and PhCs. The derivation of the Purcell effect is also described.

In chapter 3, theoretical works for achieving near-unity single-photon coupling from QDs into photonic waveguides are shown.

Chapter 4 describes the experimental demonstrations of integrated QD SPSs on glass-cladded photonic waveguides for efficient single-photon waveguide coupling. The development of the transfer printing technique is presented. Characterization methods of the completed device are also shown. Efficient single-photon coupling into

the GaAs waveguide is experimentally demonstrated together with the integration of two SPSs into a single GaAs photonic waveguide.

Chapter 5 is devoted to the hybrid integration of a QD SPS on CMOS silicon photonics platforms. Hybrid integration is performed using transfer printing, which enables us to assemble them after the completion of the entire CMOS process. To uncover a way to integrate QD SPSs on a silicon CMOS chip, QD SPSs are transfer-printed onto a dry-etched glass surface of a CMOS chip. We confirm that integrated QDs are cooled down even on a foundry-processed silicon chip. Single-photon generation is successfully observed from the integrated QD together with its efficient waveguide coupling.

Chapter 6 presents in-situ fine wavelength tuning of QD SPSs integrated on a CMOS-processed silicon waveguide. Emission wavelengths of the integrated QDs are thermally controlled with optically-driven heating pads, which are additionally integrated onto the silicon-integrated QD SPS. All these hybrid integration processes are done by using transfer printing. With this approach, spectral matching is experimentally demonstrated between two dissimilar QD sources integrated on a silicon chip, which is an important step toward on-chip two-photon interference utilizing dissimilar integrated QDs.

Chapter 7 shows the unidirectional output of QD SPSs hybrid integrated on a silicon waveguide toward the efficient photon output. By terminating the waveguide with PhC mirrors, the unidirectional output of QD emission coupled to the waveguide is demonstrated. By employing a subwavelength grating (SWG) waveguide, it is confirmed that we can mitigate the required positioning accuracy of QD SPSs to support the near-unity efficiency of the single-photon output in the waveguide. The designed structure is fabricated using transfer printing. Experimentally, efficient coupling of QD emission into the silicon SWG waveguide is demonstrated with the unidirectional output of QD emission. Single-photon generation is also verified from the integrated QD.

Chapter 8 describes a fiber-pigtailed QD SPS based on hybrid silicon quantum photonics toward efficient fiber output of single photons. The efficient extraction of QD emission on chip through the optical fiber is addressed. Transfer printing even allows for the integration of a pre-characterized QD SPS onto the silicon CMOS chip that has been already implemented with fiber pigtails for the efficient fiber-to-waveguide coupling. The Observation of Purcell-enhanced QD emission and single-photon emission from the integrated QD are demonstrated through the pigtailed fiber in the fabricated device.

Chapter 9 presents the conclusion of this thesis. An outlook for future prospects is also discussed.

Chapter 2

Fundamentals of quantum-dot single photon source in photonic crystal cavity

In this chapter, we introduce the fundamentals of quantum dots (QDs), photonic crystals (PhCs), and single-photon sources (SPSs). We start from the basic contents of self-assembled QDs. Purcell effect is also introduced to describe the enhancement of spontaneous emission of QDs inside the cavity. We then discuss the basic theory of photonic band gap of 1D PhCs. Finally, we discuss how to evaluate the quantum nature of light.

2.1 Quantum dot (QD)

A QD consists of a lower bandgap semiconductor (e.g., InAs and InGaAs) embedded in a semiconductor with a higher bandgap (e.g., GaAs and InP). This results in the confinement of the electron in all spatial dimensions due to the band offsets, which is strong enough to provide atom-like discrete energy levels for a trapped carrier. Since the two pioneers, Y. Arakawa and H. Sakaki, pointed out the significance of the structure in the field of laser applications in 1982 [73], intensive studies have been done for QDs, especially as excellent SPSs.

2.1.1 Epitaxial growth of QD

To form the semiconductor QDs, the common approach is the Stranski-Krastanov growth using a molecular beam epitaxy (MBE) system or metal-organic chemical

vapor deposition (MOCVD) system. Here semiconductor QDs based on MBE are discussed. When the lattice mismatch between two semiconductor materials is sufficiently high, the accumulation of strain after a certain thickness results in the formation of 3D islands rather than 2D layers. InAs is one of the typical materials used for growing QDs on GaAs substrates. When a layer of InAs is deposited on a GaAs surface, the increasing strain only allows the growth of a thin 2D layer (wetting layer). A transition between 2D and 3D growth occurs when the thickness of InAs reaches a critical point, forming 3D InAs islands on the GaAs surface. For the case of InAs/GaAs QDs, the lattice-constant mismatch is 7%. A GaAs capping layer is subsequently grown on top, which is necessary for the 3D quantum confinement.

2.1.2 Energy level and excitation schemes of QD

The schematic band structure of a QD is depicted in Fig. 2.1 [74]. The small size of the QD and lower band gap form quantized discrete levels (here, we only show p- and s-shells). Initially, electrons are in the valence band and holes in the conduction band. When optically pumped, an electron can be excited to the conduction band, leaving a hole in the valence band. This electron-hole pair can be trapped by the QD, relaxing to the lowest energetic state called s-shell. When confined into the QD, the electron-hole pair form a new quasi-particle called exciton state (X) due to the Coulomb interactions. Radiative decay of X leads to the emission of a photon. In practice, the QD can be excited to a higher excited state leading to a biexciton (XX) state (two electrons and two holes) or a higher multi-excitonic state. For an odd number of particles in the QD, charged excitons are formed. The simplest charged exciton is a trion (X_{\pm}), which consists of one exciton and a single electron (X_{-}) or hole (X_{+}).

The optical excitation schemes are typically distinguished by the used wavelength of the excitation laser. A standard and easy excitation method is the above band excitation (or non-resonant excitation), where laser energy is above the bandgap of the barrier material. Charge carriers are created in the vicinity of the QD and captured by the wetting layer, subsequently relaxing into the high energy states of the QD further and then into the ground state forming exciton. The advantage of this above band excitation is that the laser wavelength is well separated from that of QD photons, allowing us to extract only single photon emission with spectral filtering. However, the high excitation energy causes the creation of many charge carriers in the QD vicinity, resulting in electromagnetic fluctuations. These charge fluctuations in the solid-state environment, together with phonon interaction introduce decoherence to the emitted photons and homogeneous linewidth broadening.

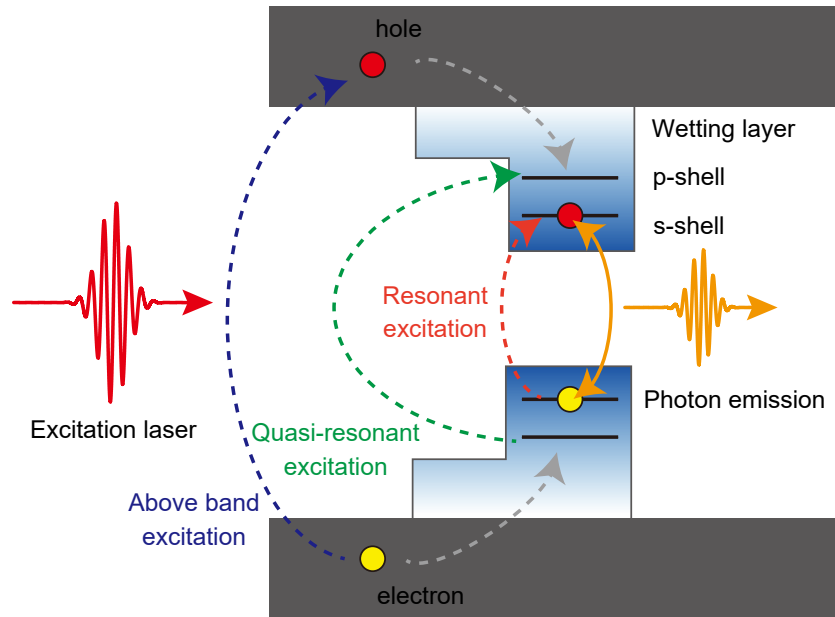


Figure 2.1: The schematic band structure of a QD.

A way to overcome this decoherence issue is the quasi-resonant and resonant excitation of a single QD transition. In quasi-resonant excitation, the excitation laser is tuned near the emission line of a QD, and excites the QD on transition with a higher excited state (e.g., p-shell), while the single photon emission takes place from s-shell following a fast non-radiative decay. Large laser power may be required since the absorption cross section of a single QD is small. In this scheme, it is possible to excite only one single QD, so the filtering has to be done only for the excitation laser. Besides, dephasing processes should be drastically reduced since the charge carriers are exclusively generated within the desired QD.

In resonant excitation, the excitation laser exactly matches the QD transition, and excites the QD into the first excited state (s-shell). Since there is no additional relaxation process from a higher excited state, the high indistinguishability of the excited state can be expected. However, resonant excitation is challenging to perform practically due to the difficulty of filtering out the excitation laser from QD emission. Thus this scheme requires more sophisticated filtering techniques compared to the above band excitation scheme commonly based on spatial or polarization filtering.

2.2 Purcell effect

Spontaneous emission rates of an atom placed in a resonant cavity can be enhanced over its free-space value, as was first predicted by E. M. Purcell some 70 years ago [75]. In this section, we show the essential derivation of Purcell effect. Assuming that the linewidth of the dipole emission is much narrower than that of the cavity resonant mode, we can calculate the spontaneous emission rate simply by using Fermi's golden rule. In Fermi's golden rule, the transition rate ($|i\rangle \rightarrow |f\rangle$) is given by

$$\Gamma = \frac{2\pi}{\hbar} \rho(\hbar\omega) |\langle f | \mathbf{d} \cdot \mathbf{E}(\mathbf{r}_e) | i \rangle|^2, \quad (2.1)$$

where $|i\rangle$ and $|f\rangle$ are the initial and final state of the system and $\rho(\hbar\omega)$ is the available density of final states. \mathbf{d} is the dipole moment at $\mathbf{r} = \mathbf{r}_e$ with the emitter frequency of ω .

For 3D free space, we have the photon density of states

$$\rho_{free}(\hbar\omega) = \frac{\omega^2 n^3}{\pi^2 \hbar c^3} V, \quad (2.2)$$

where V is a volume of free-space modes and n is a refractive index. The optical electric field in this space $\mathbf{E}(\mathbf{r}, t)$ takes the following form;

$$\mathbf{E}(\mathbf{r}, t) = \mathbf{E}(\mathbf{r}, \omega) e^{-i\omega t} + \mathbf{E}^*(\mathbf{r}, \omega) e^{i\omega t} \quad (2.3)$$

$$\mathbf{E}(\mathbf{r}, \omega) = i E_{max} \mathbf{f}(\mathbf{r}), \quad (2.4)$$

where $E_{max} = E(\mathbf{r}_{max})$ is the maximum amplitude of $\mathbf{E}(\mathbf{r}, t)$ and $\mathbf{f}(\mathbf{r})$ is the normalized function satisfying $|\mathbf{f}(\mathbf{r} = \mathbf{r}_{max})| = 1$. Here, the time-averaged storage energy of electromagnetic field for a single photon equals to $\hbar\omega$ (the energy of single photon);

$$\frac{1}{2} \int_V d^3 \mathbf{r} n^2(\mathbf{r}) (\varepsilon_0 \mathbf{E}^2 + \mu_0^{-1} \mathbf{B}^2) = 2\varepsilon_0 \int_V d^3 \mathbf{r} n^2(\mathbf{r}) |\mathbf{E}(\mathbf{r}, \omega)|^2 = \hbar\omega. \quad (2.5)$$

We note that from Maxwell equations in isotropic media, we can obtain $\varepsilon_0 \mathbf{E}^2 = \mu_0^{-1} \mathbf{B}^2$. For a plane wave $\mathbf{f}(\mathbf{r}) = \hat{\mathbf{r}} e^{i\mathbf{k} \cdot \mathbf{r}}$, we obtain

$$E_{max}^{free} = \sqrt{\frac{\hbar\omega}{2\varepsilon_0 n^2 V}}. \quad (2.6)$$

When we take into account for a factor of 1/3 for the angular average of the atomic dipole moment, we obtain

$$|\mathbf{d} \cdot \mathbf{E}|^2 = |\mathbf{d}|^2 |\mathbf{E}^{free}|^2 / 3, \quad (2.7)$$

Then the spontaneous emission rate in free space is expressed as follows;

$$\begin{aligned}
 \Gamma_{free} &= \frac{2\pi}{\hbar} \rho_{free}(\hbar\omega) |\langle f | \mathbf{d} \cdot \mathbf{E}(\mathbf{r}_e) | i \rangle|^2 \\
 &= \frac{2\pi}{\hbar} \frac{\omega^2 n^3 V}{\pi^2 \hbar c^3} \frac{|\mathbf{d}|^2 |\mathbf{E}^{free}|^2}{3} \\
 &= \frac{2\pi}{\hbar} \frac{\omega^2 n^3}{\pi^2 \hbar c^3} \frac{|\mathbf{d}|^2}{3} \frac{\hbar\omega}{2\varepsilon_0 n^2}.
 \end{aligned} \tag{2.8}$$

Next we focus on cavities. We consider a single cavity mode with a resonant cavity frequency of ω_{cav} and FWHM of the cavity $\Delta\omega$. For a cavity, the optical field cannot be treated as plane waves, so we alternatively employ an effective mode volume V_{eff} . When defining $n_{max} = n(\mathbf{r}_{max})$ (\mathbf{r}_{max} : location of the electrical field at its maximum), we can introduce

$$\begin{aligned}
 V_{eff} &= \frac{\int_V n^2(\mathbf{r}) |\mathbf{E}(\mathbf{r}, \omega)|^2 d^3\mathbf{r}}{n_{max}^2 E_{max}^2} \\
 &= \frac{\int_V n^2(\mathbf{r}) |\mathbf{f}(\mathbf{r})|^2 d^3\mathbf{r}}{n_{max}^2},
 \end{aligned} \tag{2.9}$$

which gives the the maximum amplitude of $\mathbf{E}(\mathbf{r}, t)$ for a cavity,

$$\mathbf{E}_{max}^{cav} = \sqrt{\frac{\hbar\omega}{2\varepsilon_0 n_{max}^2 V_{eff}}}. \tag{2.10}$$

The density of modes inside the cavity can be approximated as the following Lorentzian

$$\rho_{cav}(\omega) = \frac{1}{2\pi\hbar} \frac{\Delta\omega}{(\omega - \omega_{cav})^2 + (\Delta\omega/2)^2} \tag{2.11}$$

Since the cavity has only one resonant mode, the density of modes satisfies the normalization condition

$$\int_{-\infty}^{\infty} d(\hbar\omega) \rho_{cav}(\omega) = 1. \tag{2.12}$$

Using 2.1, the spontaneous emission rate in a cavity can be expressed as

$$\Gamma_{cav} = \frac{|\mathbf{d} \cdot \mathbf{E}|^2}{\hbar^2} \frac{\Delta\omega}{(\omega - \omega_{cav})^2 + (\Delta\omega/2)^2} \tag{2.13}$$

Thus, Purcell factor $F_p = \frac{\Gamma_{cav}}{\Gamma_{free}}$, the ratio of the cavity spontaneous emission rate to that of free space is

$$\begin{aligned}
 F_p &= \frac{\Gamma_{cav}}{\Gamma_{free}} \\
 &= \frac{1}{2\pi\hbar} \frac{3\pi^2\hbar c^3}{\omega^2 n^3 V_{eff}} \frac{|\mathbf{d} \cdot \mathbf{E}|^2}{|\mathbf{d}|^2 |\mathbf{E}|^2} \frac{\Delta\omega}{(\omega - \omega_{cav})^2 + (\Delta\omega/2)^2} \\
 &= \frac{3}{4\pi^2} \left(\frac{\lambda}{n}\right)^3 \frac{Q}{V_{eff}} \frac{|\mathbf{d} \cdot \mathbf{E}|^2}{|\mathbf{d}|^2 |\mathbf{E}|^2} \frac{\Delta\omega^2}{(\omega - \omega_{cav})^2 + (\Delta\omega/2)^2}, \tag{2.14}
 \end{aligned}$$

where we define a quality factor (Q-factor) Q as

$$Q = \frac{\text{Stored energy inside the cavity}}{\text{Power dissipation per cycle}} = \frac{\omega_{cav}}{\Delta\omega}. \tag{2.15}$$

If we have the dipole satisfying the following conditions,

- i. The dipole is positioned at the maximum electrical field position,
- ii. The direction of the dipole is aligned with that of the electrical field, and
- iii. The dipole spectrally resonates with the cavity $\omega = \omega_{cav}$,

we obtain the famous expression of Purcell factor,

$$F_p = \frac{3}{4\pi^2} \left(\frac{\lambda}{n}\right)^3 \frac{Q}{V_{eff}}, \tag{2.16}$$

where λ is the wavelength of the cavity resonance $\lambda = 2\pi c/\omega$.

2.3 Photonic crystal (PhC)

To enhance the spontaneous emission rate of QDs, PhC-based cavity is employed in this study. PhCs are artificial crystals with periodic refractive indices [76]. The period of the refractive indices is almost the same as the wavelength of light. The periodicity produces the photonic bandgap, where the propagation of the light is forbidden. This phenomenon can be understood by an analogy to the Bragg reflection of the light.

In order to intuitively understand the photonic bands and bandgaps, we examine 1D PhCs in this section [77]. We take the x axis in the direction perpendicular to the plane of the dielectric layers as shown in Fig. 2.2(a). We only deal with electromagnetic waves propagated in the x direction and polarized linearly here. We also take the z axis in the direction of the polarization. The electric field of the propagated wave is denoted by a complex function $E(x, t)$ for convenience. The actual electric field is by the real part of $E(x, t)$. Now, the wave equation for $E(x, t)$ is given by

$$\frac{d^2}{dt^2}E = \frac{c^2}{\varepsilon(x)}E, \quad (2.17)$$

where $\varepsilon(x)$ is the relative dielectric constant of the 1D PhC as a function of x . Here we assumed that the magnetic permeability of the PhCs equal to that in free space. Because $\varepsilon(x)$ is a periodic function of x ,

$$\varepsilon(x + a) = \varepsilon(x) \quad (2.18)$$

Let us expand $\varepsilon(x)^{-1}$ in a Fourier series:

$$\varepsilon(x)^{-1} = \sum_{m=-\infty}^{\infty} \kappa_m e^{iG_m x} \quad (2.19)$$

where m is an integer and κ_m is the Fourier coefficients for m . We also introduce $G_m = \frac{2\pi}{a}m$. Since we assume that $\varepsilon(x)$ is real, $\kappa_{-m} = \kappa_m^*$. If we utilize Bloch's theorem for electro-magnetic waves in PhCs, any eigen-mode in the 1D crystal is characterized by a wave number k and expressed as follows:

$$E(x, t) = E_k(x, t) = u_k(x) e^{i(kx - \omega_k t)}, \quad (2.20)$$

where ω_k denotes the eigen-angular frequency and $u_k(x)$ is a periodic function satisfying $u_k(x + a) = u_k(x)$. We expand $E_k(x, t)$ in a Fourier series:

$$E_k(x, t) = \sum_{m=-\infty}^{\infty} E_m e^{i(k+G_m)x} e^{-i\omega_k t}, \quad (2.21)$$

where E_m is the Fourier coefficient.

Now for simplicity, we assume that only components with $m = 0$ and ± 1 are dominant in the expansion (2.19):

$$\varepsilon(x)^{-1} \approx \kappa_0 + \kappa_1 e^{2i\pi x/a} + \kappa_{-1} e^{-2i\pi x/a} \quad (2.22)$$

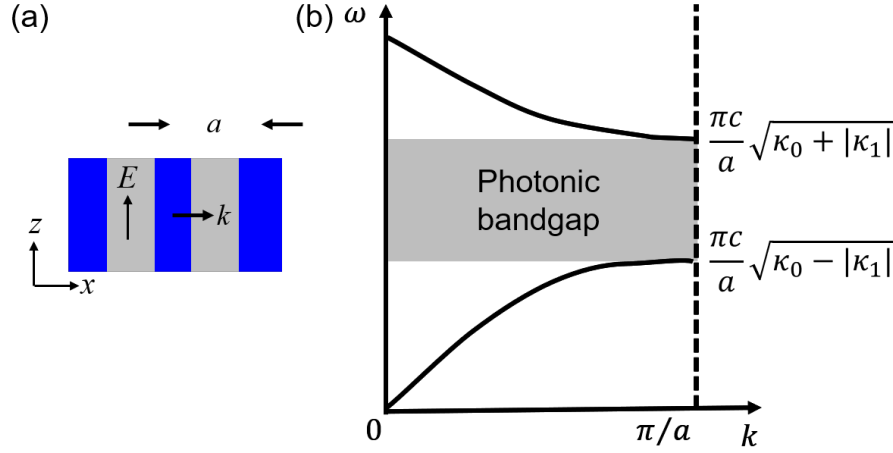


Figure 2.2: (a) Schematics of the investigated periodic structure for calculating dispersion relation of a 1D PhC. (b) Dispersion relation for a 1D PhC.

By substituting (2.21) and (2.22) into 2.17, we can obtain

$$\begin{aligned} \kappa_1 \left\{ k + \frac{2(m-1)\pi}{a} \right\}^2 E_{m-1} + \kappa_{-1} \left\{ k + \frac{2(m+1)\pi}{a} \right\}^2 E_{m+1} \\ \approx \left\{ \frac{\omega_k^2}{c^2} - \kappa_0 \left(\frac{k + 2m\pi}{a} \right)^2 \right\} E_m \end{aligned} \quad (2.23)$$

Let us consider the case for $m = 0$ and $m = -1$. We also consider the bandedge: $k \approx \pi/a$, $\omega_k^2 \approx \kappa_0 c^2 k^2$. In this case, E_0 and E_{-1} are dominant in the expansion (2.21), and we can neglect all other terms and obtain the following coupled equations:

$$\begin{cases} (\omega_k^2 - \kappa_0 c^2 k^2) E_0 - \kappa_1 c^2 \left(k - \frac{2\pi}{a} \right)^2 E_{-1} = 0 \\ -\kappa_{-1} c^2 k^2 E_0 + \left\{ \omega_k^2 - \kappa_0 c^2 \left(k - \frac{2\pi}{a} \right)^2 \right\} E_{-1} = 0 \end{cases} \quad (2.24)$$

These linear equations have a nontrivial solution when the determinant of coefficients equals zero:

$$\omega_{\pm}(K) = \frac{\pi c}{a} \sqrt{\kappa_0 \pm |\kappa_1|} \pm \frac{a c \kappa_0^{3/2}}{\pi |\kappa_1|} K^2, \quad (2.25)$$

where we introduce $k - \pi/a = K$ (we assume $|K| \ll \pi/a$). Therefore, there is no mode in the interval

$$\frac{\pi c}{a} \sqrt{\kappa_0 - |\kappa_1|} < \omega < \frac{\pi c}{a} \sqrt{\kappa_0 + |\kappa_1|}. \quad (2.26)$$

This energy gap disappears when $\kappa_1 = 0$. Figure 2.2(b) illustrates the dispersion relation for a 1D PhC. This result can be interpreted that the modes with $k \approx \pm\pi/a$ are mixed with each other in the presence of the periodic modulation of the dielectric constant and this mixing lead to a frequency splitting.

2.4 Photon statistics with second-order correlation function

In this section, we discuss the tools to verify the single photon generation. The photon statistics of a quantum state of light is determined by recording the second-order correlation function $g^{(2)}(\tau)$ [78, 79].

In the 1950s, Hanbury Brown and Twiss developed a new kind of correlation experiment that involved the correlation of intensities rather than of fields [80]. A sketch of the Hanbury Brown-Twiss experiment is shown in Fig. 2.3(a). Detectors 1 and 2 are the same distance from the beam splitter. This setup enables us to measure a delayed coincidence rate where one of the detectors registers a count (E_1) at time t and the other a count (E_2) at $t + \tau$. If τ is smaller than the coherence time of the light τ_c , information on the statistics of the light beam striking the beam splitter can be determined. The rate of coincident counts is proportional to the time average:

$$C(t, t + \tau) = \langle I(t)I(t + \tau) \rangle, \quad (2.27)$$

where $I(t)$ and $I(t + \tau)$ are the instantaneous intensities at the two detectors (these are classical quantities here). If we assume that the fields are stationary, the average is a function only of t . We also assume that the average of the intensity at each detector is $\langle I(t) \rangle$. In our case, we care only about the correlations at a fixed point, and thus our $g^{(2)}(\tau)$ has only two time arguments. Classically, this is defined as the auto-correlation of the optical intensity:

$$g^{(2)}(\tau) = \frac{\langle E^*(t)E^*(t + \tau)E(t + \tau)E(t) \rangle}{\langle E^*(t)E(t) \rangle \langle E^*(t + \tau)E(t + \tau) \rangle} = \frac{\langle I(t)I(t + \tau) \rangle}{\langle I(t) \rangle \langle I(t + \tau) \rangle}, \quad (2.28)$$

where τ is the delay time and $E(t)$ and $I(t)$ are the electric field and intensity of the light at time t . We also note that $\langle f(t) \rangle$ indicates the time average which is obtained by integrating over a long time period. Here we assume a light source with constant average intensity (i. e., $\langle I(t) \rangle = \langle I(t + \tau) \rangle$).

2.4.1 Classical case

We begin with the description of $g^{(2)}(\tau)$ based on the classical theory of light. Here, we introduce the following quantity:

$$\sigma(I)^2 = \langle (I(t) - \langle I \rangle)^2 \rangle \quad (2.29)$$

where $\sigma(I)$ is the fluctuation from the mean intensity $\langle I \rangle$. Since the averaged value of this quantity $\sigma(I)$ is zero, it is apparent that

$$\langle I(t)^2 \rangle = \langle I \rangle^2 + \sigma(I)^2 \geq \langle I \rangle^2. \quad (2.30)$$

$g^{(2)}(\tau = 0)$ can be expressed as

$$g^{(2)}(0) = 1 + \frac{\sigma(I)^2}{\langle I \rangle^2} \geq 1. \quad (2.31)$$

By using Cauchy-Schwartz inequality

$$\langle I(t)I(t+\tau) \rangle^2 \leq \langle I(t)^2 \rangle \langle I(t+\tau)^2 \rangle = \langle I(t)^2 \rangle^2, \quad (2.32)$$

we can obtain the following relation,

$$g^{(2)}(\tau) \leq g^{(2)}(0) \quad (2.33)$$

For $\tau \rightarrow \infty$, we have no correlation any more;

$$\langle I(t)I(t+\tau) \rangle \rightarrow \langle I(t) \rangle \langle I(t+\tau) \rangle = \langle I(t) \rangle^2 \quad (2.34)$$

Hence we obtain

$$g^{(2)}(\tau) \rightarrow 1. \quad (2.35)$$

From the above discussion, we can conclude that the classical light satisfies the following conditions:

$$g^{(2)}(\tau) \leq g^{(2)}(0) \quad (2.36)$$

$$g^{(2)}(\tau) \rightarrow 1(\tau \rightarrow \infty) \quad (2.37)$$

2.4.2 Quantum case

Next, we treat $g^{(2)}(\tau)$ based on the quantum theory of light. If we quantize the electromagnetic field as

$$\hat{E}(t) = -i\sqrt{\frac{\hbar\omega}{2\varepsilon V}} (\hat{a}(t) - \hat{a}^\dagger(t)), \quad (2.38)$$

the second-order correlation function of the light can be rewritten as follows:

$$g^{(2)}(\tau) = \frac{\langle \hat{a}^\dagger(t)\hat{a}(t+\tau)^\dagger\hat{a}(t+\tau)\hat{a}(t) \rangle}{\langle \hat{a}^\dagger(t)\hat{a}(t) \rangle \langle \hat{a}(t+\tau)^\dagger\hat{a}(t+\tau) \rangle}, \quad (2.39)$$

where $\hat{a}(t)$ and $\hat{a}^\dagger(t)$ are the annihilation and creation operators of photons at time t , respectively. For the zero delay $\tau = 0$, $g^{(2)}(\tau)$ can be simplified using the number operator $\hat{n} = \hat{a}^\dagger\hat{a}$:

$$\begin{aligned} g^{(2)}(0) &= \frac{\langle \hat{a}^\dagger\hat{a}^\dagger\hat{a}\hat{a} \rangle}{\langle \hat{a}^\dagger\hat{a} \rangle \langle \hat{a}^\dagger\hat{a} \rangle} \\ &= \frac{\langle \hat{n}^2 \rangle - \langle \hat{n} \rangle}{\langle \hat{n} \rangle^2}. \end{aligned}$$

Here, we defined the annihilation operator \hat{a} as

$$\hat{a} |n\rangle = \sqrt{n} |n-1\rangle. \quad (2.40)$$

Similarly, we defined the creation operator \hat{a}^\dagger as

$$\hat{a}^\dagger |n\rangle = \sqrt{n+1} |n+1\rangle, \quad (2.41)$$

which satisfies $[\hat{a}, \hat{a}^\dagger] = 1$.

Thus, we obtain the simple expression of $g^{(2)}(0)$ as

$$g^{(2)}(0) = 1 + \frac{\sigma(n)^2 - \langle \hat{n} \rangle}{\langle \hat{n} \rangle^2}, \quad (2.42)$$

where $\sigma(n)^2 = \langle \hat{n}^2 \rangle - \langle \hat{n} \rangle^2$ is the fluctuation of the photon number.

By evaluating $g^{(2)}(0)$, we can learn whether a light source is bunched, Poisson-like or anti-bunched as below (see also Fig. 2.3(b)). If the light source is anti-bunched, we can confirm that the source can generate single photons.

$$\begin{cases} g^{(2)}(0) > 1 : & \text{Bunched source} \\ g^{(2)}(0) = 1 : & \text{Poisson-like source} \\ g^{(2)}(0) < 1 : & \text{Anti-bunched source} \end{cases}$$

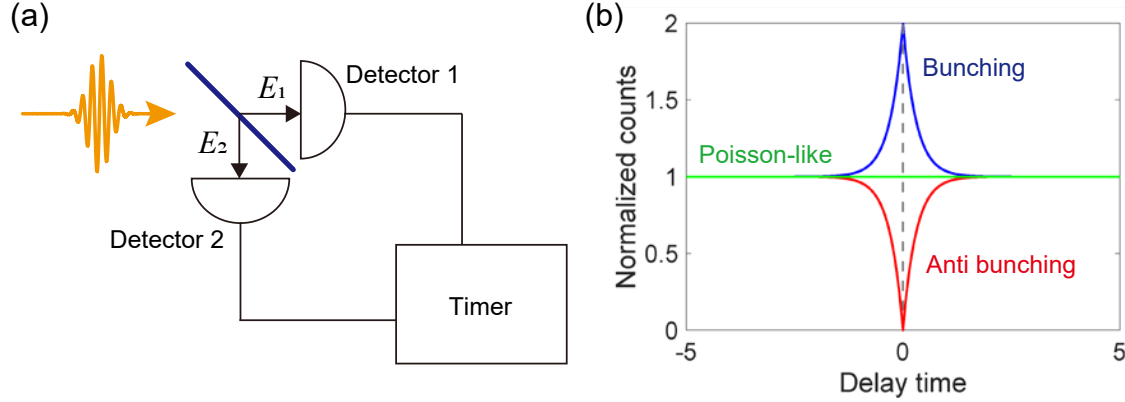


Figure 2.3: (a) A sketch of the Hanbury Brown-Twiss experiment. (b) Intensity correlation functions $g^{(2)}(\tau)$ of bunching source (blue), Poisson-like source (green) and anti bunching source (red).

Bunched source

The bunched source is defined as the light with $g^{(2)}(0) > 1$. If the photon is detected at $t = 0$, there is a higher probability of detecting another photon at short times than longer times. Sources of bunched photons include thermal light sources. To observe this bunching, one needs either excellent time resolution in the detectors, or a narrow-band light source, since the width of the peak in $g^{(2)}(\tau)$ is approximately $\Delta\tau \sim 1/\Delta\omega$ ($\Delta\omega$: source bandwidth). A source will also be bunched due to the blinking effect [81]. For instance, if it is blinking on and off with a time scale of τ_b , a peak will appear in $g^{(2)}(\tau = 0)$ with a width of τ_b . The height of this peak depends on how much time the source spends in its “off” state, compared to the “on” state. If it is usually “off”, then the peak will be large.

As an example, we consider the thermal light source. A thermal state of light describes the blackbody radiation, which is generated by matter at thermal equilibrium with the environment. We assume a single radiation mode within a cavity at a frequency ω . The probability that there will be n photons in this mode is given by Boltzmann’s law:

$$w_n = \frac{e^{-n\beta\hbar\omega}}{\sum_{n=0}^{\infty} e^{-n\beta\hbar\omega}} = (1 - \zeta)\zeta^n, \quad (2.43)$$

where $\beta = 1/k_B T$ is the inverse temperature (k_B : Boltzmann constant, T : temperature within the cavity) and $\zeta = e^{-\beta\hbar\omega}$ is Boltzmann factor. The density operator

of the thermal state is expressed as

$$\hat{\rho}_{thermal} = \sum_{n=0}^{\infty} w_n |n\rangle \langle n| = (1 - \zeta) \sum_{n=0}^{\infty} \zeta^n |n\rangle \langle n|. \quad (2.44)$$

Thus we can evaluate the expectation value of the number operator as follows:

$$\begin{aligned} \langle \hat{n} \rangle &= \text{Tr}(\hat{n} \hat{\rho}_{thermal}) = (1 - \zeta) \sum_{i,n=0}^{\infty} \zeta^n \langle i | \hat{n} | n \rangle \langle n | i \rangle \\ &= (1 - \zeta) \sum_{n=0}^{\infty} n \zeta^n = \frac{\zeta}{1 - \zeta}. \end{aligned} \quad (2.45)$$

Likewise, we can obtain the fluctuation of the photon number as

$$\sigma(n)^2 = \langle \hat{n}^2 \rangle - \langle \hat{n} \rangle^2 = \langle \hat{n} \rangle + \langle \hat{n} \rangle^2 \quad (2.46)$$

By combining the equations (2.42) and (2.46), we can evaluate the $g^{(2)}(0)$ value for the thermal light as

$$g^{(2)}(0) = 2 > 1, \quad (2.47)$$

which agrees with the discussion based on classical theory. The corresponding intensity correlation function is illustrated in the blue curve in Fig. 2.3(b).

Poisson-like source

If we have $g^{(2)}(0) = 1$, the source is Poisson-like. The photon number may follow a Poisson distribution, but it is not easy to prove this simply by measuring $g^{(2)}(\tau)$. For a true Poisson process, each photon arrives independently. Ideally, a laser emits a coherent state $|\alpha\rangle$, for which the photon number follows a Poisson distribution. For most large-bandwidth non-blinking thermal light sources, the measured $g^{(2)}(0)$ will appear to be 1 since the photon detectors will be too slow to resolve the bunching effect.

We can show that the coherent state satisfies $g^{(2)}(0) = 1$. The coherent state is defined by

$$\hat{a} |\alpha\rangle = \alpha |\alpha\rangle, \quad (2.48)$$

where α is the complex number specifying the complex field amplitude in photon number units. In the photon number representation, the coherent state is expressed as

$$|\alpha\rangle = e^{-|\alpha|^2/2} \sum_{n=0}^{\infty} \frac{\alpha^n}{\sqrt{n!}} |n\rangle. \quad (2.49)$$

The expectation value of number operator is then given by

$$\langle n \rangle = \langle \alpha | n | \alpha \rangle = \alpha^* \alpha. \quad (2.50)$$

We find that

$$\sigma(n)^2 = \langle \hat{n}^2 \rangle - \langle \hat{n} \rangle^2 = \langle \hat{n} \rangle. \quad (2.51)$$

Therefore, we can deduce the $g^{(2)}(0)$ value for the coherent light by using the equations (2.42) and (2.51) as

$$g^{(2)}(0) = 1. \quad (2.52)$$

The corresponding intensity correlation function is illustrated in the green curve in Fig. 2.3(b).

Anti-bunched source

The anti-bunched source is defined as the light with $g^{(2)}(0) < 1$. If the photon is detected at $t = 0$, there is a lower probability of detecting another photon at short times than longer times. Such behavior can be observed from light sources based on a single quantum emitter. This type of source is called “non-classical light source”, whose property is totally different from that of the classical light source ($g^{(2)}(\tau) \leq g^{(2)}(0)$).

We consider the Fock number state $|n\rangle$. Since $\hat{n} |n\rangle = n |n\rangle$, we can obtain the fluctuation for Fock state as

$$\sigma(n)^2 = \langle \hat{n}^2 \rangle - \langle \hat{n} \rangle^2 = 0 \quad (2.53)$$

Thus we can obtain $g^{(2)}(0)$ for the Fock number state $|n\rangle$ as

$$g^{(2)}(0) = \frac{n(n-1)}{n^2}. \quad (2.54)$$

From this equation, it is obvious that we can obtain $g^{(2)}(0) < 1$ for any n , violating the classical limit for the second order correlation function (2.33). Particularly for $n = 1$ (the case of the single-photon state), we can clearly see that

$$g^{(2)}(0) = 0. \quad (2.55)$$

The corresponding intensity correlation function is illustrated in the red curve in Fig. 2.3(b). Ideal SPSs satisfy the equation (2.55), and the single-photon generation can be experimentally verified by measuring $g^{(2)}(0) < 0.5$ (since we can find $g^{(2)}(0) = 0.5$ for $n = 2$).

Chapter 3

Design for integrated single-photon source with near-unity waveguide coupling

3.1 Introduction

Toward the scalable operation of integrated quantum optical circuits, it is vital to design the efficient structure of waveguide-coupled SPSs. Since transfer printing is based on a simple pick-and-place manner, separate preparation of required components is possible, allowing us to investigate flexible design for efficient SPS device structure. This chapter theoretically demonstrates that our SPS structure's design enables the coupling of single-photon emission from QDs into the photonic waveguide over 99%. Besides, numerical simulations reveal that this near-unity coupling efficiency can be maintained even under the position misalignment of QD SPSs. Moreover, our SPS design structure is robust for the change in material platforms. Before describing the design concept, the basic contents of transfer printing are briefly introduced. The numerical simulations of this thesis are performed with commercial software Rsoft.

3.2 Transfer printing

In this section, we introduce the primary contents of transfer printing, a material assembly technique that uses elastomeric stamps for heterogeneous integration of various classes of micro/nano-structured materials onto a wide variety of target

substrates. A major advance in transfer printing was made by J. A. Rogers group in 2004 [82, 83]. In transfer printing, a thin film material stack or device is transferred from a source substrate to a target substrate using a soft elastomeric stamp. As described below, the adhesion to the elastomeric stamp relies on the velocity of the stamp. The components can be picked up from the native substrate by moving up the stamp quickly and printed to a target substrate by slowly releasing the stamp. There are already plenty of reports on heterogeneously integrated photonic and electronic devices using transfer printing, including solar cells, light-emitting diodes (LEDs), lasers, photodetectors, and digital imaging systems [84–86].

3.2.1 Principle of transfer printing

The basis of the transfer printing is the rate-dependence adhesion strength of the object to the elastomer stamp [83, 87]. Inset in Fig. 3.1 shows a schematic diagram of a stamp on a substrate subjected to a peel force F normal to the stamp/substrate interface. The stamp is peeled off from the substrate at a speed of v . Here we introduce the energy release rate G , which is related to the peel force by

$$G = \frac{F}{w}, \quad (3.1)$$

where w is the stamp width. We assume that the ink and substrate are elastic, while the stamp is viscoelastic. The critical energy release rate for the ink/substrate interface is given by $G_{crit}^{ink/substrate}$, which is considered as a material property of the interface and is independent of the peeling velocity v because the ink and substrate are elastic. The critical energy release rate $G_{crit}^{stamp/ink}$ for the stamp/ink interface, however, depends on v ; $G_{crit}^{stamp/ink} = G_{crit}^{stamp/ink}(v)$. This is a monotonically increasing function because the energy dissipation in the viscoelastic stamp increases with v . We can obtain the criterion for pickup and printing simply by comparing $G_{crit}^{ink/substrate}$ and $G_{crit}^{stamp/ink}(v)$. Figure 3.1 shows a schematic diagram of critical energy release rates $G_{crit}^{ink/substrate}$ and $G_{crit}^{stamp/ink}(v)$ as a function of v . $G_{crit}^{ink/substrate}$ corresponds to a horizontal blue line since it is independent of v . On the other hand, $G_{crit}^{stamp/ink}(v)$ is a monotonically increasing function of v . There exists a critical velocity (v_c) at which the two critical energy release rates are equal,

$$G_{crit}^{ink/substrate} = G_{crit}^{stamp/ink}(v_c) \quad (3.2)$$

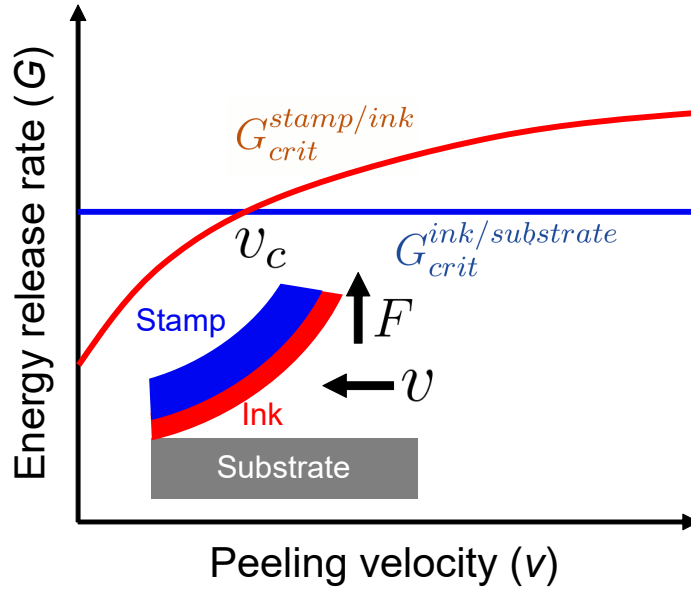


Figure 3.1: Schematic diagram of critical energy release rates $G_{crit}^{ink/substrate}$ and $G_{crit}^{stamp/ink}(v)$ as a function of v (Inset. Schematic diagram of a stamp on a substrate subjected to a peel force F normal to the stamp/substrate interface).

Thus we can obtain the criterion for pickup and printing based on the peeling velocity;

$$\left\{ \begin{array}{ll} G_{crit}^{ink/substrate} < G_{crit}^{stamp/ink}(v > v_c) : & \text{Ink is peeled off from the substrate.} \\ & \text{(i.e., pickup)} \\ G_{crit}^{ink/substrate} > G_{crit}^{stamp/ink}(v < v_c) : & \text{Ink remains on the substrate.} \\ & \text{(i.e., printing)} \end{array} \right.$$

3.3 Device design for near-unity QD-waveguide coupling

In this section, we design the QD-based SPS device structure, which allows near-unity coupling of QD emission into the photonic waveguide. Figures 3.2(a) and (b) respectively display the top view and cross-section of the schematic waveguide-coupled SPS. A QD SPS is placed above the photonic waveguide cladded with SiO₂. This structure can be experimentally fabricated by transfer printing: the QD SPS is printed on a flat SiO₂ surface above the photonic waveguides. In this device, a 1D PhC nanobeam cavity is employed for the SPS to support the efficient coupling of the QD emission into the underneath photonic waveguide thanks to the Purcell effect. First, the photons emitted from QDs are coupled to the fundamental resonant mode of the cavity. This cavity mode is then coupled to the underneath photonic waveguide evanescently. Figure 3.2(c) shows the computed cross-sectional field profile of the investigated cavity mode coupled to the underneath GaAs waveguide (E_y component), confirming the efficient cavity-waveguide coupling without noticeable photon leakage into free space. Here, we introduced the cavity-waveguide coupling efficiency η and emitter-cavity coupling efficiency β , which gives the overall emitter-waveguide coupling efficiency ($\eta\beta$). Now we describe the details of optimizing η and β .

3.3.1 Cavity-waveguide coupling efficiency (η)

According to the coupled mode theory [88], the cavity-waveguide coupling constant κ is given by the following equation;

$$\kappa = \frac{\int d\mathbf{r} \frac{\Delta\epsilon(\mathbf{r})}{c^2} e^{i(k_{cav}-k_{wg})x} \mathbf{E}_{cav}^*(\mathbf{r}) \mathbf{E}_{wg}(\mathbf{r})}{\int d\mathbf{r} \frac{2\epsilon(\mathbf{r})}{c^2} |\mathbf{E}_{cav}(\mathbf{r})|^2}, \quad (3.3)$$

where $\Delta\epsilon(\mathbf{r}) = \epsilon_t(\mathbf{r}) - \epsilon_w(\mathbf{r})$ ($\epsilon_t(\mathbf{r})$: the relative dielectric constant for the cavity, $\epsilon_w(\mathbf{r})$: the dielectric constant for the waveguide).

Following the coupled mode theory formalism, we can express η by the following equation:

$$\eta = \frac{Q_{waveguide}^{-1}}{Q_0^{-1} + Q_{waveguide}^{-1} + Q_{scatter}^{-1}}, \quad (3.4)$$

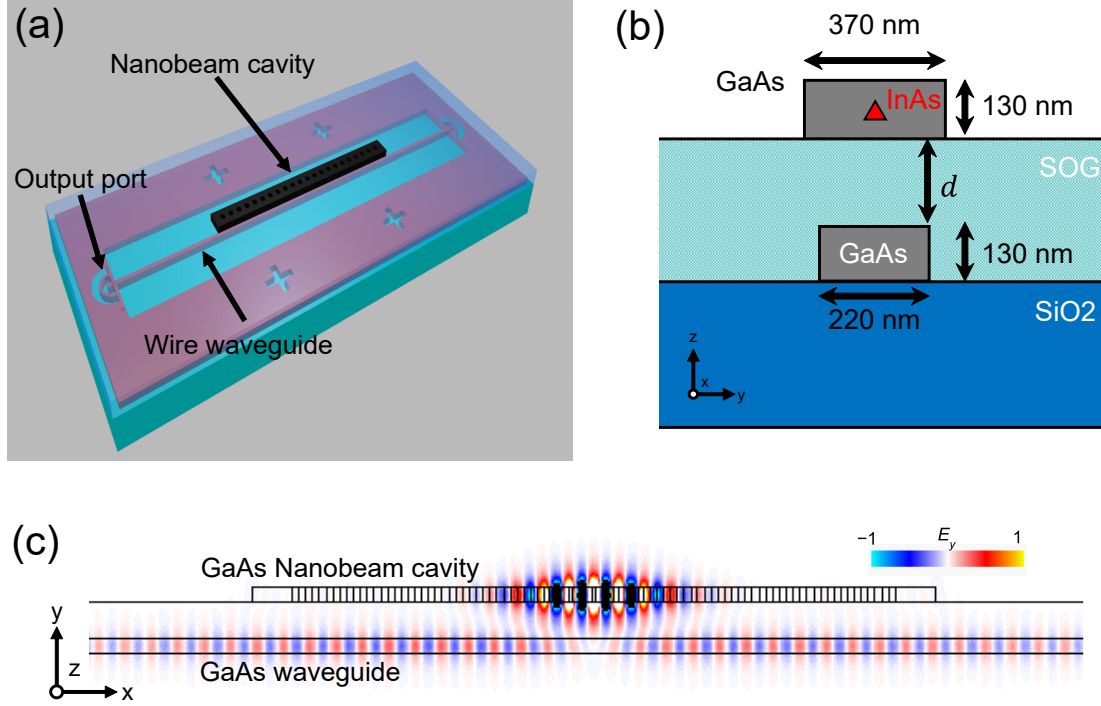


Figure 3.2: (a) Top view and (b) cross section of the schematic waveguide-coupled SPS. (c) Simulated cross-sectional field profile of the investigated cavity mode (E_y) coupled to the underneath GaAs photonic waveguide.

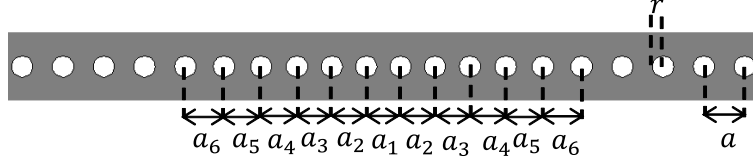


Figure 3.3: Schematic of the cavity design for achieving ultra high Q_0 . In this work, we disturbed the period of air holes quadratically ($a_1 = 0.84a$, $a_2 = 0.844a$, $a_3 = 0.858a$, $a_4 = 0.88a$, $a_5 = 0.911a$, $a_6 = 0.951a$).

where Q_0 and $Q_{\text{waveguide}}$ are the quality factors of the cavity without and with the photonic waveguide, respectively. $1/Q_{\text{scatter}}$ expresses the additional photon scattering loss from the cavity into free space because of the introduction of the photonic waveguide. From this equation, for realizing a high efficiency η , it is vital to design a very high Q_0 and a low $Q_{\text{waveguide}}$, while suppressing $1/Q_{\text{scatter}}$. From (3.3) and (3.4), high η is achieved by addressing the following 3 points.

- i Designing high-Q factor nanobeam cavities (achieving high Q_0).
- ii Realizing low $Q_{\text{waveguide}}$.
- iii Achieving the phase-matched condition between the cavity and photonic waveguide $k_{\text{cav}} = k_{\text{wg}}$.

Details of the high-Q nanocavity design

We designed the PhC nanobeam cavity with a very high quality factor when being solely placed on flat SiO_2 [89]. Figure 3.3 shows a schematic of the cavity design. Here, we considered a GaAs-based (refractive index of $n_{\text{GaAs}} = 3.4$) PhC nanobeam cavity with a width of $w = 370$ nm and a thickness of $t = 130$ nm. The nanobeam air holes have radii of $r = 59.8$ nm and a period of $a = 230$ nm. For the formation of the PhC nanobeam cavity, we disturbed the period of air holes quadratically: $a_1 = 0.84a$, $a_2 = 0.844a$, $a_3 = 0.858a$, $a_4 = 0.88a$, $a_5 = 0.911a$ and $a_6 = 0.951a$, respectively [90–92]. We assumed the refractive index of SiO_2 to be $n_{\text{SiO}_2} = 1.45$ in this simulation. We simulated properties of the fundamental resonant mode of the investigated cavity at a normalized frequency a/λ of 0.249 (corresponding cavity resonant wavelength of $\lambda = 920$ nm) using the finite-difference time-domain (FDTD) method. We obtained a very high quality factor of 5.4×10^6 with a very small mode volume of $0.434 \times (\lambda/n)^3$.

Detailed calculation of the cavity-waveguide coupling

Since the cavity-waveguide coupling relies on evanescent coupling, η can be optimized by tuning the cavity-waveguide distance (d). We simulated quality factors of the cavity with the photonic waveguide as a function of d , as shown in the black curve of Fig. 3.4. It is apparent that the quality factors decreases exponentially with the reduction of d . The sharp reduction in Q predominantly stems from the cavity-waveguide coupling, which can be confirmed by the direct calculation of η . The calculation of η begins with the simulation of the investigated cavity mode using the FDTD method. When the simulated cavity resonant mode reached its steady state, we compared the light leakage from the waveguide with that from whole simulation domain. We deduced η by comparing these light leakage. The red curve in Fig. 3.4 shows the simulated η as a function of d . When $250 \text{ nm} < d < 450 \text{ nm}$, a cavity-waveguide coupling efficiency $\eta > 99\%$. In contrast, further reduction of d leads to a degradation of η ($d < 200 \text{ nm}$), as the photonic waveguide becomes too close to the cavity and starts to scatter cavity photons into free space. In such cases, the index modulation by the photonic waveguide becomes too strong to treat as a perturbation for the cavity mode.

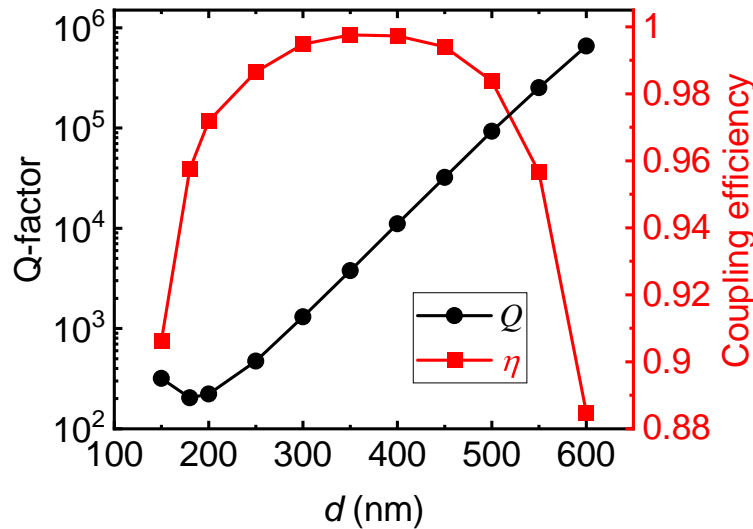


Figure 3.4: Calculated Q and η as a function of the cavity-waveguide distance d .

Details of the waveguide design

According to (3.3), it is essential to achieve phase-matching condition between the cavity resonant mode and waveguide propagation mode in order to obtain the maximum possible cavity-waveguide coupling for a given d . For this purpose, the width of the photonic waveguide was optimized [93]. Figure 3.5 shows the schematic dispersion diagram of the nanobeam cavity and waveguide. Phase-matching condition is achieved when the waveguide dispersion crosses at the band edge (π/a) and cavity resonant frequency ω_0 ($= 2\pi c/\lambda$). For this case, the effective refractive index of the photonic waveguide (n_{eff}) is given by the following equation;

$$n_{eff} = \frac{c}{\omega_0} \frac{\pi}{a} = \frac{\lambda}{2a}. \quad (3.5)$$

We calculated n_{eff} using the finite element method (FEM) and fixed the thickness of the photonic waveguide to be 130 nm for simplicity. When $a = 230$ nm, the required n_{eff} is 2.0, which can be obtained for the case when the width of the waveguide is 220 nm.

The black curve in Fig. 3.6 shows calculated quality factors of the investigated cavity as a function of the width of the photonic waveguide when the cavity-waveguide distance is set to be $d = 300$ nm. Cavity quality factors take their minimum value around the width of 220 nm, which agrees with the above discussion. The reduction of Q predominantly stems from the cavity-waveguide coupling, rather than the free space leakage from the cavity. This can be confirmed by numerical calculation of η s based on the radiation power distribution, whose results are summarized in the red curve in Fig. 3.6. η for the width of 220 nm was found to be 99.5%. Thus we employed the GaAs photonic waveguide with a width of 220 nm in this work. From a different point of view, we can interpret that from (3.3) the coupling efficiency can be maximized when we obtain the largest overlap integral κ between the investigated cavity mode and the waveguide propagating mode in the sense of the coupled mode theory [88].

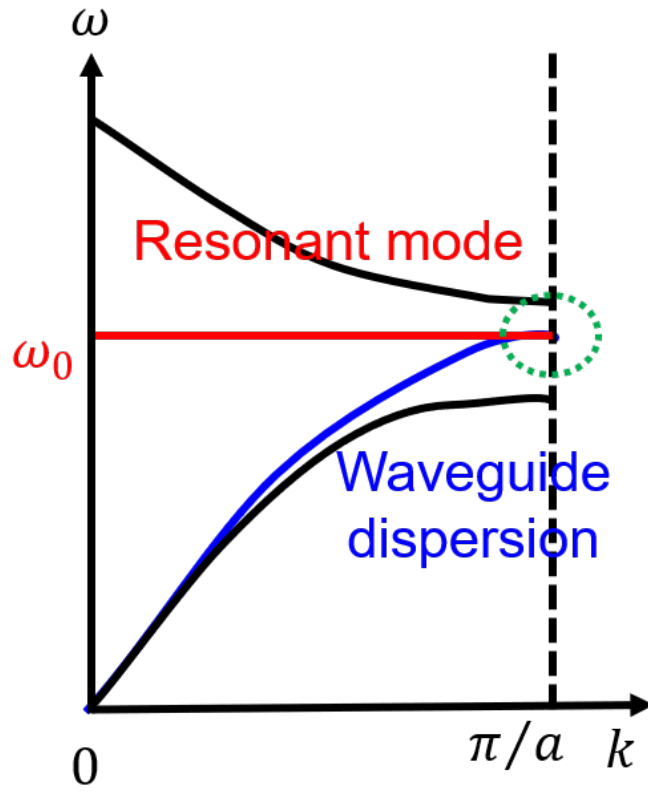


Figure 3.5: Schematic dispersion diagram of the nanobeam cavity and photonic waveguide.

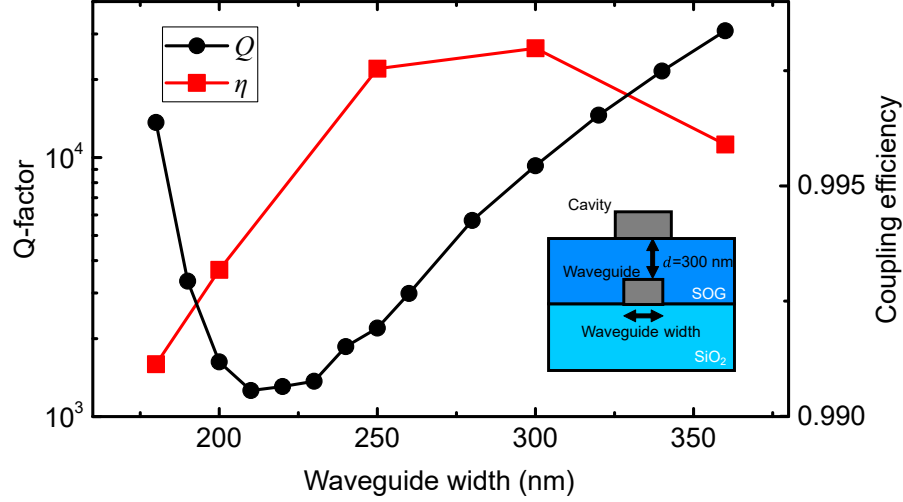


Figure 3.6: Calculated cavity-waveguide coupling as a function of the width of the photonic waveguide.

3.3.2 Emitter-cavity coupling efficiency (β)

Next, β is investigated. When we assumed that spontaneous emission of the investigated QD coupled to either the cavity of free space, we can express β by the following equation:

$$\beta = \frac{F_p \gamma_0}{F_p \gamma_0 + \gamma_{other}}, \quad (3.6)$$

where F_p is the Purcell factor, γ_0 is the spontaneous emission rate of QDs in the unprocessed area (not in the cavity) and γ_{other} is the decay rate of QD emission into free space. Thanks to the Purcell enhancement, the nanobeam cavity allows us to obtain fast spontaneous emission into the cavity mode with an emission rate $F_p \gamma_0$. On the other hand, the photonic bandgap effect inside the 1D nanobeam PhC suppresses the spontaneous emission rate of embedded QDs by half [92]. Consistent with this previous report of [92], we experimentally confirmed γ_{other} to be $\sim 0.5\gamma_0$.

Figure 3.7 shows the calculated β and η as a function of the cavity-waveguide distance d . Since F_p is proportional to Q/V , β is reduced as d decreases. Nevertheless, for the case when $d = 300$ nm ($Q = 1,300$), the maximum possible Purcell factor is $F_p = 250$, which leads to a near-unity β of 99.7%. As a result, the overall single-photon coupling efficiency into the photonic waveguide ($\eta\beta$) reaches a near-ideal value of $\eta\beta = 99.2\%$.

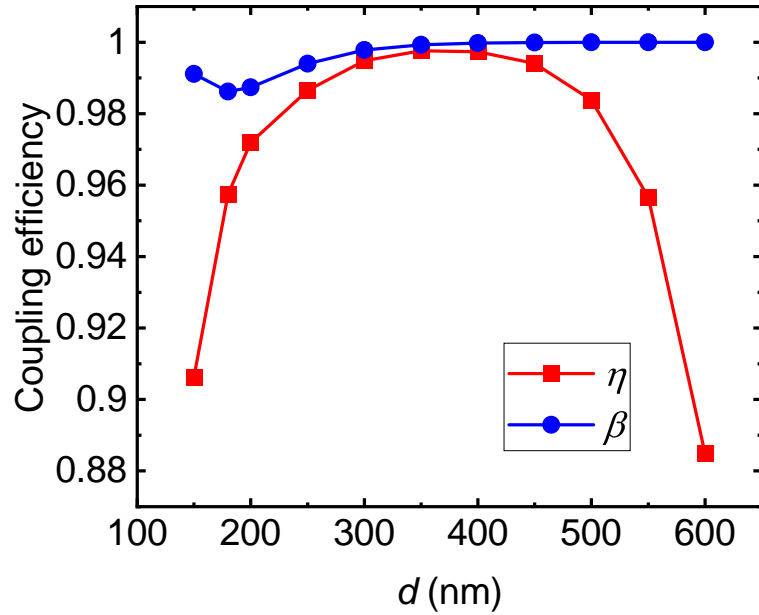


Figure 3.7: Calculated β and η as a function of the cavity-waveguide distance d .

3.4 Direct simulation of $\eta\beta$ using point dipole source

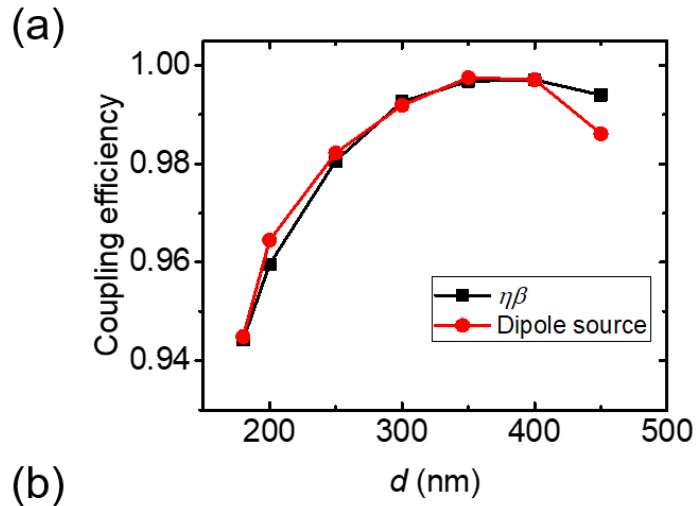
In this section, we further confirmed the high coupling efficiencies of single photons, $\eta\beta$ s by performing numerical simulations based on a point dipole as a radiation source [94]. We evaluated $\eta\beta$ by comparing the power distribution to the photonic waveguide with the whole radiated power. Here, we assumed the dipole emitter to be

- (i) linearly polarized (parallel to the slab and perpendicular to the guiding direction of the nanobeam cavity),
- (ii) controlled to have the same emission wavelength as that of the fundamental cavity mode, and
- (iii) placed in the center of the cavity, where we can obtain the strongest electric field of the fundamental mode.

We also considered that the dipole source reasonably emulates our QDs, which are thin-disk-like shape and thus possess strong optical transition dipoles parallel to

the slab (normal to the growth direction). Strong linear polarizations are available for, e.g., neutral exciton states subjected to an anisotropic electron-hole exchange interaction. Figure 3.8(a) shows a comparison of the direct calculation of $\eta\beta$ (shown in red) with the separated calculation, as discussed in the previous section (shown in black). These two curves match each other well, confirming the validity of the separated simulations of η and β to estimate total single-photon coupling efficiencies. For the case when $d = 350$ nm, the simulation based on the point dipole source results in $\eta\beta = 99.8\%$. We attributed the residual deviations between the two curves to the finite simulation accuracy in the FDTD method, which is mainly limited by, e.g., the grid size of the calculation space and simulation time length.

Next, we simulated the total single-photon coupling efficiency when the dipole source deviates from the maximum of the cavity field. According to (2.14), the Purcell factor depends on the position of the dipole. Figure. 3.8(b) summarizes the total single-photon coupling efficiencies under the existence of spatial source misalignment ($d = 300$ nm). These simulation results well agree with the analytical predictions based on the conventional theory of the Purcell effect: we solely took into account the reduction of the local field intensity at the position of the dipole source. These results indicate the importance of the accurate QD positioning to the cavity center when maximizing the SPS efficiency. Alternatively, we can realize efficient single photon coupling by the pre-selection of a proper QD SPS with strong Purcell effect before the transfer.



No.	Predicted efficiency	Simulated efficiency	Position of the dipole source
1	99.2%	99.0%	x = 0 nm, y = 0 nm
2	93.8%	93.8%	x = 700 nm, y = 170 nm
3	89.1%	88.4%	x = 1280 nm, y = 0 nm

Figure 3.8: (a) Comparison of the the direct calculation of $\eta\beta$ (shown in red) with the separated calculation, as discussed in the previous section (shown in black). (b) Summary of the total single-photon coupling efficiencies under the existence of spatial source misalignment.

3.5 Robustness against misalignment of cavity with respect to waveguide

In this section, we verified that the designed SPS device structure can maintain high η s even under the presence of cavity-waveguide misalignment. First, we checked the robustness against the in-plane deviation of the nanobeam (δ , the center-to-center distance between the nanobeam cavity and photonic waveguide). Figure 3.9(a) shows the calculated η s as a function of δ . For the case when $\delta \leq 200$ nm, we can see that simulated quality factors is $Q < 4,000$, which is low enough to get $\eta > 99\%$. Indeed, these low quality factors are mainly due to the waveguide coupling since we evaluated a η of 99.5% for the case when $\delta = 200$ nm by the numerical calculation based on the power distributions using the FDTD simulation.

Next, we examined the tolerance against the rotation, quantified by the angle between the cavity and photonic waveguide (θ). Figure 3.9(b) shows the calculated η s as a function of θ . Again, we can see the low quality factor ($Q < 2,000$) for the case when $\theta \leq 10^\circ$, suggesting that the high η is maintained even under the presence of the angular displacement. For the case when $\theta = 10^\circ$, we confirmed a $\eta > 99\%$ by using the FDTD method.

We also confirmed the robustness under the presence of both finite δ and θ . Figure 3.9(c) summarizes the cases when δ of 100 and 200 nm and $0^\circ \leq \theta \leq 10^\circ$. It is clearly seen that quality factors are still kept low even under the presence of the combined misalignment. For the case when $\delta = 200$ nm and $\theta = 10^\circ$, we obtained an η of 99.1%. Assuming the experimental misalignment ($\delta < 100$ nm and $\theta < 1^\circ$), we concluded that the near-unity η can be achieved by the current transfer printing technology, if we prepare the PhC cavity with $Q_0 > 50,000$.

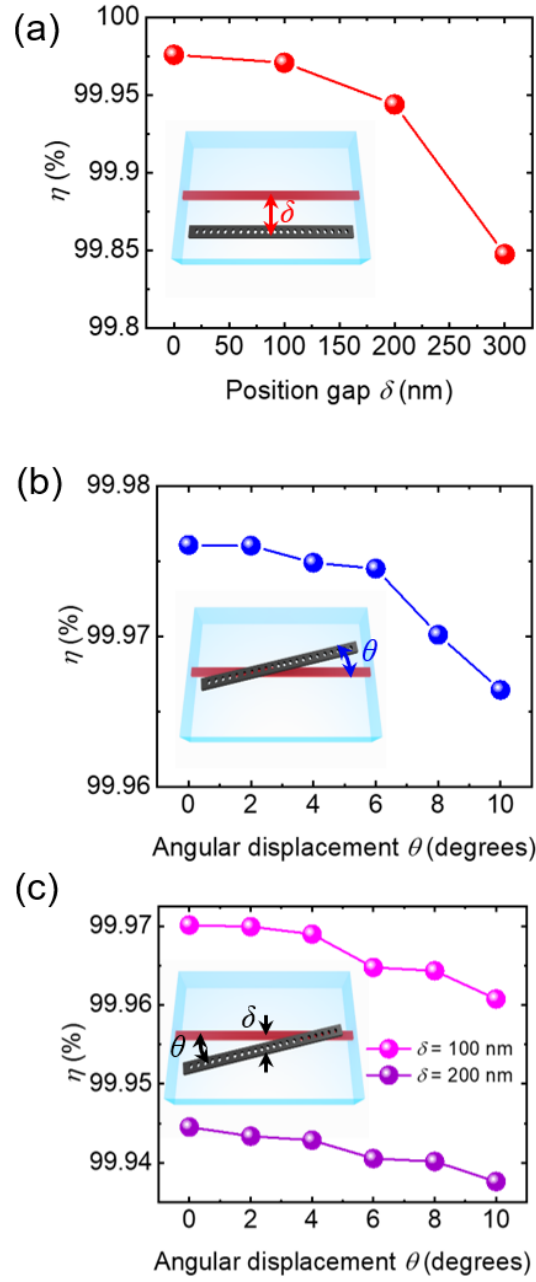


Figure 3.9: Summary of calculated η s under the presence of (a) the position misalignments δ , (b) angular displacement θ and (c) both finite δ and θ .

3.6 Simulated coupling efficiency with different material platforms

In this section, we show that our examining SPS structure is versatile for different material platforms. We investigated this feature by considering photonic waveguides based on Si and Si_3N_4 (assumed refractive indices of n_{Si} to be 3.5 and $n_{\text{Si}_3\text{N}_4}$ to be 2.0, respectively), both of which are common materials in the field of PICs. For the case of a Si photonic waveguide, we designed an InP nanobeam cavity (employed refractive index of n_{InP} to be 3.5 in this section). Figure 3.10(a) shows the schematic of the device design. In the cavity design, we set $w = 640$ nm, $h = 220$ nm, $a = 380$ nm, and $r = 99$ nm, while using the same modulation rule of the periods of the air holes described at the beginning of this chapter to define the cavity defect region. The fundamental mode of the investigated cavity has the resonant wavelength within the telecommunication wavelength band at 1.55 μm , where Si is optically transparent. Without the Si waveguide, the PhC nanobeam cavity placed on flat SiO_2 exhibits a very high quality factor of $Q_0 = 5.2 \times 10^6$ as well as a very small V of $0.463(\lambda/n)^3$. Then we set the Si photonic waveguide parameters as follows; a width of 400 nm and thickness of 210 nm. For the case when the cavity-waveguide distance of $d = 500$ nm, we deduced a near-unity η of 99.5% from the power distributions obtained in FDTD simulations. Figure 3.10(b) shows a field profile of the simulated mode at the steady state. We obtained the cavity quality factor $Q = 2,300$, which results in an η of 99.9% and well agrees with the simulated η . Based on the calculated values of Q and V , we deduced a β to be 99.8% and obtained an overall coupling efficiency of single photons as $\eta\beta = 99.3\%$ under these parameters.

For the case of a Si_3N_4 photonic waveguide, we used the same nanobeam cavity employed in this section. Figure 3.10(c) shows the schematic of the device design based on a Si_3N_4 photonic waveguide. We set the width of the Si_3N_4 photonic waveguide to be 1 μm and the thickness to be 400 nm. For the case when $d = 200$ nm, the designed SPS demonstrates a very high η of 99.1%. Here, we obtained a low quality factor of $Q = 7,900$, resulting in a high β of 99.9% and thereby near-unity $\eta\beta$ of 99.0%. Figure 3.10(d) shows a field profile of the computed resonant mode at the steady state. These simulated results clearly show that our investigated SPS device structure is highly suitable for introducing highly efficient SPSs into diverse material platforms of PICs.

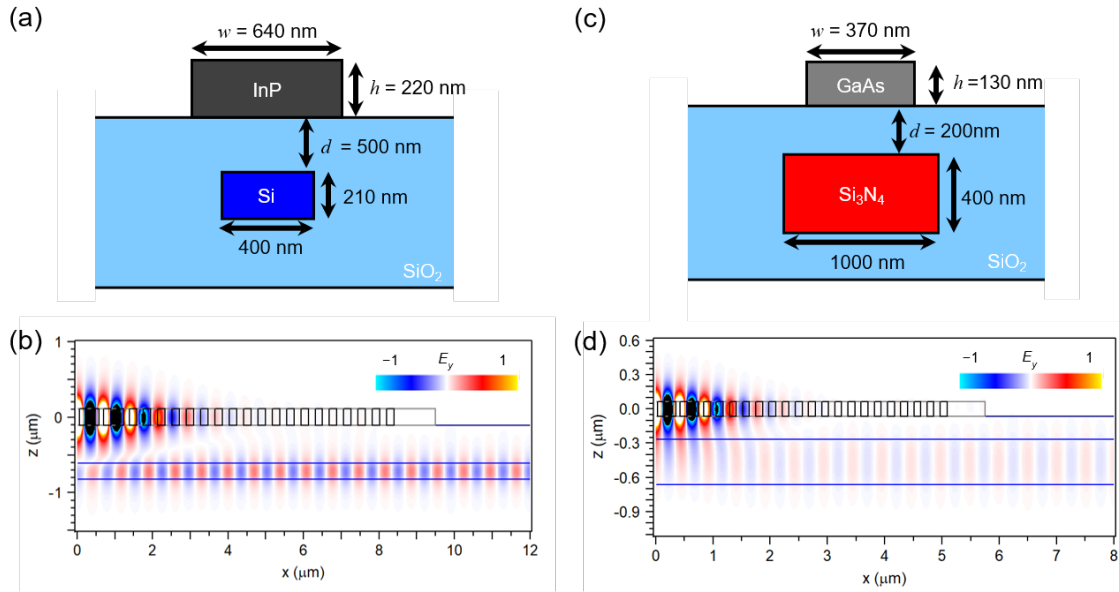


Figure 3.10: (a) Cross-section of the schematic Si waveguide-coupled InP-based QD SPSs. (b) Simulated cross-sectional field profile of the investigated cavity mode (E_y) coupled to the Si photonic waveguide. (c) Cross-section of the schematic Si₃N₄ photonic waveguide-coupled GaAs-based QD SPSs. (d) Simulated cross-sectional field profile of the investigated cavity mode (E_y) coupled to the Si₃N₄ photonic waveguide.

3.7 Summary

In this chapter, the theoretical work for an efficient QD SPS device structure was presented. Since transfer printing enables us to perform the individual fabrication of each optical component, it is possible to design on-chip SPS structure flexibly. The numerical simulations showed that our SPS structure's design enabled the coupling of single-photon emission from QDs into the photonic waveguide over 99%. Notably, this near-unity efficiency can be maintained even under the position misalignment of transfer printing or even under the material change.

Chapter 4

Fabrication and characterization of QD single-photon source transfer-printed on photonic waveguide

To fabricate the efficient SPS structure designed in chapter 3, many efforts were paid to construct the transfer printing apparatus, by which QD SPSs can be integrated on a photonic waveguide with high position accuracy and high yields. In this chapter, we describe the fabrication methods for integrating QD SPSs on glass-cladded photonic waveguide. The investigation of the transfer printing technique is described. The method to characterize the completed device is also explained. Experimentally, we demonstrated efficient single-photon coupling into a GaAs photonic wire waveguide, together with the integration of two SPSs into a GaAs waveguide.

4.1 Overall integration procedure based on transfer printing

Figure 4.1 shows the schematics of our overall transfer printing-based integration procedure. The process started with the fabrication of airbridge SPSs on a QD wafer by patterning an array of PhC nanobeam cavities. The airbridge SPS was picked up by the attachment and subsequent quick peel off of the transparent rubber stamp. In parallel, we prepared another wafer for photonic waveguides, which is glass-cladded to place the SPS above the waveguide (we utilized GaAs photonic wire

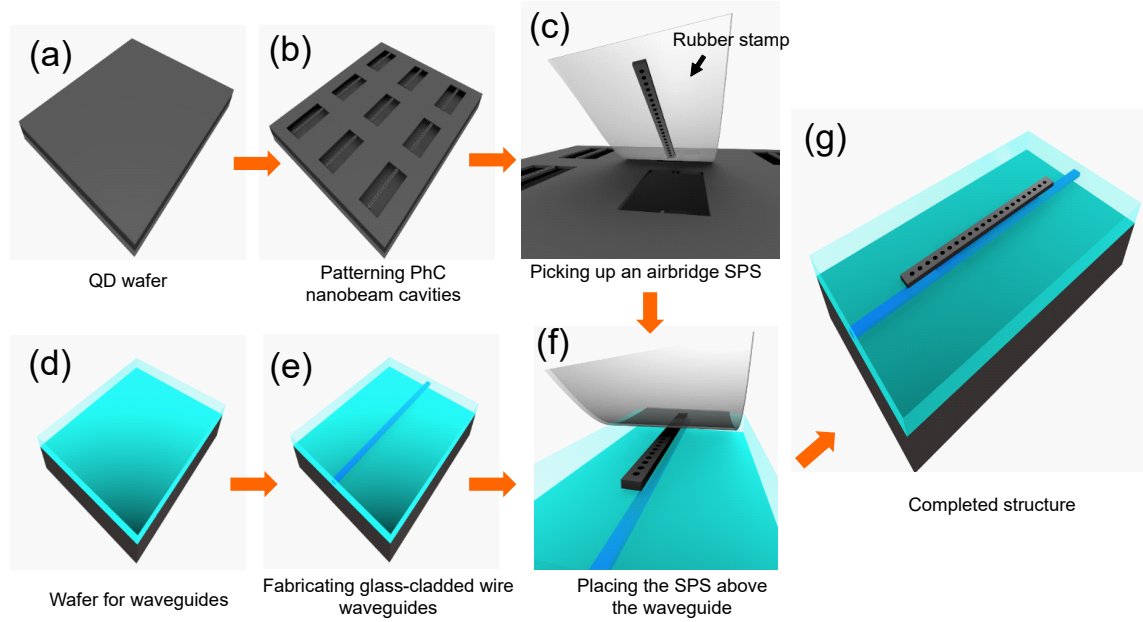


Figure 4.1: Schematics of our overall transfer printing-based integration procedure. The process started with the fabrication of SPSs on (a) a QD wafer, by patterning (b) an array of PhC nanobeam cavities. (c) The airbridge SPS was picked up by the attachment and subsequent quick peel off of the transparent rubber stamp. Concurrently, we prepared (d) another wafer to form (e) glass-cladded photonic wire waveguides. GaAs-based photonic wire waveguides were employed in this chapter. (f) The picked-up SPS was transferred by placing it onto the prepared waveguide and slowly releasing the stamp. (g) Schematics of the completed QD SPS structure.

waveguides in this chapter). The picked-up SPS was transferred by placing it above the prepared waveguide and slowly releasing the stamp. A schematic of the final waveguide-coupled SPS is shown in Fig. 4.1(g). This structure enables us to obtain near-unity coupling of QD emission into the waveguide, as discussed in chapter 3. As can be seen in Figs. 4.1, transfer printing largely simplifies the required 3D integration of the optical elements, enabling us to demonstrate QD-based SPSs with efficient QD-to-waveguide coupling and the dense integration of multiple SPSs into a single photonic waveguide.

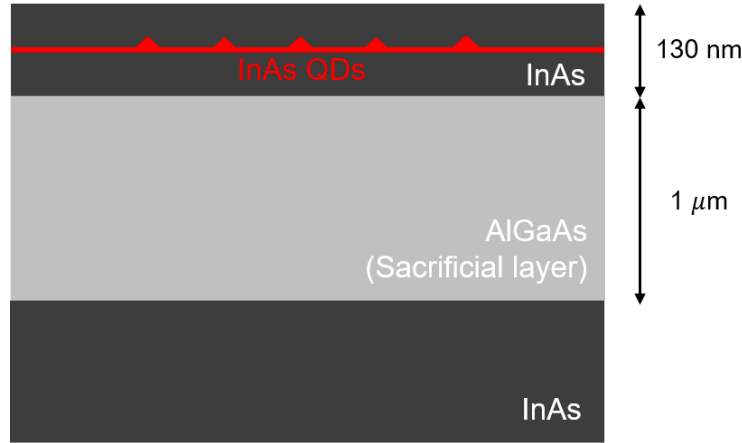


Figure 4.2: The structure of the sample wafer utilized in this study.

4.1.1 Fabrication of GaAs photonic crystal nanobeam cavity

In this section, we describe the preparation of the nanocavity-based QD SPSs [Figs. 4.1(a) and (b)]. For the efficient waveguide-coupled SPSs, it is important to fabricate high-Q PhC cavities. We show the details of nano-fabrication processes to address this issue.

Sample growth of GaAs slab containing InAs QD

We prepared a wafer sample of self-assembled GaAs/InAs QDs by molecular beam epitaxy (MBE). Figure 4.2 shows the structure of the wafer utilized in this study. The single QD layer is located at the middle of the 130 nm-thick GaAs slab grown on a 1 μm -AlGaAs sacrificial layer. The areal density of the QDs is 10^8 cm^{-2} . The growth of the QD sample was performed by Dr. Masahiro Kakuda.

Electron beam resist spin coating

We employed ZEP 520A (ZEON Corp.) as an electron beam (EB) resist. After the EB lithography, this EB resist works as a pattern mask for the dry etching process. We placed a few drops of ZEP 520A on the sample chips. We spread the resist by using the spin coater, which operates at speeds of 5,000 rpm for 1 minute (the spin coater's initial speed is 500 rpm for 5 s). Here, rpm stands for revolutions per minute. After spin coating, we baked the EB resist at 180 $^{\circ}\text{C}$ for 2 minutes using the hot plate, which resulted in the resist thickness of 320 nm.

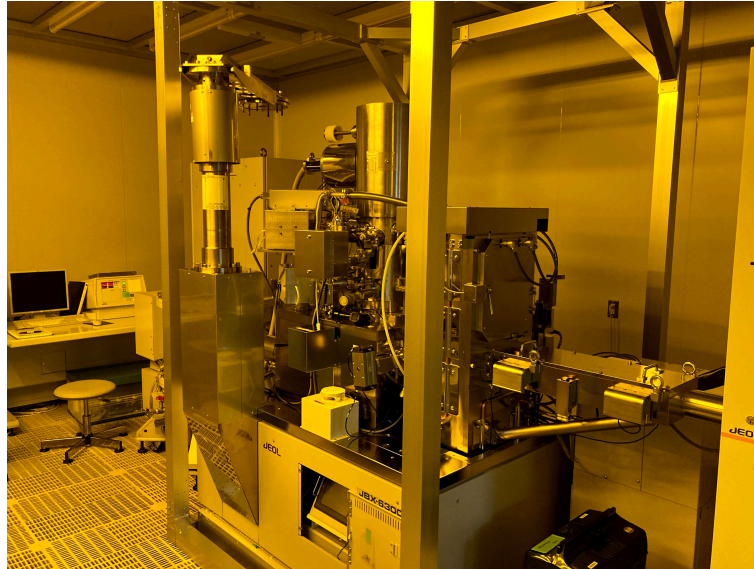


Figure 4.3: Photography of the EB lithography machine used in this study.

Electron beam lithography

The electron beam lithography is a direct writing technique that uses a beam of accelerated electrons to form a nano-meter scale pattern. This is done by accurately focusing a beam of electrons on a sample coated with EB resist. Since the focused electron beam changes the EB resists' solubility, the exposed area will be selectively removed after the development process. To pattern PhC structures on the resist, we used an EB lithography machine (JBX-6300FS, JEOL Corp.) as shown in Fig. 4.3.

Figure 4.4(a) shows a simple example of the lithography pattern to form the nanobeam cavity. However, when using this electron-beam pattern, the nanobeam will be distorted due to the scattering of accelerated electrons (proximity effects). To circumvent this issue, we alternatively utilized the patterns shown in Fig. 4.4(b) [95]. The area surrounded by blue lines will be removed out after the wet etching. To write the red (blue) area of this pattern, we set EB's dose as 250 (300) μC .

Development

To prepare the mask for the dry etching process, we developed the exposed EB resist on the sample using ZED-N50 (ZEON Corp.) together with ZMD-B (ZEON Corp.). Both ZED-N50 and ZMD-B were kept at 16 °C in a cool bath. First, we dipped the sample chip into ZED-N50 for 90 s. Subsequently, we transferred it to

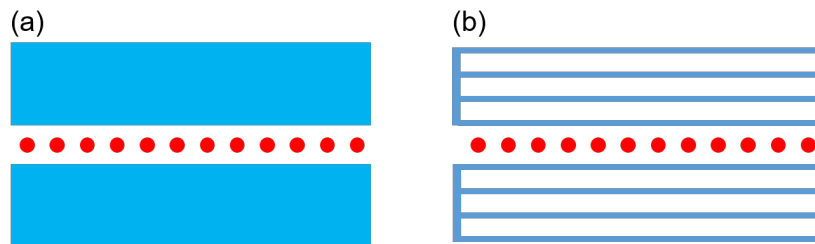


Figure 4.4: Electron beam patterns to form a nanobeam cavity. (a) Simple example, (b) Employed pattern in this study.

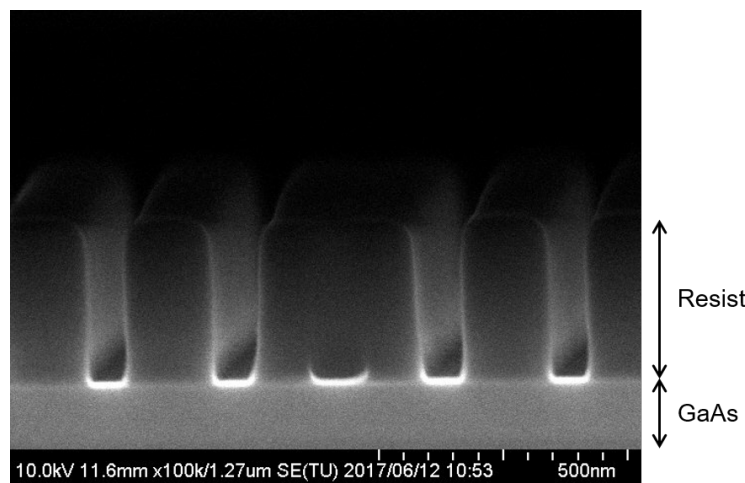


Figure 4.5: SEM image of the cross-section of the sample after the development.

ZMD-B, and the sample was rinsed for 1 minute. Then we dipped the sample in IPA for 10 s at room temperature. We baked the sample at 140 °C for 5 minutes using the hot plate for evaporating the rinse solution. Figure 4.5 shows an SEM image of the cross-section of the sample. We can see the smooth sidewall and vertical hole of the EB resist.

Dry etching

We dry-etched the sample by using the inductively coupled plasma (ICP) reactive ion etching (RIE) system, whose principle is shown in Fig. 4.6. RIE uses a combination of radical species and positive ions to remove material from the substrate. For etching the GaAs slab, we used Cl_2 and Ar for reactive and inactive gas, respectively. ICP is generated by using a strong electric field from an inductive coil around the

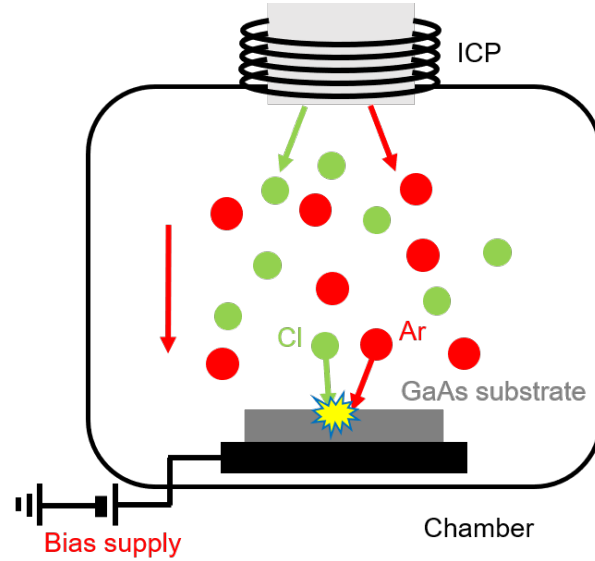


Figure 4.6: Principle of the ICP RIE system.

reaction chamber. Here, there are two types of etching processes. One process is the chemical ion etching, which is related to the chemical reactions between the etched sample layer and the neutral species generated in the plasma to form volatile compounds. These volatile compounds subsequently evaporate from the surface. The chemical etching allows low surface damage, high etch rate, and high selectivity. The other process is the physical etching caused by the surface bombardment with energetic ions. For this purpose, positive ions are accelerated by the self-bias effect provided from the bias RF power, resulting in the anisotropic etching.

In this study, we used the etching machine (Samco international, RIE-140iP), which is shown in Fig. 4.7. To realize a smooth sidewall of air holes in the sample slab, it is essential to keep the balance between the physical and chemical etching. We performed the dry etching based on the parameters listed in Table 4.1. The unit “sccm” stands for standard cc per minute, meaning the gas flow normalized under atmospheric pressure. Figure 4.8 shows an SEM image of the sample’s cross-section after the dry etching process. We can see the smooth sidewall and vertical hole in the GaAs slab, which is vital to realize high quality factor PhC cavities.



Figure 4.7: Photography of the ICP RIE machine used in this study (RIE-140iP).

Table 4.1: Utilized parameters for dry-etching GaAs slab.

Cl ₂	Ar	Pressure	Bias	ICP	Etching time
30 sccm	3.0 sccm	0.3 Pa	25 W	23 W	4 min

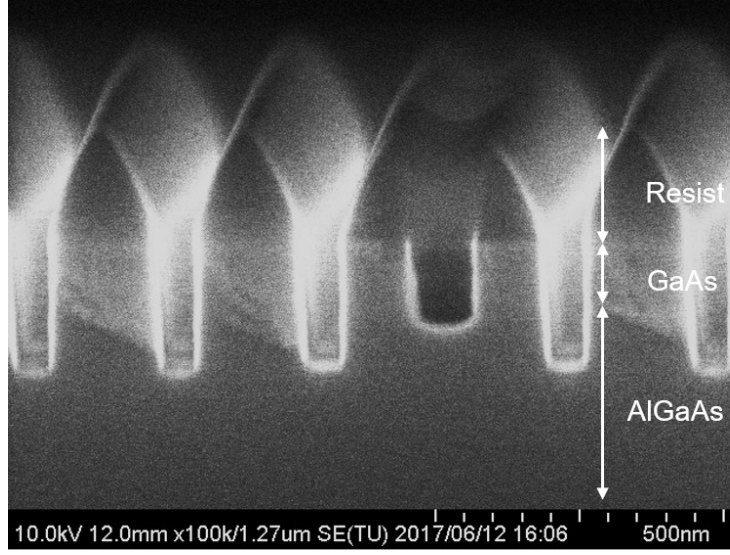


Figure 4.8: SEM image of the cross-section of the sample after the dry etching.

Removing electron beam resist

We removed the EB resist by using ZDMAC (Zeon Corp.) after the dry etching process. ZDMAC was kept at 55 °C in a heat bath. First, we dipped the sample into ZDMAC with ultra-sonication for 1 minute. To efficiently transmit ultrasonic vibration to the sample, we utilized a sample container made of iron. We again dipped the sample in ZDMAC for 10 minutes to completely remove the residual EB resist. Next, we cleaned the sample by dipping it in acetone for 3 minutes and IPA for the same minutes. Then we evaporated the residual solution on the sample by baking it for 5 minutes on the hot plate.

Wet chemical etching

We wet etched the sample using 50% hydrofluoric acid solution (HF, FUJIFILM Wako Pure Chemical Corp.) to form an airbridge sample structure. We diluted the HF solution by 20% with high-purity water (HF:H₂O = 1:4). We dipped the sample

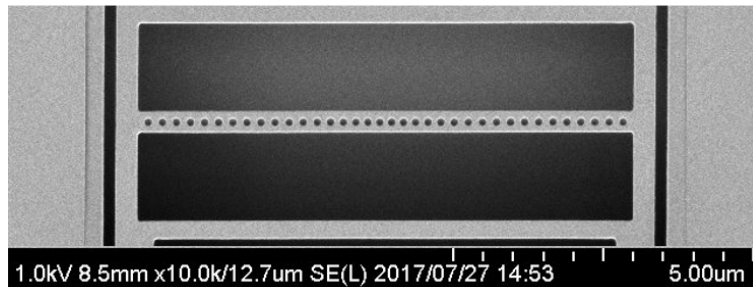


Figure 4.9: SEM image of the fabricated sample after the wet and digital etching.

in this HF solution for 20 s at room temperature. Then we rinsed the sample about 10 times using high-purity water.

Before picking up the sample from the rinse water, we removed the surface oxides using the digital etching technique. We diluted hydrogen peroxide (H_2O_2 , FUJIFILM Wako Pure Chemical Corp.) with pure water by 10% ($\text{H}_2\text{O}_2:\text{H}_2\text{O} = 1:9$). We dipped the samples into this H_2O_2 solution for 30 seconds to oxidize the sample and then rinsed the samples with high-pure water. Then, we prepared 1 mol/L solution of citric acid. We dipped the samples into this for 1 minute to etch the sample surface. Figure 4.9 shows an SEM image of the fabricated sample after the wet and digital etching. We can see that the sacrificed 1 μm -thick AlGaAs layer is completely dissolved. We can also confirm the smooth sample surface and sidewall of air-holes.

4.1.2 Fabrication of GaAs photonic waveguide embedded in glass

In this section, we describe the preparation of the glass-cladded GaAs waveguide [Figs. 4.1(d) and (e)]. We first prepared an air-bridged GaAs wire waveguide. Then we transferred them onto the flat SiO_2 glass and embedded them by a spin-on-glass (SOG) process.

Fabrication of air-bridged GaAs photonic wire waveguide

By using the same semiconductor nano-fabrication processes mentioned above, we fabricated airbridge GaAs wire waveguides with a thickness of 130 nm, as shown in Fig. 4.10. The waveguide width was chosen to be 220 nm, as discussed in chapter 3. To extract the waveguide-coupled photons directly into free space, we terminated the waveguide by second-grating-based exit ports. We designed the second-order Bragg gratings based on [96].

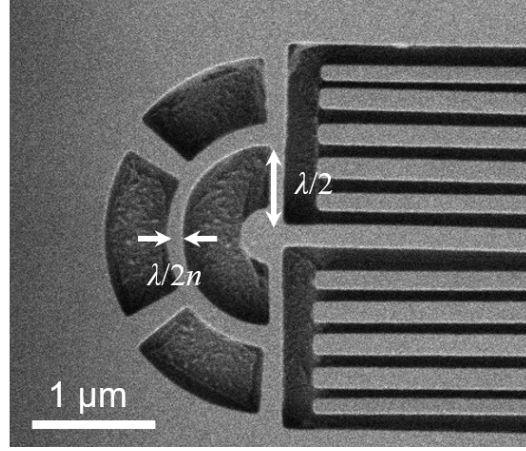


Figure 4.10: SEM image of the fabricated airbridge GaAs wire waveguide.

Spin-on-glass process

We embedded the waveguide by a SOG process. For this purpose, we placed the waveguides on a glass substrate by transfer printing, as discussed later. Then we formed an upper clad on the waveguide by using FOX15 (Dow Corning) mixed with MIBK (FUJIFILM Wako Pure Chemical Corp.). After spin-coating the solution on the sample, we baked it on the hot plate at 180 °C for 5 minutes. Here, we evaluated the thickness by using the SEM image, as shown in Fig. 4.11(a). We precisely controlled the thickness of the glass above the waveguide ($= d$) to be 300 nm by tuning the amount of solvent in the liquid glass material (FOX15 : MIBK = 5 : 4.5) and the spin speed (3000 rpm). We note that d was deduced from the cross-section of Fig. 4.11(b). We note that small amounts of humidity damage FOX15 in the atmosphere at room temperature. Therefore we mixed the solutions in a glove box filled with N_2 , and FOX15 was preserved in the refrigerator (below 0°C). We evaluated the clad surface's flatness above the waveguide by using an atomic force microscope (AFM). Figure 4.12 shows the AFM image of the sample surface, demonstrating that the surface was smooth with a root-mean-square roughness of only 0.4 nm.

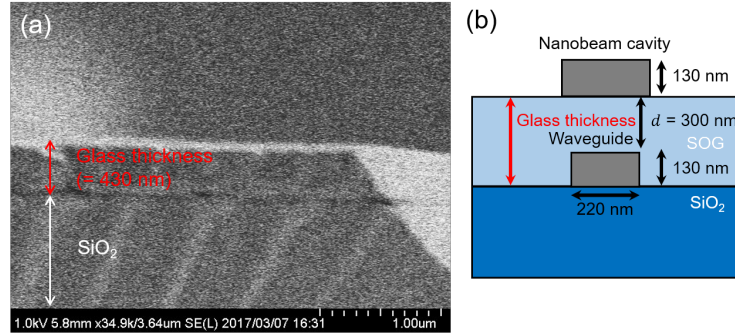


Figure 4.11: (a) SEM image of the cross-section of the SOG on a flat glass. (b) Schematic cross-section of our investigated device.

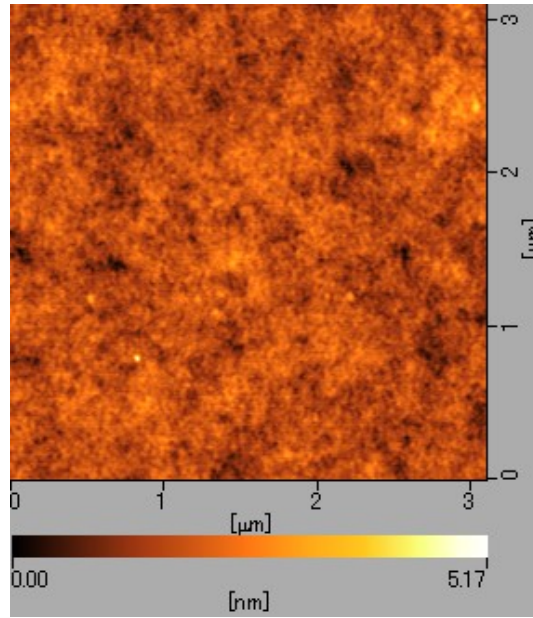


Figure 4.12: AFM image of the clad surface above the waveguide, demonstrating that the surface was smooth with a root-mean-square roughness of only 0.4 nm.

4.2 Transfer printing-based integration of nanocavity on photonic waveguide

In this section, we describe the integration of nanobeam cavities on the waveguide using transfer printing [Figs. 4.1(c) and (f)]. We intensively study the transfer printing technique by constructing a homemade transfer-printing apparatus.

4.2.1 Home-made transfer printing machine

We performed the transfer printing with a homemade transfer-printing apparatus, a photograph of which is shown in Fig. 4.13. Our apparatus is composed of two movable stages and an optical microscope. The system is placed on an anti-vibration table (TS-150, HERZ Corp.) for the accurate sample integration.

The left sample transfer stage (highlighted in green) holds a thin glass slide, on which a transparent rubber film is attached. This film was made of polydimethylsiloxane (PDMS, Sylgard184, Dow Corning). The PDMS film had $\sim 1\ \mu\text{m}$ -thick square pillars with a side length of $30\ \mu\text{m}$ for selectively picking up samples. Importantly, the pillar-like structure mitigated unwanted strain on the PDMS film by reducing the total contact area with the sample substrate, leading to improved positioning accuracy during the transfer process. Details of fabricating PDMS films with the pillar-like structure are discussed in the latter of this section. We can control the position of the stamp with fine adjusters in the three axes. With the top stage, we can also control the pitch and roll of the stamp, which is also important to obtain better positioning accuracy during the transfer printing process.

The right sample stage (highlighted in blue) holds the mother substrates for SPSs and waveguides on the top. This stage was equipped with fine adjusters and a three-axis piezo actuator (SFS-H60XYZ(CL), SIGMA KOKI), allowing us to tune the sample positions finely. The sample rotation can also be corrected using an incorporated manual rotation stage. We observed the sample with the microscope (highlighted in red), the magnification of which can be switched by rotating the turret equipping objective lenses (x5, x10, x50, and x100).

Now we describe the procedure of transfer printing processes. First, we attached a PDMS film to an appropriate air-bridged nanobeam cavity, as shown in Fig. 4.14(i). Then, we quickly peeled the film off by moving an actuator of the sample transfer stage in the vertical direction (Fig. 4.14(ii)). The peeling speed was approximately 3 mm/s. The success probability of this pick-up process was roughly 70~80% in the current apparatus. Next, we transferred the lifted nanobeam cavity onto a target

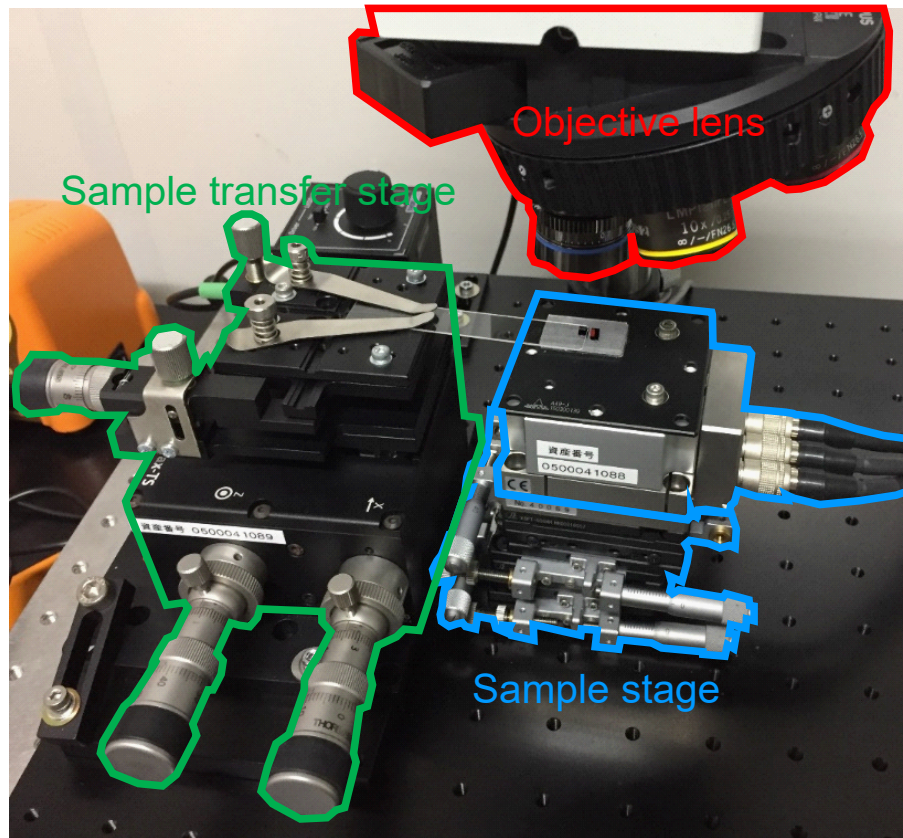


Figure 4.13: Photograph of the homemade transfer-printing apparatus. The left sample transfer stage (highlighted in green) holds a thin glass slide, on which a transparent rubber film is attached. The right sample stage (highlighted in blue) holds the mother substrates for SPSs and waveguides on the top. We observed the sample with the microscope (highlighted in red), the magnification of which can be switched by rotating the turret equipping objective lenses (x5, x10, x50, and x100).

waveguide. We carefully loaded the cavities above the waveguide manually using the piezo actuators (Fig. 4.14(iii)). During this loading process, we attentively tracked the cross markers patterned in both the marginal regions of the cavity and waveguide. The top cross markers of the cavity coupon looked slightly enlarged compared to those of the waveguide coupon, and the image contrast between the two elements served as a guide for precise sample positioning. Figure 4.14(iv) shows a snapshot of the printing process by slowly peeling the stamp off. We succeeded in this release step almost without fail in the current transfer condition.

A microscope image of a completed device is shown in Fig. 4.15 (Inset: SEM image of the completed device). The loaded SPS was tightly bonded on the waveguide clad via van der Waals force [97]. To evaluate the printing accuracy of the transfer printing technique, we integrated 8 different nanocavities on a waveguide with the same design and measured them with a high-resolution optical microscope. Based on the picture's digital edge enhancement, we deduced each element's perimeter, which was employed to determine the center positions of the cavity and waveguide. The absolute positioning error between the cavity and waveguide in the y direction was estimated to be ~ 60 nm on average. We also estimated the standard deviation of the error to be ~ 40 nm. From the pictures of Fig. 4.15, unwanted sample rotations are found to be $< 1^\circ$.

4.2.2 Fabrication of patterned rubber stamp

We fabricated the PDMS film with the pillar-like structure to reduce the total contact area with the sample substrate and mitigate unwanted strain on the PDMS film. This is highly important for an improvement in positioning accuracy during the transfer process. The pillar structure can be formed using a photo-resist as a mold.

Preparation of mold using laser drawing

We employed AZ-1500 (Merck Corp.) as a photo-resist. After the laser drawing, this resist works as a mold for the dry etching process. We spread the AZ resist using the spin coater, which operates at speeds of 4,500 rpm for 45 s (the initial speed of the spin coater is 500 rpm for 5 s). After spin coating, we baked the EB resist at 90°C for 10 minutes using the oven.

Then we drew the pattern on the resist by using the laser drawing machine ($\mu\text{PG101 SW2}$, Hidelberg Corp.), which is shown in Fig. 4.16. We patterned the simple square and circle structure (size: $20 \sim 30\ \mu\text{m}$) with a pitch of $\sim 200\ \mu\text{m}$. The

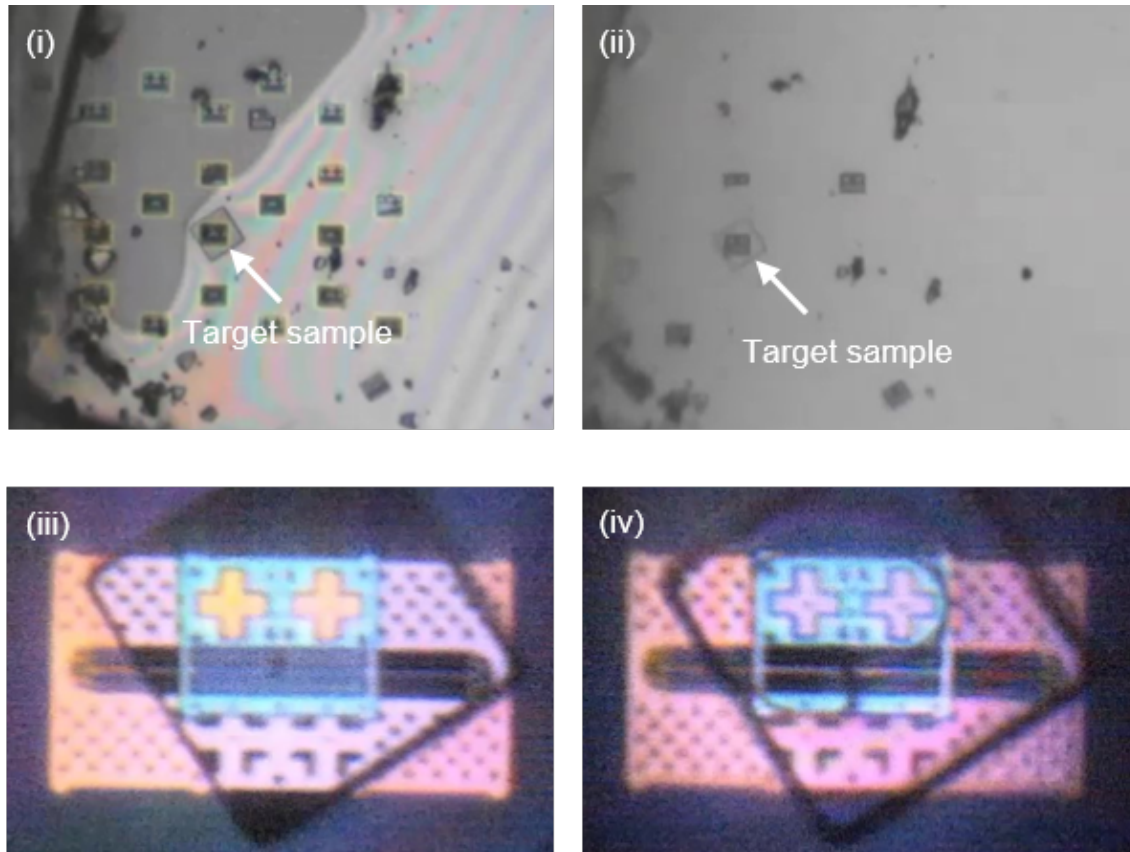


Figure 4.14: Microscope images taken at each step of the transfer printing process. (i) We attached a PDMS film to an appropriate air-bridged nanobeam cavity. (ii) We quickly peeled the film off by moving an actuator of the sample transfer stage in the vertical direction. (iii) We transferred the lifted nanobeam cavity onto a target waveguide, and carefully loaded the cavities above the waveguide manually using the piezo actuators. (iv) We slowly peeled the stamp off to release the cavities on the target waveguide.

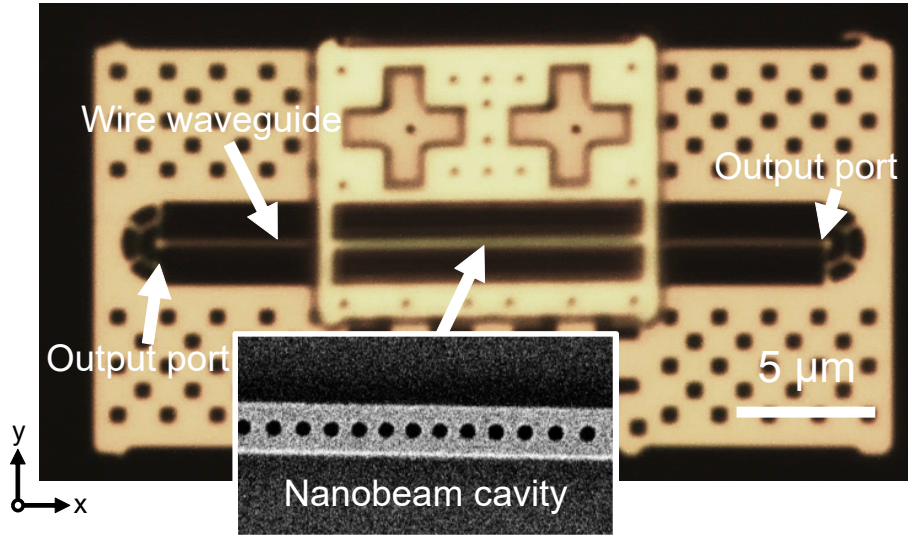


Figure 4.15: Microscope image of a completed device (Inset: SEM image of the completed device).

laser power was reduced 25% from 7 mW. The wafer was developed using NMD-3 (ZEON Corp.) for 1 minute.

Spin coating polydimethylsiloxane (PDMS)

We employed PDMS of Sylgard184 as a silicon rubber film. Sylgard 184 silicone elastomer consists of two-part liquid components, a pre-polymer base, and a cross-linking curing agent, that were mixed in 10:1 mass ratio. We spin-coated the developed wafer by using this mixture. The spin coating was done at 200 rpm for 5 s and 1000 rpm for 150 s. After the spin coating, we cured the PDMS at 100 °C for 5 minutes with an additional cure temperature of 150 °C for 10 minutes using the hot plate. Figure 4.17 shows an SEM image of the pillar structure of the PDMS.

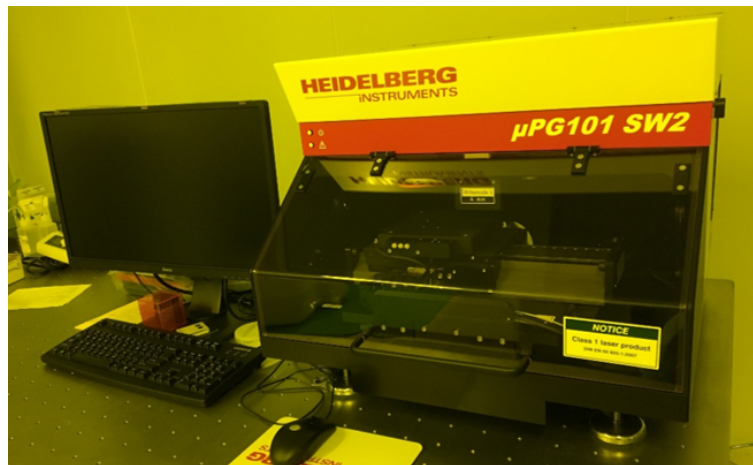


Figure 4.16: Photograph of the laser drawing machine.

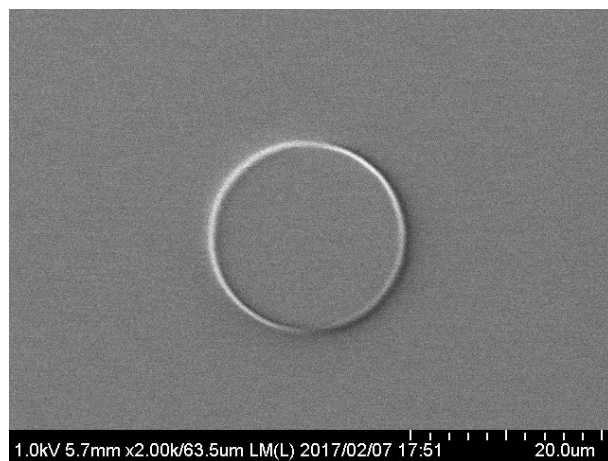


Figure 4.17: SEM image of the pillar structure of the PDMS.

4.3 Optical characterization setup

In this section, the optical setup to characterize the completed device is explained. Figure 4.18 shows a schematic overview of the constructed cryogenic temperature μ PL measurement setup on an optical table (RS4000, Newport). We used a liquid helium flow cryostat (HighResoII, Oxford instruments) to cool down the fabricated device around 4 K and keep the quantum nature of the InAs/GaAs QDs. We chose a liquid helium container (Stratos 100SL-J, Messer Cryotherm) whose height is almost close to that of the cryostat entrance to avoid unwanted strain on the system. The cryostat has a very short working distance of about 2.2 mm (depending on the sample thickness) with a window thickness of 1.0 mm to use a high magnification objective lens to correct the signal effectively. The cryostat was placed on a stage equipped with a two-axis piezo actuator, allowing us to control the sample positions precisely.

For optically pumping the QDs, we used the following laser sources: CW diode laser oscillating at 808 nm, pulsed Ti:sapphire laser, and CW Ti:sapphire laser. To guide the laser light to the device, we used a 92/8 pellicle beam splitter. To image the devices, focus a pump laser beam on devices and collect PL signals, we utilized an objective lens with N.A. = 0.65, working distance of 4.5 mm and cover glass correction up to 1.2 mm (LCPLN50XIR, Olympus Corp.). When we took the image of devices, we illuminated them by using a LED, which was sent to the devices and then captured by a CCD (charge-coupled device) camera (1/2" WAT-902H2, Watec).

The collected PL was then send to a grating spectrometer (Acton SP2750, Princeton Instruments) equipped with an Si CCD camera (PIXIS 400BR eXcelon, Roper Scientific). We chose a achromatic doublet lens with a focal length of 100 mm (magnification x28) to focus the image onto the slit, whose F number (~ 20) is larger than that of the spectrometer (focal length = 750 mm) for ensuring low loss. The spectrometer has three gratings with groove densities of 600 mm^{-1} , 1200 mm^{-1} and 1800 mm^{-1} , which can be switched by rotating the turret by a motor.

When measuring time-resolved spectra and intensity correlation functions $g^{(2)}[t]$, the signals were sent to the photon counter after the spectrometer. Here, the spectrometer functioned as a band-pass filter to exclude unwanted signals. To obtain time-resolved PL spectra, we employed the time-correlated single-photon counting (TCSPC) technique.

TCSPC technique is based on the detection of single photons from a periodic light signal. Figure 4.19 illustrates the measurement principle of TCSPC technique. By measuring the time difference between two signals (one is from a single photon sensitive detector and the other is from a reference signal from, e.g., a pulsed laser) over a consecutive series of very short periods, we can indirectly reconstruct

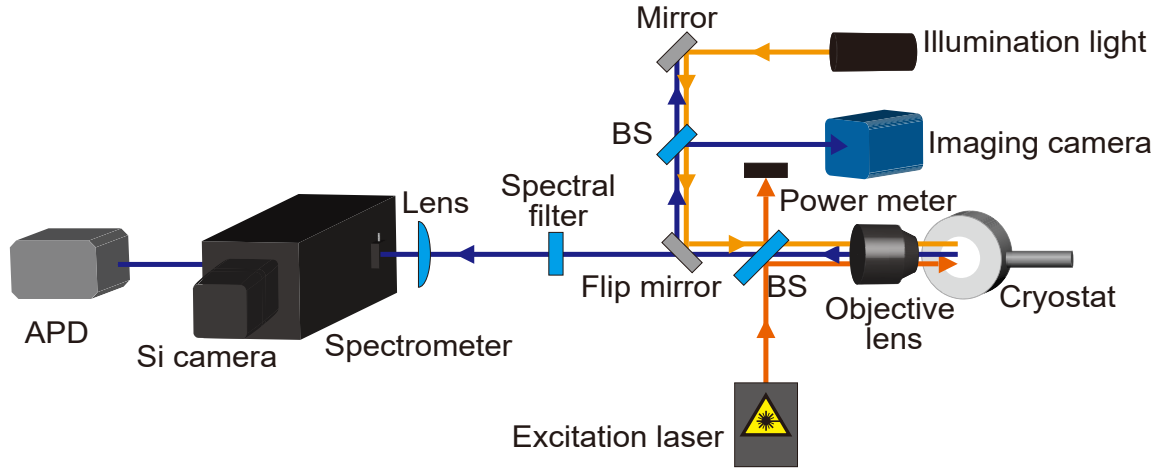


Figure 4.18: Schematic overview of the constructed cryogenic temperature μ PL measurement setup.

the original time-dependent waveform. The time difference between excitation and emission is determined by electronics that act like a stop-watch. Since the signal's pulse repetition rate is much higher than the photon detection rate, the detection of more than one photon per signal period is extremely unlikely.

During many cycles, no photons are detected. A single photon is detected in some periods, and for a very few periods, more than one photon is detected. The stop-watch readings are sorted into a histogram consisting of a range of "time bins". The time bins width typically corresponds to the resolution of the stop-watch (some pico-seconds). After many photons have been detected, a histogram of the detection times relative to the laser pulse can be piled up, which corresponds to the decay curve of the original optical pulse. The detected photons can be synchronized by a TCSPC electronics unit with a reference pulse corresponding to the pulsed output of the excitation laser.

In this work, a commercial correlation histogrammer (Pico Harp 300, Pico Quant) was used for the counting electronics unit. We used an avalanche photodiode (APD, PerkinElmer Co., Ltd) in this chapter. We estimated the system's overall time resolution to be 400 ps, which is mainly limited by the timing jitter of the APD.

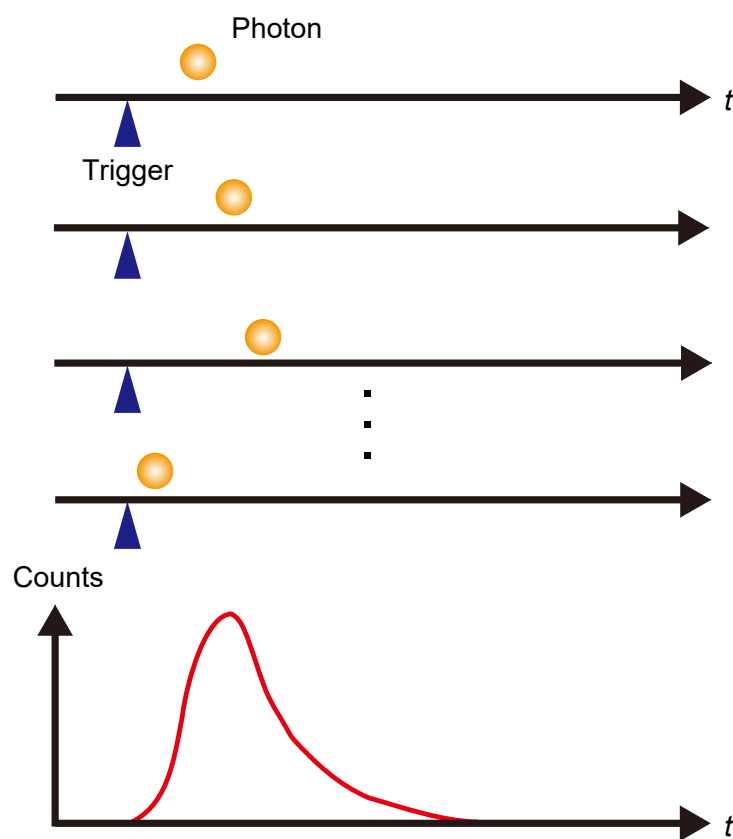


Figure 4.19: Measurement principle of TCSPC technique.

4.4 Optical characterization of waveguide-integrated quantum-dot single-photon source

4.4.1 PL image

We performed PL imaging of the fabricated device by pumping a CW Ti:sapphire laser (oscillation wavelength = 819 nm, excitation power = 25 μ W) onto the cavity center. Here, we inserted a bandpass filter (center wavelength = 900 nm) in front of an imaging camera to extract the investigated QD emission contribution. Figure 4.20(b) displays the PL image of the device at 7 K. We observed optical out-coupling from both of the exit ports [the dotted red circles in Fig. 4.20(b)]. These bright signals indicate efficient cavity-waveguide coupling.

To confirm that the optical pump of the cavity causes the above-mentioned optical coupling, we also took the PL image under the presence of the pump position shift. Figures 4.21 (a) and (b) display the PL image of the device while shifting the pump laser spot by 600 nm in x direction and 850 nm in y direction, respectively. For both cases, we observed no signals in from the exit ports [the dotted green circles in Figs. 4.21], further confirming that the bright signals in Fig 4.20(b) stems from the cavity emission.

4.4.2 PL spectra from exit port and above cavity

We measured PL spectra from one of the exit ports (red) and above the cavity center (green) at 7 K, as shown in Fig. 4.22. Here, we switched the pump laser to a pulsed Ti:sapphire laser (oscillation wavelength = 815 nm, averaged excitation power = 20 nW, repetition rate = 80.3 MHz, pulse width \sim 1 ps). For spatial filtering of the PL signal from out of the interested exit port, we limited the PL collection region by narrowing the entrance slit of the spectrometer and the region of interest of the CCD camera, roughly corresponding to the detection area of a few μm^2 .

In the red curve (upper panel), we observed an intense cavity mode emission (902.5 nm), together with cavity-coupled QD emission (902.2 nm). Besides, no other signals were observed in the red curve. On the other hand, in the green curve (lower panel), we cannot observe the cavity peak, which indicates that the photon leakage from the cavity into free space is suppressed and that the emission occurs predominantly into the waveguide. We consider that the largest perturbation for the cavity is provided by the waveguide, which is the main loss channel for the cavity photons and in turn suppresses the photon leakage into free space.

In this work, we did not pre-characterize PhC nanobeam cavities. We character-

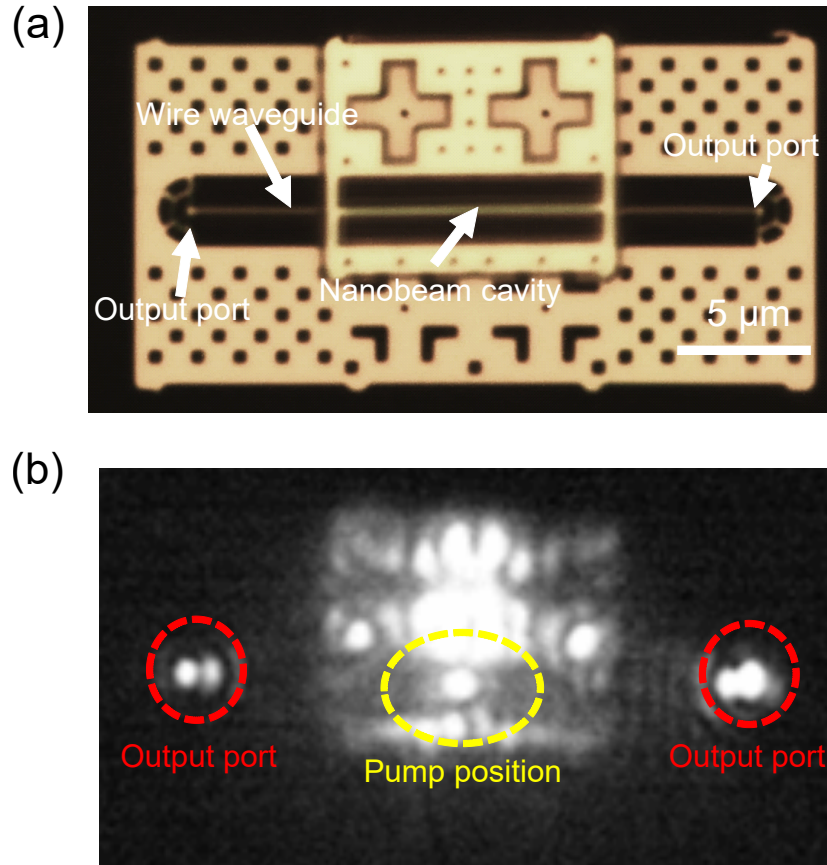


Figure 4.20: (a) Microscope image of the fabricated device. (b) PL image of the device at 7 K by pumping a CW Ti:sapphire laser onto the cavity center (oscillation wavelength = 819 nm, excitation power = 25 μW).

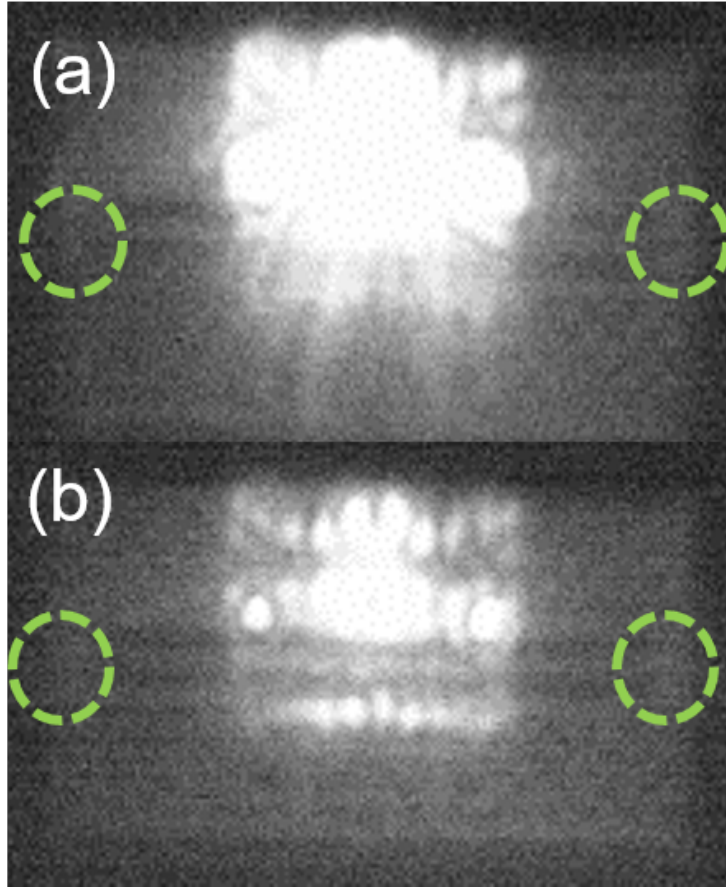


Figure 4.21: PL image of the device at 7 K while shifting the pump laser spot by (a) 600 nm in x direction and (b) 850 nm in y direction, respectively.

ized the fabricated SPSs after the transfer printing process. In this study, only one out of three to four devices contained QDs, which resonated with the cavity mode. The device discussed above was one of such devices. Pre-characterizing suitable QD SPSs can easily circumvent this randomness in the SPS fabrication by optical experiments before the transfer printing processes.

4.4.3 Evaluation of experimental cavity-waveguide coupling efficiency (η_{exp})

We evaluated the experimental cavity-waveguide coupling efficiency (η_{exp}) based on the measured cavity quality factors. By fitting the PL peak of the cavity mode with Lorentz function (solid black line in the inset of Fig. 4.22), we estimated the experimental cavity quality factor (Q_{exp}) to be 3,600. Next, we measured 9 nanobeam cavities that were placed on flat SiO₂ without the waveguide. By fitting the measured PL peaks with Voigt function, we deduced an averaged cavity quality factor on flat SiO₂ (Q_{ave}) to be 13,000. The standard deviation of the quality factors was estimated to be $\sim 1,000$. We note that the slightly larger Q_{exp} compared to the simulated quality factor ($Q = 1,300$ for $d = 300$ nm) can be explained by the deviation of the structural parameters in the fabricated device. Particularly, the cavity resonant wavelength shift hinders the phase matching between the cavity and waveguide, resulting in the degradation of their coupling efficiency. Notably, a more direct measurement of Q_{exp} will be possible by measuring the transmission spectrum of the waveguide-cavity coupled system [93].

Here, the experimental quality factors of Q_{exp} and Q_{ave} can be expressed by using the theoretical values of Q_0 and Q_{cav} in chapter 3 as follows:

$$\frac{1}{Q_{ave}} = \frac{1}{Q_0} + \frac{1}{Q_{fab}} \quad (4.1)$$

$$\frac{1}{Q_{exp}} = \frac{1}{Q_{ave}} + \frac{1}{Q_{waveguide}}, \quad (4.2)$$

where Q_{fab} is a quality factor related to the loss of photons through light scattering due to fabrication imperfections. Using the obtained values of Q_{exp} and Q_{ave} and above equations, we deduced an η_{exp} of 72% based on the following equation:

$$\eta_{exp} = \frac{1/Q_{waveguide}}{1/Q_{waveguide} + 1/Q_{ave} + 1/Q_{scatter}} = \frac{1/Q_{exp} - 1/Q_{ave}}{1/Q_{exp}}. \quad (4.3)$$

In this equation, we assume that the observed reduction of the quality factor when introducing the waveguide is mainly caused by the leakage of cavity photons into the

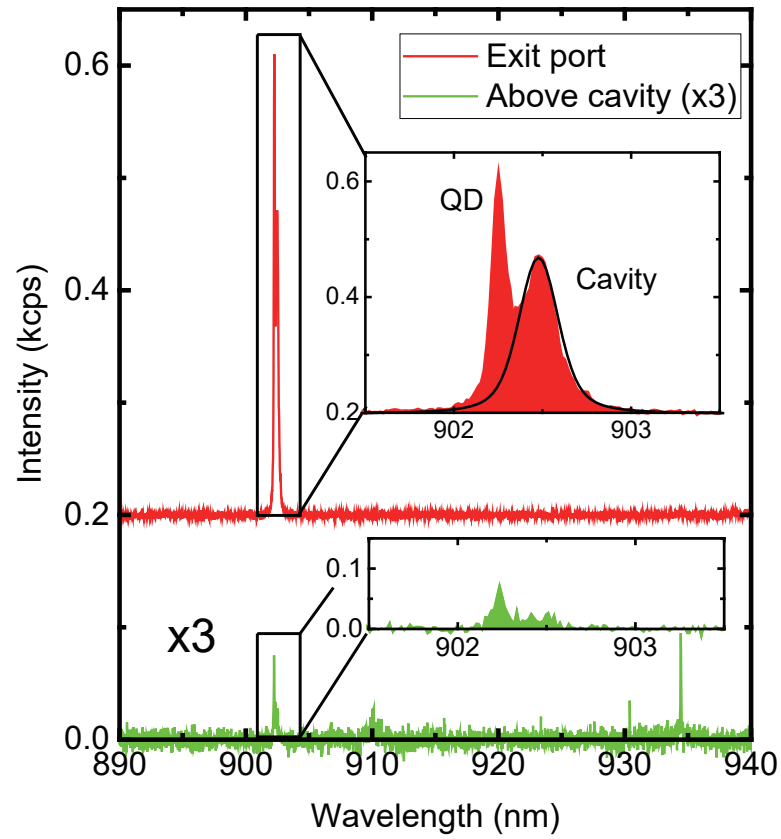


Figure 4.22: Measured PL spectra from one of the exit ports (red) and above the cavity center (green) at 7 K.

underneath waveguide ($1/Q_{\text{waveguide}} \gg 1/Q_{\text{scatter}}$). This assumption is reasonable for the current case where the cavity-waveguide distance is large enough to suppress the additional photon leakage from the cavity into free space, confirmed in the numerical simulations based on FDTD method shown in chapter 3. Even with fabrication imperfections (Q_{fab}), we can expect the dominance of the waveguide loss since the largest refractive index perturbation induces cavity photon leakage provided by the waveguide. Indeed, we had experimentally confirmed the significant suppression of free-space scattering of the cavity photons when cavities were coupled to the photonic waveguide, as discussed in chapter 3.

4.4.4 Observation of Purcell enhancement

We further performed detailed optical characterization for the fabricated device to confirm the Purcell enhancement of the extracted QD emission. Figure 4.23(a) displays a color map of the temperature-dependent PL spectra measured through the exit port by using the CW laser (oscillation wavelength = 849 nm, excitation power = 87 nW). We observed an enhancement of the QD emission around the cavity resonance [42, 44], while the intensity of the QD peak was diminished for large QD-cavity detuning. These results suggest the increase of emitter-cavity coupling due to the Purcell effect. For comparison, we also measured temperature-dependent PL spectra from above the cavity center, as shown in Fig. 4.23(b). The intensity of QD emission was decreased around the QD-cavity resonant condition, confirming that leakage of QD emission into free space was surely suppressed by the Purcell effect.

We also performed time-resolved PL measurements for the QD emission. For this purpose, we again switched the pump laser to a pulsed Ti:sapphire laser oscillating at 815 nm (averaged excitation power = 20 nW). We measured the time-resolved PL spectrum under the QD-cavity resonance, as shown in Fig. 4.24(a). To evaluate the emission rate of QDs, we fit the obtained time-resolved spectra with double exponential decay curves, $e^{-\kappa_1 t}$ and $e^{-\kappa_2 t}$ ($\kappa_1 > \kappa_2$) convolved with a response function reflecting the system time response. Among the two deduced time constants, we treated the faster decay rate κ_1 as the experimental value in the discussion. For comparison, we measured the time-resolved PL spectrum for QDs which were not inside a cavity but in an unprocessed sample region. We observed a rapid decay of the QD emission with a rate of $\gamma_{\text{exp}} = 3.9$ GHz (decay lifetime of 260 ps), which is 3.9 times faster than that of unprocessed QDs (as shown by the gray curve in Fig. 4.24(a)).

We evaluated the experimental emitter-cavity coupling efficiency (β_{exp}) based on

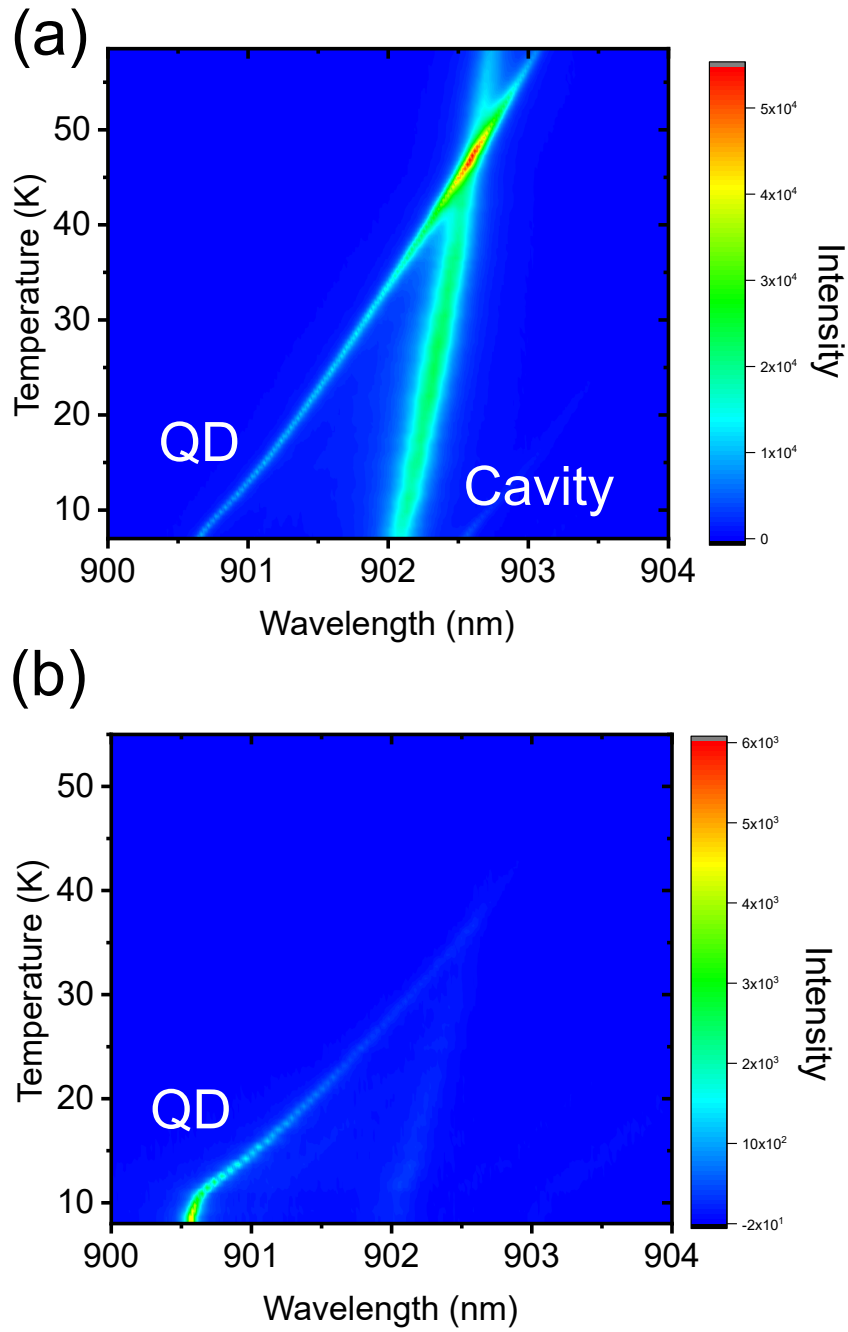


Figure 4.23: Color map of the temperature dependent PL spectra measured (a) through the exit port and (b) from above the cavity center by using the CW laser (oscillation wavelength = 849 nm, excitation power = 87 nW).

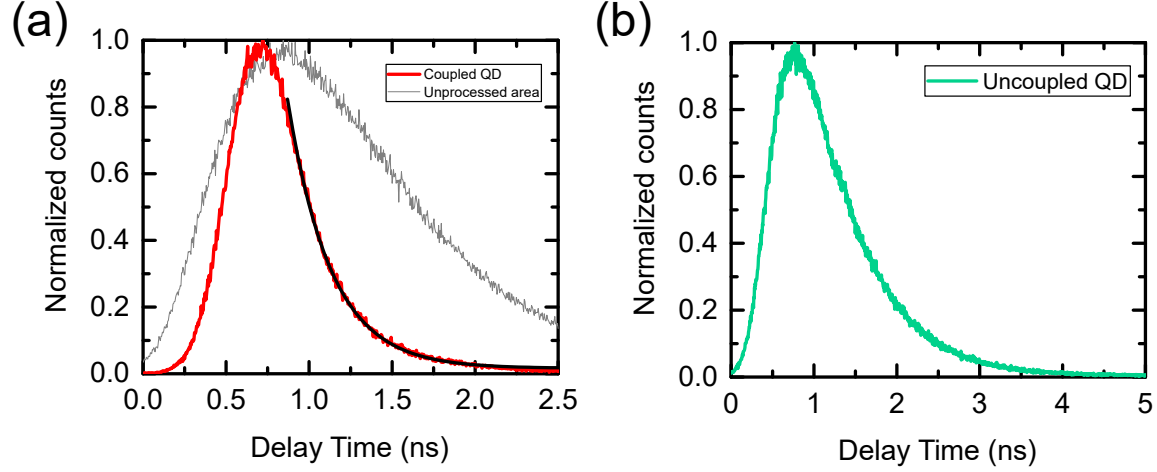


Figure 4.24: (a) Time-resolved PL spectrum measured for the investigated QD emission under the QD-cavity resonance. (b) Time-resolved PL spectrum measured for a QD that was embedded in a PhC nanobeam cavity on plane SiO_2 but uncoupled to any cavity resonant modes.

the measured emission rates of QDs. For this purpose, we measured emission decay rates of several single QDs that was embedded in PhC nanobeam cavities on plane SiO_2 but uncoupled to any cavity resonant modes, as shown in Fig. 4.24(b). The average decay rate was measured to be $\gamma_{\text{other}} = 0.5$ GHz, which is roughly half of that of QDs in an unprocessed sample area. The reduction of the decay rate γ_{other} is due to the partial photonic bandgap effect in the PhC nanobeam [92]. Then, we measured emission decay rates of the investigated QD emission peaks coupled to the cavity mode. Using the obtained values of γ_{exp} and γ_{other} , we deduced an β_{exp} of 87% based on the following equation:

$$\beta_{\text{exp}} = \frac{\gamma_{\text{exp}} - \gamma_{\text{other}}}{\gamma_{\text{exp}}}. \quad (4.4)$$

It is noteworthy that the estimation of β_{exp} based on lifetime measurements allows us to exclude the contribution of photon emission from the other indifferent QDs. This is important for us since our QD SPSs exhibit a certain level of cavity background emission provided by other QDs inside the cavity (roughly ~ 2 QDs on average in one cavity).

4.4.5 Overall emitter-waveguide coupling efficiency ($\eta_{exp}\beta_{exp}$)

We discuss the overall single photon coupling efficiency in experiment. This can be simply obtained by multiplying the two efficiencies, η_{exp} and β_{exp} . Given $\eta_{exp} = 72\%$ and $\beta_{exp} = 87\%$, the total single photon coupling efficiency is estimated to be $\eta_{exp}\beta_{exp} = 63\%$.

We primarily attribute this non-ideal $\eta_{exp}\beta_{exp}$ to the fabrication imperfection of the nanocavity, which degraded η_{exp} . The other possible reason for this non-ideal $\eta_{exp}\beta_{exp}$ in the current result is that β_{exp} did not take the maximum possible value probably because of the position deviation of the QD from the cavity field maximum (degrading the Purcell enhancement). If we can optimize the position of the QD, the maximum value of β_{exp} would reach to 99.7%. In addition, if we can optimize the waveguide-cavity distance ($d = 250$ nm), we can expect an increase of η up to 96.3%, with a slightly decreased β of 99.4%. As a whole, it would be possible to achieve a total single-photon coupling efficiency of $\eta\beta = 95.7\%$ even under the present quality of the nano-fabrication.

Meanwhile, a high quality factor $> 50,000$ for air-bridged PhC nanobeam cavities have been already demonstrated [98]. Very recently, a high quality factor of $\sim 160,000$ for air-bridged PhC nanobeam cavities have been already demonstrated [99]. With the high quality factor of 50,000, it would be possible to achieve $\eta\beta > 98.4\%$ for the case when $d = 250$ nm. Moreover, if we can obtain the ultra-high quality factor ($\sim 10^6$), the maximum possible $\eta\beta$ would become 99.6% for the case when $d = 300$ nm. These estimations imply that the near-unity single-photon coupling into the photonic waveguide is already within reach of the current nano-fabrication technology. It is noteworthy that the optimization of d for realizing the highest possible $\eta\beta$ depends on the achievable cavity quality factor Q_{ave} , since $\eta\beta$ is determined by the balance between the waveguide coupling and the Purcell effect which increases or decrease relative to the total quality factor Q_{exp} .

4.4.6 Measured evolution of spontaneous emission rate as a function of QD-cavity detuning

Figure 4.25 shows measured spontaneous emission rates of the QD plotted as a function of cavity-QD detuning. The fastest QD emission rate of 3.8 GHz was achieved at the emitter-cavity resonance (detuning = 0 nm). The emission rates became slower when QD was spectrally detuned from the resonance. These behaviors support our conclusion that the emission rate enhancement indeed originates from the Purcell effect in the nanocavity. The purple line in Fig. 4.25 shows a Lorentzian peak with the same linewidth of the cavity mode ($Q = 3,600$). The emission rate evolution did not match with the Lorentzian curve, being apart from the expectation from the conventional theory of the Purcell effect. We attributed this discrepancy to the coupling of the QDs to acoustic phonons. According to the reference of [100], the phonon-assisted Purcell effect in QDs supports a wide range of the emission rate enhancement. Indeed, the widened rate enhancement curve with a full-width half-maximum of 1.5 nm reasonably matched with those discussed in the literature.

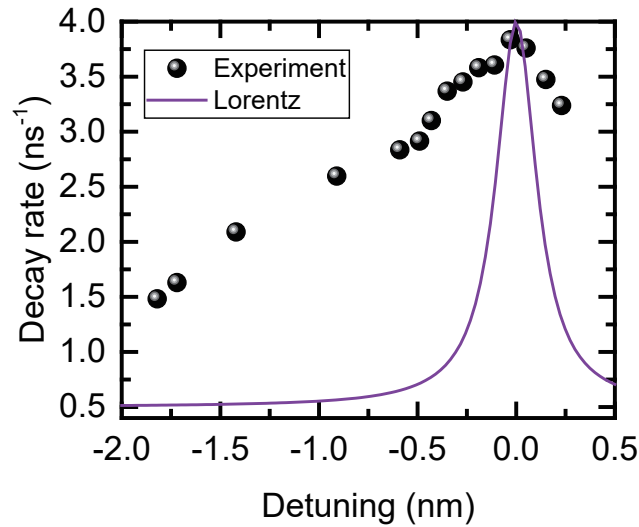


Figure 4.25: Measured spontaneous emission rates of the QD plotted as a function of cavity-QD detuning.

4.4.7 Observation of single-photon generation

To verify single-photon generation in the fabricated devices, we performed second-order correlation measurements based on a Hanbury Brown-Twiss setup. For obtaining the intensity correlation functions, we added a 50/50 beamsplitter, spectrometer, and APD to build a Hanbury Brown-Twiss interferometer. Due to the periodicity of the pulses, the photon correlation function consists of a series of peaks. Second-order coherence function under a pulsed excitation (which we defined as $g^{(2)}[t]$) was measured with slight QD-cavity detuning of 0.43 nm. The PL spectrum from the exit port is shown in Fig. 4.26(a)), which was obtained by using the pump laser to a pulsed Ti:sapphire laser oscillating at 815 nm with an averaged excitation power of 30 nW. Figure 4.26(b) shows a measured intensity correlation histogram. The $g^{(2)}[0]$ value was deduced by dividing the peak area of $t = 0$ by the averaged area of the remaining peaks. The histogram exhibits a clear anti-bunching with a zero delay time value of the second-order coherence function of $g^{(2)}[0] = 0.23$, demonstrating single-photon generation from the investigated QD. We consider that the relatively large $g^{(2)}[0]$ value originates primarily from the intrusion of the background cavity emission supplied by other off-resonant QDs embedded in the cavity and possibly from multiple pump-and-emission processes in the QD within an excitation pulse.

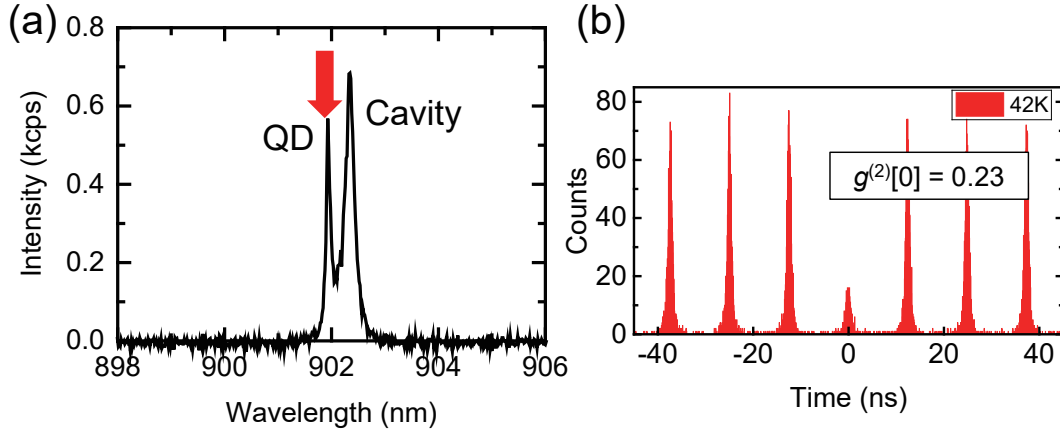


Figure 4.26: (a) Measured PL spectrum from one of the exit ports at 42 K. (b) Intensity correlation histogram measured for the investigated QD emission.

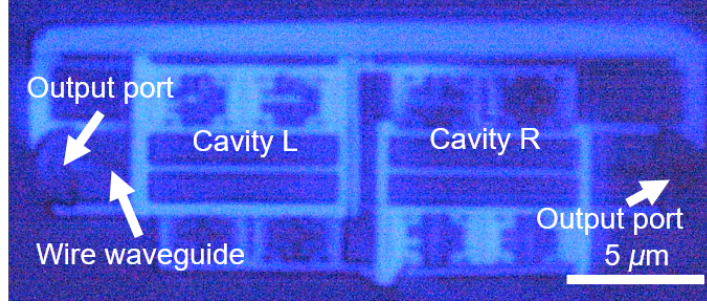


Figure 4.27: Microscope image of two integrated SPSs on a single photonic wire waveguide by repeating the transfer printing process.

4.5 Integration of two QD SPSs on a single chip

In this section, we extended our transfer printing approach to integrating multiple SPSs into a photonic waveguide, which will be required to realize large-scale quantum PICs. For this demonstration, we demonstrated the integration of two different SPSs by repeating the transfer printing process. Figure 4.27 shows a microscope image of the completed device. When integrating two nano-cavities into a single wire waveguide, we did not see a significant disturbance in the printing process by the pre-printed nanobeam cavity. This result suggests the possibility for densely integrated QD SPSs by using the transfer printing technique. In this regard, the parallel transfer of multiple photonic nano/micro-structures by transfer printing will also be of great importance for scalable integration [101, 102].

4.5.1 Single-photon transport under the presence of two cavities on a single waveguide

We verified that the integrated two cavities have little effect on each other regarding the single-photon coupling efficiency. For this purpose, we simulated light transport for the case that the two cavities are simultaneously integrated onto a single GaAs waveguide. We utilized two PhC nanobeam cavities (which we labeled as cavity L and R): they differ only in a (230 nm and 235 nm), while sharing the same parameters ($r/a = 0.26$, $w = 370$ nm and $h = 130$ nm). The two cavities resonate at 924 nm ($a = 230$ nm) and 937 nm ($a = 235$ nm) in the simulation. We selectively excited one of the two cavities to investigate the light propagation and simulated its evolution until the cavity mode reached the steady state in our numerical simulator. Figures 4.28(a) and (b) display the calculated cavity mode field profiles at the steady

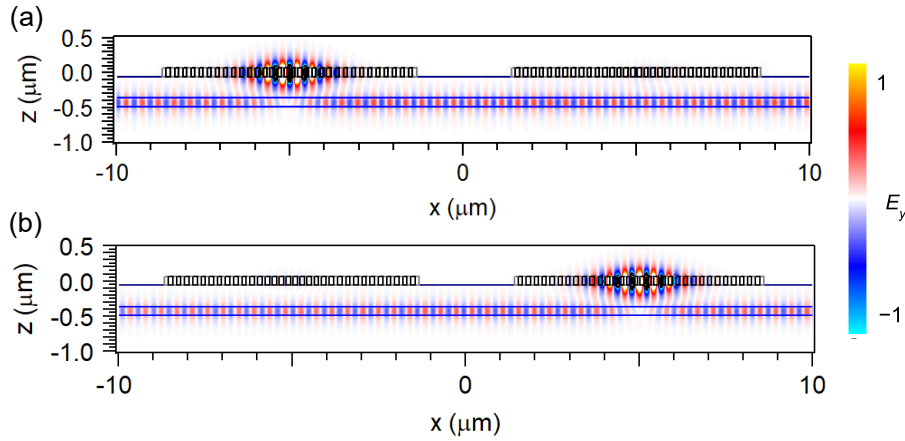


Figure 4.28: Calculated cavity mode field profiles at the steady states when two cavities are integrated on a single GaAs waveguide [(a) cavity L and (b) cavity R].

states. We can see that the light transport was not disturbed even under the other PhC cavity's existence. By monitoring the cavity mode's power distribution into the waveguide, we deduced η s over 99% for the waveguide coupling from the two cavities. We note that the minimal disturbance on light transport is mainly due to the large detuning between the two cavity resonant frequencies.

4.5.2 Demonstration of efficient cavity-waveguide coupling

We characterized the optical performance of the two QD SPSs by using PL measurements through the waveguide exit ports. We measured PL spectra from one of the exit ports at 3 K when individually pumping cavity L and R, as shown in Figs. 4.29(a) and (b). Through the study of two integrated QD SPSs, we used the pulse Ti:sapphire laser (831 nm, 3.8 μ W) as a pump laser. In order to achieve moderate cavity-QD detunings for both QD SPSs, we performed cavity tuning based on gas condensation technique [103]. We inserted Xe gas into the cryostat through the gas port, which effectively deposited the gas onto the device and thus allowed us to tune only the cavity wavelength via the change of the reflective index of the cavity. The maximum tuning range of the cavity wavelength by using this technique was about a few nm in our current setup.

For both SPSs, we observed strong QD emission peaks (which we labeled as QD-A, and B). From the PL spectra of Figs. 4.29(a) and (b), we measured a cavity quality factor of 1,000 (950) for the cavity L (R), resulting in the high experimental

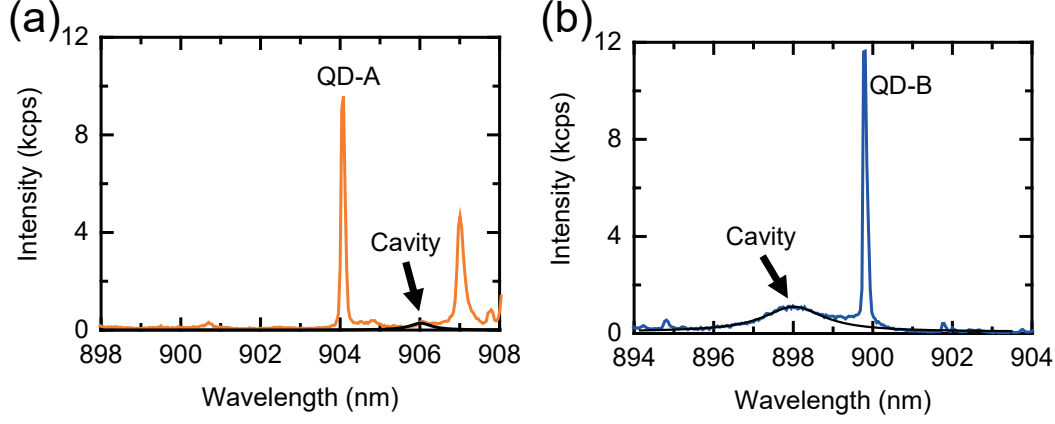


Figure 4.29: PL spectra measured from one of the exit ports at 3 K when individually pumping cavity L and R [(a) cavity L and (b) cavity R].

cavity-waveguide coupling efficiency of $\eta_{exp} = 92\%$ (93%).

4.5.3 Demonstration of efficient emitter-cavity coupling

We measured time-resolved PL spectra for QD-A and B through the exit port at 3 K, as shown in Figs. 4.30(a) and (b). Both QD emissions showed fast radiative decay rates, indicating their Purcell-enhanced emission into the cavity modes. For QD-A(B), γ_{exp} was measured to be 2.2 (1.2) GHz at 3 K, at which the QD peak was detuned from the cavity resonance by 2.0 (1.8) nm. From these results, we deduced experimental emitter-cavity coupling efficiency of $\beta_{exp} = 77\%$ (58%) for the QD-A (B), resulting in $\eta_{exp}\beta_{exp}$ of 71% (54%).

4.5.4 Observation of single-photon generation

We confirmed that both the QD emission peaks exhibit strong anti-bunching, as shown in Figs. 4.31(a) and (b). The obtained $g^{(2)}[0]$ value was 0.24 (0.25) for QD-A (QD-B), suggesting the successful integration of two SPSs into the same single waveguide.

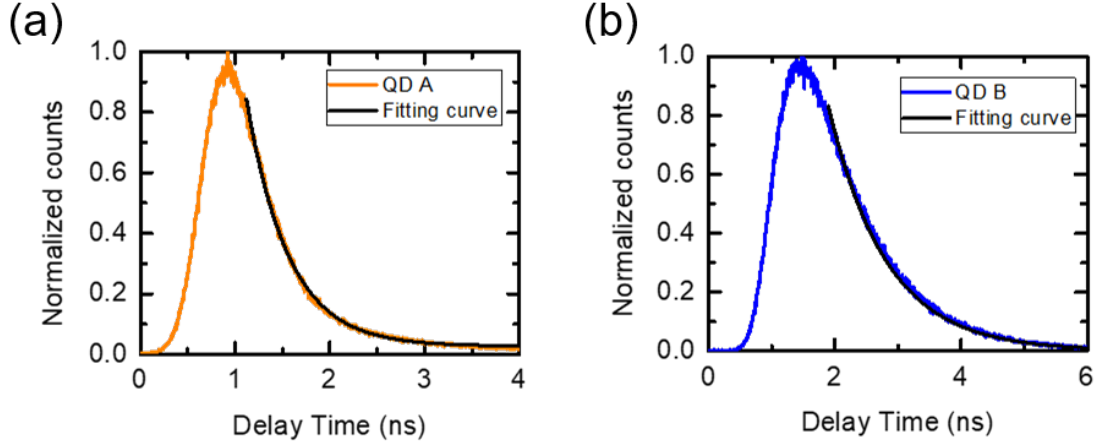


Figure 4.30: Time-resolved PL spectra measured for QD-A and B through the exit port at 3 K [(a) QD-A and (b) QD-B].

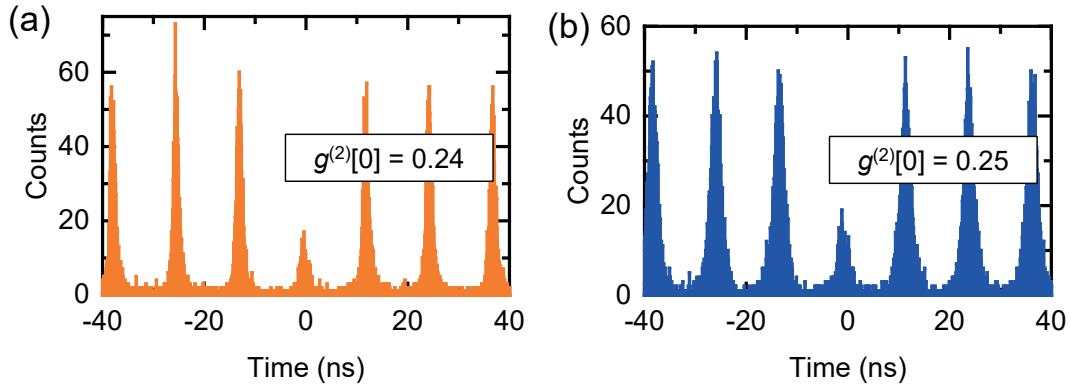


Figure 4.31: Intensity correlation functions measured for QD-A and B through the exit port at 3 K [(a) QD-A and (b) QD-B].

4.6 Summary

In this chapter, the hybrid integration technique using transfer printing was presented. To perform hybrid integration of QD SPSs with high position accuracy at high yield, lots of efforts were paid to develop transfer printing technology. Experimentally, the devices exhibited efficient coupling of single photons with coupling efficiency over 70%. Our transfer printing approach further made it possible to integrate two QD SPSs into a single photonic waveguide.

Chapter 5

Hybrid integrated QD single-photon source on silicon CMOS photonic chip

5.1 Introduction

Among the various PIC platforms [104], silicon photonics is one of the most attractive ones for implementing large-scale PICs [17, 18], by taking advantage of mature complementary-metal-oxide-semiconductor (CMOS) technology [105]. The silicon-based PIC technology also offers well-developed nanophotonic elements (e.g., high-Q micro-ring resonators, ultra-low-loss waveguides, optical beam splitters, efficient grating couplers, and optical modulators) that enable us to build highly functional and robust quantum PICs. Silicon quantum photonics exploits the power of silicon photonics and provides a fascinating route towards large-scale photonic quantum information processing [106, 107]. Silicon quantum PICs have already shown their promise for quantum key distribution [108–110], linear optical quantum computation [8, 111, 112], quantum teleportation [113] and boson sampling [62, 114]. However, current silicon quantum photonics is inherently lacking scalability because the silicon-based SPSs (e.g., those based on spontaneous parametric down conversion) have probabilistic emission nature [115].

Self-assembled QDs are especially promising SPSs because of their proven potential for deterministic operation with pure and indistinguishable single-photon generation [39–41]. QDs can also be engineered to generate single photons in the telecom wavelength region, where silicon is optically transparent [116–119]. However, their hybrid integration is inherently difficult since each epitaxial QD’s spectral and spa-

tial randomness hinders the deterministic integration of the desired QD on a proper location of the target PIC. This difficulty becomes more prominent when employing conventional heterogeneous integration techniques, such as wafer bonding and direct epitaxial growth; introducing such hybrid integration processes into existing CMOS foundry platforms is generally challenging since it is significantly difficult to modify CMOS foundry processes solely for new materials. Thus far, a few groups reported the hybrid integration of QD-based SPSs on silicon-based photonic platforms (including those based on Si_3N_4). However, none of them has succeeded in the hybrid integration of QD SPSs on a silicon waveguide that was processed using commercial CMOS fabrication.

This chapter describes the demonstration of a QD SPS integrated on a silicon waveguide processed by a CMOS foundry. Hybrid integration was performed using transfer printing. Since transfer printing relies on van der Waals force, QD SPSs can be assembled on chip after completing the entire CMOS process. The transfer printing approach is fully compatible with the CMOS back-end process and will open the possibility of constructing large-scale quantum PICs that take full advantage of matured CMOS technology. It is also possible to select QD SPSs with desirable optical properties before integrating them onto a target silicon PIC, allowing us to integrate multiple QD SPSs while circumventing their inherent randomness. To uncover a way to integrate QD SPSs on a silicon CMOS chip, QD SPSs were integrated onto a dry-etched glass surface of a CMOS chip by transfer printing. It was confirmed that integrated QDs are cooled down even on a foundry-processed silicon chip. We also observed single-photon generation from the integrated QD and its efficient waveguide coupling.

5.2 Device design for near-unity coupling of QD emission into silicon photonic waveguide

In this section, we performed numerical simulations to confirm that our SPS structure described in chapter 3 even supports the efficient coupling of single photons into a silicon waveguide. A QD-based SPS is placed on a glass-cladded silicon waveguide. Here, we considered a GaAs-based nanobeam cavity with a width of 450 nm and a thickness of 180 nm. For the nanobeam cavity, the radius of air holes is $r = 78$ nm, and the period of holes is $a = 300$ nm. We employed the same modulation rule for the cavity center as discussed in chapter 3, resulting in the formation of a high-Q PhC nanobeam cavity. For the cavity without silicon waveguides, the

fundamental mode of the cavity possesses a high quality factor of $Q = 5.4 \times 10^6$ and a small mode volume of $V = 0.43 \times (\lambda/n)^3$ with resonant wavelength of $\lambda = 1,170$ nm.

We optimized the cavity's optical coupling into the silicon waveguide by controlling the vertical distance between them (d). Figure 5.1(a) shows a cross-sectional schematic of the investigated device. To achieve phase-matching condition between the cavity mode and waveguide propagation mode, we set the silicon waveguide parameters as the width of 250 nm and thickness of 210 nm. Then we simulated the cross-sectional field profile of the investigated cavity mode (E_y) coupled to the silicon waveguide as shown in Fig. 5.1(b). We can see that the cavity fundamental mode is well funneled into the underlying silicon waveguide without noticeable light scattering into free space at $d = 450$ nm.

Figure 5.1(c) summarizes the coupling efficiencies and quality factors as a function of d . We can see an exponential reduction of Q as we reduce d , induced by the evanescent coupling of cavity mode into the silicon waveguide. This behavior well agreed with the results of chapter 3. Corresponding to the decay of Q s, we can see the increase of cavity-to-waveguide coupling efficiency η when d was reduced from 700 nm to 400 nm. For $d = 450$ nm, η is simulated to be 99.6% with the cavity quality factor of $Q = 6,200$. The decrease of Q in turn degrades the emitter-waveguide coupling efficiency (mainly for the case of $d < 450$ nm). Even under the case of low- Q conditions, we can still maintain a high β over 99.9% thanks to the large Purcell enhancement facilitated by the very small V . As a result, the overall single-photon coupling efficiency ($\eta\beta$) takes a maximum value of 99.5% at $d = 450$ nm. These numerical results demonstrate that our SPS structure is a powerful device design compatible with silicon photonics platforms.

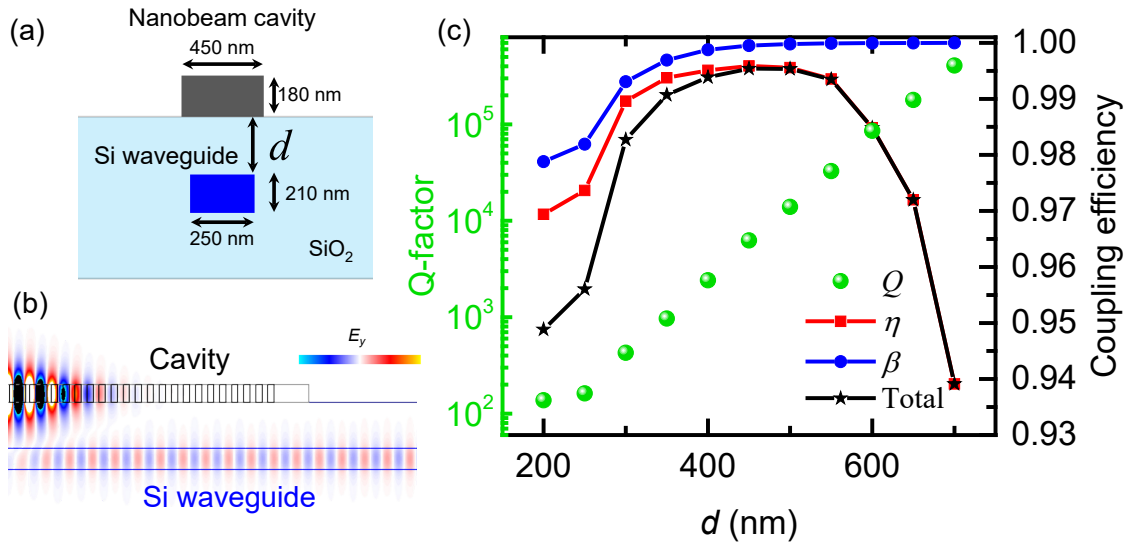


Figure 5.1: (a) Cross-section of the schematic silicon waveguide-coupled QD SPS. (b) Simulated cross-sectional field profile of the investigated cavity mode (E_y) coupled to the silicon waveguide. (c) Simulated coupling efficiencies and quality factors plotted as a function of d . Green circles : Q s. Red squares: η s. Blue circles: β s. Black stars: total single-photon coupling efficiencies ($\eta\beta$ s).

5.3 Procedure of integrating QD SPS on silicon CMOS chip based on transfer printing

In this section, we describe the procedure of fabricating the device based on transfer printing, as shown in Fig. 5.2. The process begins with the preparation of cavity-based QD SPSs. An airbridge SPS is picked up by attaching and quickly peeling off the transparent rubber stamp. Meanwhile, we outsource the preparation of CMOS-processed silicon waveguides. The picked-up QD SPS is transferred by placing it above the silicon waveguide and slowly releasing the stamp. By following these steps, we can assemble each component after completing the entire CMOS process.

5.3.1 Fabrication of air-bridged GaAs PhC nanobeam cavity

First, we fabricated nanocavity-based QD SPSs [Fig. 5.2(a)]. We patterned the 1D PhC nanobeam cavities into a GaAs slab (thickness = 180 nm) containing one layer of self-assembled InAs QDs. The QDs were grown by molecular beam epitaxy with an areal density of $5 \times 10^{10} \text{ cm}^{-2}$. We utilized using the same semiconductor nanofabrication procedure mentioned in chapter 4. For the wet etching process, we dipped the samples in IPA after rinsing the sample to circumvent the capillary effect. Due to the quick evaporation of IPA, the capillary effect becomes weaker, resulting in the low surface tension of the air-bridged samples. Thanks to this low surface tension, the nanobeam survived after pulling them out from IPA. Figure 5.3 shows an SEM image of a fabricated nanobeam cavity.

5.3.2 Preparation of CMOS-processed silicon photonic waveguide

We prepared glass-cladded silicon wire waveguides through a CMOS-process foundry [Fig. 5.2(b)]. The chip size is $8 \text{ mm} \times 2 \text{ mm}$. Figure 5.4(a) shows a microscope image of a silicon waveguide in this study. The waveguide's width and thickness were 250 nm and 210 nm, respectively, supporting an efficient waveguiding of TE fundamental mode at the wavelength of 1,170 nm (the effective refractive index of 2.1). The silicon waveguide is buried in a silicon dioxide layer formed by chemical vapor deposition. The thickness of SiO_2 above the waveguide is $2 \mu\text{m}$. At the ends of the waveguide, we implemented two output ports (a period of 670 nm and a duty cycle of 40%) to extract waveguide-coupled QD emission into free space directly. 3D FDTD simulations reveal that the coupling efficiency from the output

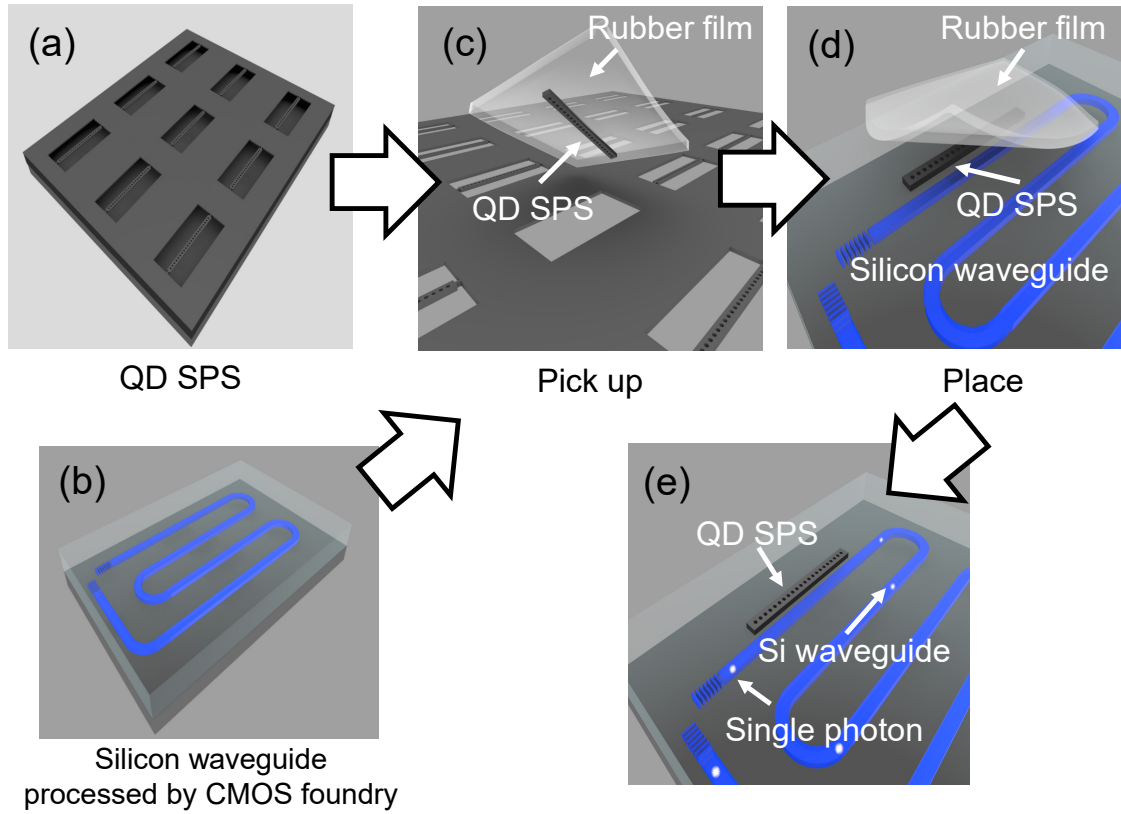


Figure 5.2: Procedure of fabricating the device based on transfer printing. The process begins with the preparation of (a) cavity-based QD SPSs. (c) An airbridge SPS is picked up by attaching and quickly peeling off the transparent rubber stamp. Meanwhile, we outsource the preparation of (b) CMOS-processed silicon waveguides. (d) The picked-up QD SPS is transferred by placing it above the silicon waveguide and slowly releasing the stamp. (e) Final device structure.

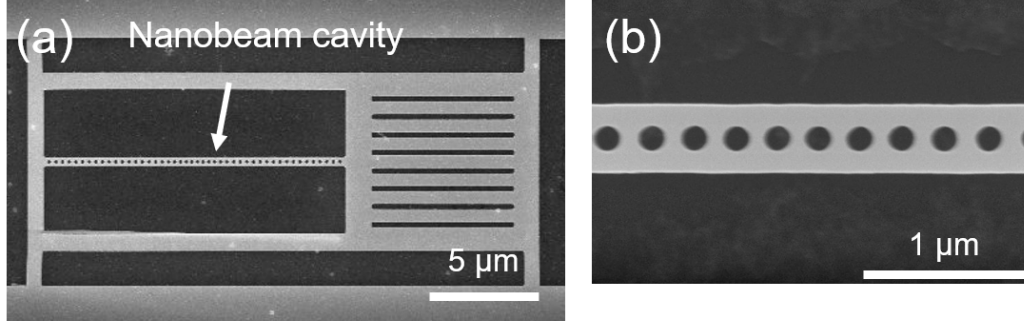


Figure 5.3: SEM image of a fabricated nanobeam cavity in this study.

Table 5.1: Utilized parameters for dry-etching SiO₂ clad.

CF ₄	Ar	Pressure	Bias	ICP	Etching time
5.0 sccm	6.0 sccm	0.75 Pa	500 W	125 W	min

port to an objective lens ($\text{NA} = 0.65$) is calculated to be about 10%.

Before placing QD SPSs on the silicon chip, the control of the glass thickness above the silicon waveguides is indispensable for the efficient QD-waveguide coupling. For this purpose, we dry-etched the glass layer above the silicon waveguide ($= d$). The dry etching was performed by inductively coupled plasma ion etching using CF₄ and Ar gases. We used the etching machine (Samco international, RIE-200iP), which is shown in Fig. 5.5. Table 5.1 summaries utilized parameters for this work. We tuned d to 350 nm, which resulted in the simulated cavity quality factors of 970 and $\eta\beta$ of 99.1%. This thickness was chosen to realize the high coupling efficiency of QD radiation into the waveguide even under the presence of fabrication imperfection. For evaluating the clad thickness, we used a thickness meter using optical interference. We also evaluated the flatness of the clad surface above the waveguide by using an AFM. Figure 5.4(b) shows the AFM image of the sample surface, demonstrating that the glass clad's top surface after the dry etching has a low r.m.s roughness of 2.2 nm, being flat enough for transfer-printing QD SPSs.

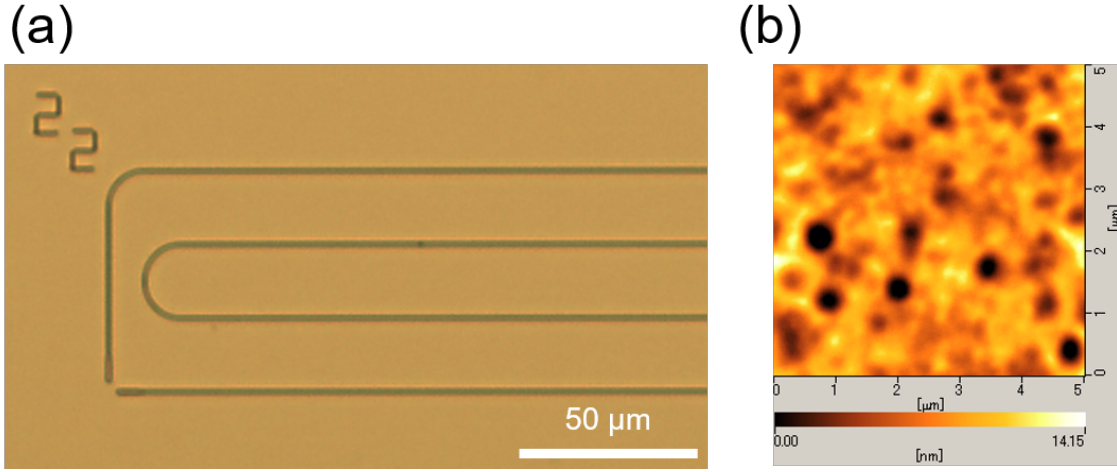


Figure 5.4: (a) Microscope image of a silicon waveguide processed by CMOS foundry. (b) AFM image of the top surface of the silicon chip after the dry etching.

5.3.3 Integration of QD SPS on CMOS-processed silicon waveguide using transfer printing

After the preparation of QD SPSs and silicon waveguides, we utilized transfer printing to place a fabricated QD SPS onto a silicon waveguide. In this study, we utilized the same transfer printing apparatus of chapter 4. We picked up a prepared QD SPS by placing a PDMS rubber stamp on it and quickly peeling the rubber stamp off as shown in Fig. 5.2(c). Then we placed the picked-up QD SPS precisely on the silicon waveguide. Subsequently, we slowly peeled off the rubber stamp, leaving only the QD SPS on the waveguide as shown in Figs. 5.2(d) and (e). The QD SPS was firmly bonded on the silicon chip through van der Waals force. Thus transfer-printing approach allows the integration of QD SPSs into photonic waveguides processed through a CMOS-process foundry, not just into those fabricated in house as demonstrated in chapter 4.

Figure 5.6 shows a microscope image of a completed device. Precise alignment between the top nanobeam cavity and the underlying waveguide can be seen. The position deviation between the nanobeam and waveguide is deduced to be ± 50 nm, which is routinely possible with our transfer-printing system. We emphasize that the hybrid integration process discussed here enables the assemble of each component after completing the entire CMOS process. Since the integration process requires



Figure 5.5: Photography of the ICP RIE machine used in this study (RIE-200iP).

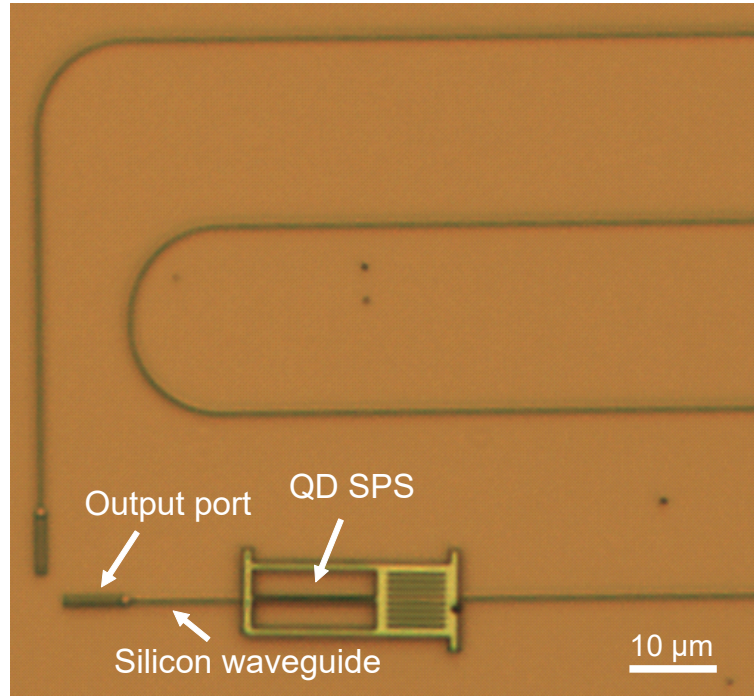


Figure 5.6: Microscope image of a completed device.

no modification of the CMOS back-end process flow, this approach is highly advantageous when exploiting the potential of silicon photonics. The transfer-printing approach is also beneficial to integrate multiple QD SPSs: we can sort out proper QD SPSs before their assembly onto a target silicon PIC.

5.4 Optical characterization of QD SPS on CMOS silicon waveguide

In this section, we experimentally investigated the fabricated device with low-temperature μ PL measurements. The setup of the optical measurement is almost the same as that of chapter 4. The collected PL was analyzed with a grating spectrometer equipped with an InGaAs camera (PIoNIR:640, Princeton instruments). For the photon detector, we used a superconducting nanowire single-photon detector (SNSPD, SCONTEL Corp.).

5.4.1 PL image

We conducted PL imaging of the fabricated device by pumping a CW Ti:sapphire laser (above-band excitation, oscillation wavelength = 820 nm, excitation power = 13 μ W) onto the center of the nanobeam cavity. Here, we inserted a long pass filter (cut-on wavelength = 900 nm) in front of an imaging camera to filter out the excitation laser. Figure 5.7(b) shows the PL image of the device at 5 K (Fig 5.7(a): microscope image of the fabricated device). We observed bright optical signals from both of the exit ports [the dotted red circles in Fig. 5.7(b)], suggesting the efficient cavity-to-waveguide coupling.

5.4.2 PL spectra from exit port and above cavity

Then, we measured PL spectra from one of the exit ports (red) and above the cavity center (blue) at 5 K, as shown in Figs. 5.8. In Fig.5.8(a), we observed strong peaks of the cavity mode emission (1,155 nm) and cavity-coupled QD emission (1,153.3 nm). We labeled this QD emission as QD-A. Besides, we can see no other signals except for the cavity-coupled QD emissions in the red curve. On the other hand, in Fig.5.8(b), we could not observe the cavity peak at 1,155 nm, which indicates that the leakage of QD-A emission from the cavity into free space was indeed suppressed, and the cavity-coupled QD emissions were predominantly funneled to the silicon waveguide. We consider that the largest perturbation for the cavity is provided by the waveguide, which is the main loss channel for the cavity photons and, in turn, suppresses the photon leakage into free space.

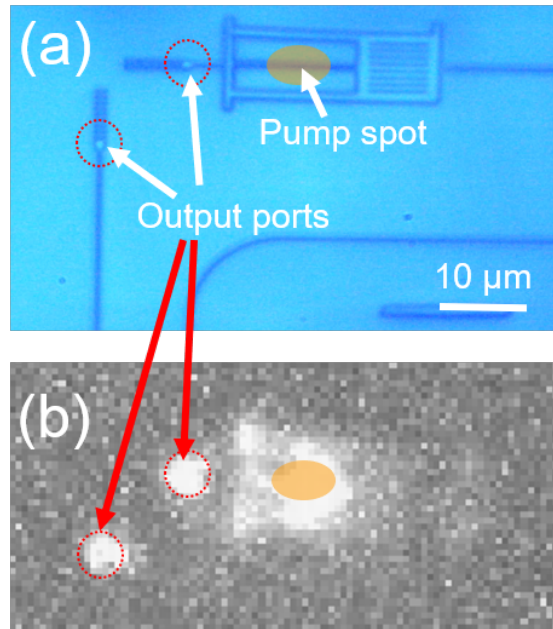


Figure 5.7: (a) Microscope image of a completed device. (b) Measured PL image by pumping a CW Ti:sapphire laser onto the center of the nanobeam cavity (oscillation wavelength = 820 nm, excitation power = 13 μW).

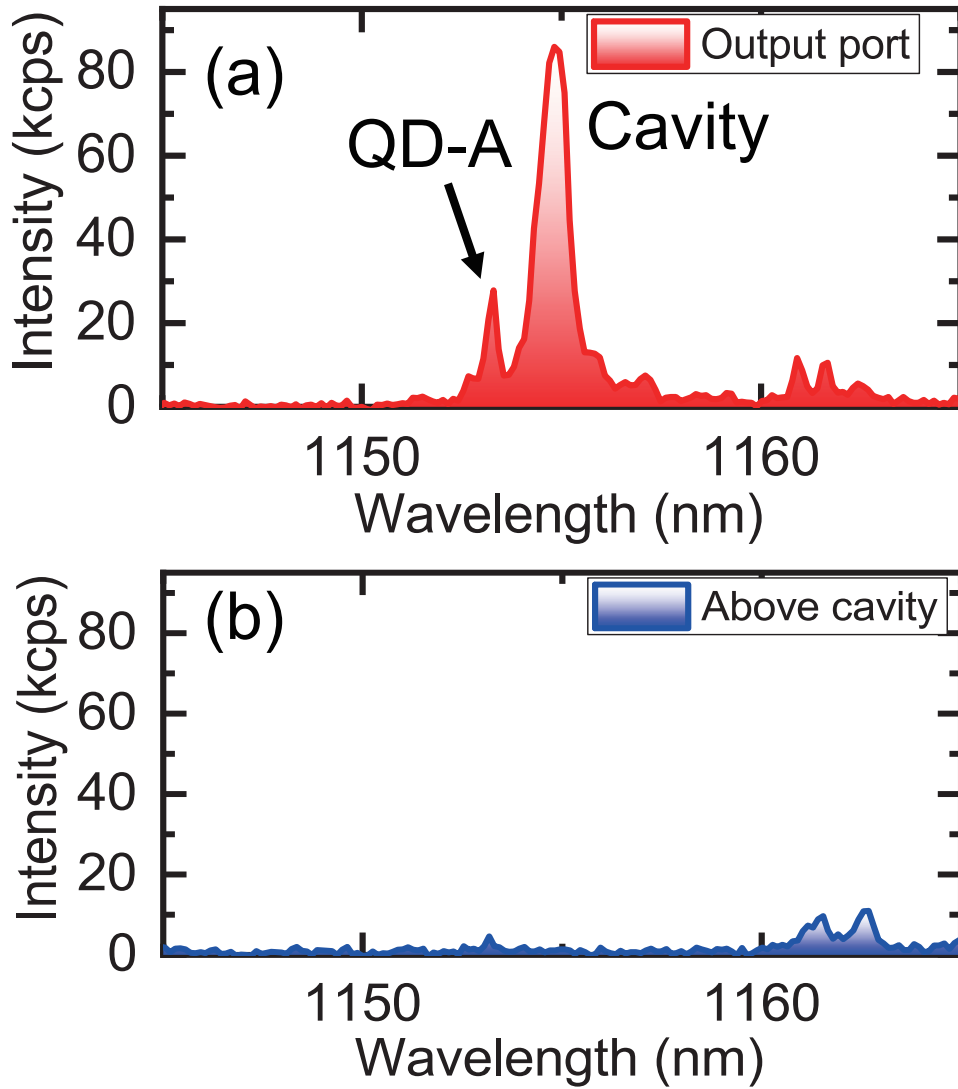


Figure 5.8: Measured PL spectra from one of (a) the exit ports and (b) above the cavity center. We used a CW Ti:sapphire laser (oscillation wavelength = 820 nm, excitation power = 13 μ W) onto the center of the nanobeam cavity.

5.4.3 Evaluation of experimental cavity-waveguide coupling efficiency (η_{exp})

We estimated an experimental cavity-to-waveguide coupling efficiency (η_{exp}) based on the measured cavity quality factors, whose details are discussed in chapter 4. From the PL spectrum in Fig. 5.8(a), we deduced the experimental quality factor of the cavity as $Q_{exp} = 1,400$. For comparison, we evaluated the quality factors of the cavities on plane glass. The average quality factor (Q_{ave}) estimated from 10 bare nanobeam cavities is estimated to be 14,000. Using the obtained Q_{exp} and Q_{ave} , we deduce an η_{exp} of 90%, elucidating the efficient coupling of the cavity mode into the silicon waveguide. Notably, we can more accurately evaluate η_{exp} when performing transmission measurements through the waveguide, which is coupled to the nanobeam cavity [93].

5.4.4 Observation of Purcell-enhanced QD emission

We further performed detailed optical characterization for the fabricated device to confirm the Purcell enhancement of the extracted QD emission. Figure 5.9(a) displays color plots of PL spectra measured through the exit port while controlling temperatures from 33 K to 52 K (pump power = 25 μ W). We observed an enhanced intensity of the QD peak around the cavity resonance of 40 K. On the other hand, the peak intensity of QD-A was decreased when QD-A was detuned from the cavity resonant mode. These results imply the increase of emitter-cavity coupling as a result of the Purcell effect.

To further confirm the Purcell enhancement for QD-A, we also performed time-resolved PL measurements for QD-A. For this purpose, we switched the pump laser to a pulsed Ti:sapphire laser oscillating at 830 nm with the averaged pump power of 180 nW, the pulse width of ~ 1 ps, and repetition rate of 80.3 MHz. We employed a time-correlated single-photon counting technique with an SNSPD (overall system time resolution of ~ 50 ps). We used the spectrometer as a bandpass filter of the PL signal. Then we focused the PL signals on the port of an optical fiber by using an x10 objective lens to send the signals to the SNSPD.

We measured the time-resolved PL spectrum for the QD-A peak at 40 K, as shown in the red curve in Fig. 5.9(b). Here, QD-A was slightly detuned by 1.5 nm from the cavity resonant mode to suppress the intrusion of the cavity background peak. Compared to the emission decay of bare QDs (black curve), a rapid emission decay of QD-A was observed. We fitted the measured curve with double exponential

decay curves convolved with a function that reflects the system time response. From the red curve in Fig. 5.9(b), the emission rate of QD-A was measured to be $\gamma_{exp} = 1.8$ GHz (decay lifetime of 500 ps). We also measured the lifetime of QD emission when thermally tuning the QD-cavity detuning, as shown in Fig. 5.9(c). The lifetime was fastened when we decreased the detuning, confirming the Purcell enhancement of QD-A.

We estimated the experimental QD-to-cavity coupling efficiency by using γ_{exp} and the obtained emission rates of QDs with no Purcell enhancement. We measured emission decay rates of several QDs in unprocessed area. The averaged decay rate was measured to be 0.9 GHz, resulting in the decay rate γ_{other} of 0.45 GHz according to the discussion in chapter 4. From these emission rates and the equation (4.4), the estimated emitter-cavity coupling efficiency from these measurements (β_{exp}) deduced to be $\sim 75\%$. Using the values of $\eta_{exp} = 90\%$ and $\beta_{exp} \sim 75\%$, the total single photon coupling efficiency is estimated to be $\eta_{exp}\beta_{exp} \sim 70\%$.

5.4.5 Observation of single-photon generation on silicon

Finally, we conducted second-order autocorrelation measurements based on a Hanbury Brown-Twiss setup. For this measurement, we added a 50/50 fiber beam-splitter (center wavelength = 1064 nm, bandwidth = ± 100 nm) and an SNSPD into the photon counting setup. Here, we utilized a CW Ti:sapphire laser (wavelength = 860 nm, excitation power = 130 μ W) for the efficient excitation of QD-A. Figure 5.10(a) shows a PL spectrum measured at one of the output ports after tuning the laser oscillating wavelength to 860 nm. We filtered the emission peak of QD-A at 1,153 nm and sent it to the interferometer. Figure 5.10(b) shows the normalized second-order autocorrelation function $g^{(2)}(t)$ measured for the QD-A peak at 5 K (QD-cavity detuning = 1.6 nm).

As a simple model for antibunching, we considered a single quantum system with two states, a ground and excited state ($|g\rangle$ and $|e\rangle$, respectively). Here, we assume that the carrier was excited ($|g\rangle \rightarrow |e\rangle$) with the rate p , and decayed ($|e\rangle \rightarrow |g\rangle$) by spontaneously emitting a photon with the rate γ . For this simple model, $g^{(2)}(t)$ can be derived by solving the following rate equations:

$$\frac{d}{dt} \begin{pmatrix} P_e(t) \\ P_g(t) \end{pmatrix} = \begin{pmatrix} -\gamma & p \\ \gamma & -p \end{pmatrix} \begin{pmatrix} P_e(t) \\ P_g(t) \end{pmatrix}, \quad (5.1)$$

where $P_g(t)$ and $P_e(t)$ are the probabilities for the carrier to be in the ground and excited states, respectively. Here we set the condition $P_g(t) + P_e(t) = 1$. For the

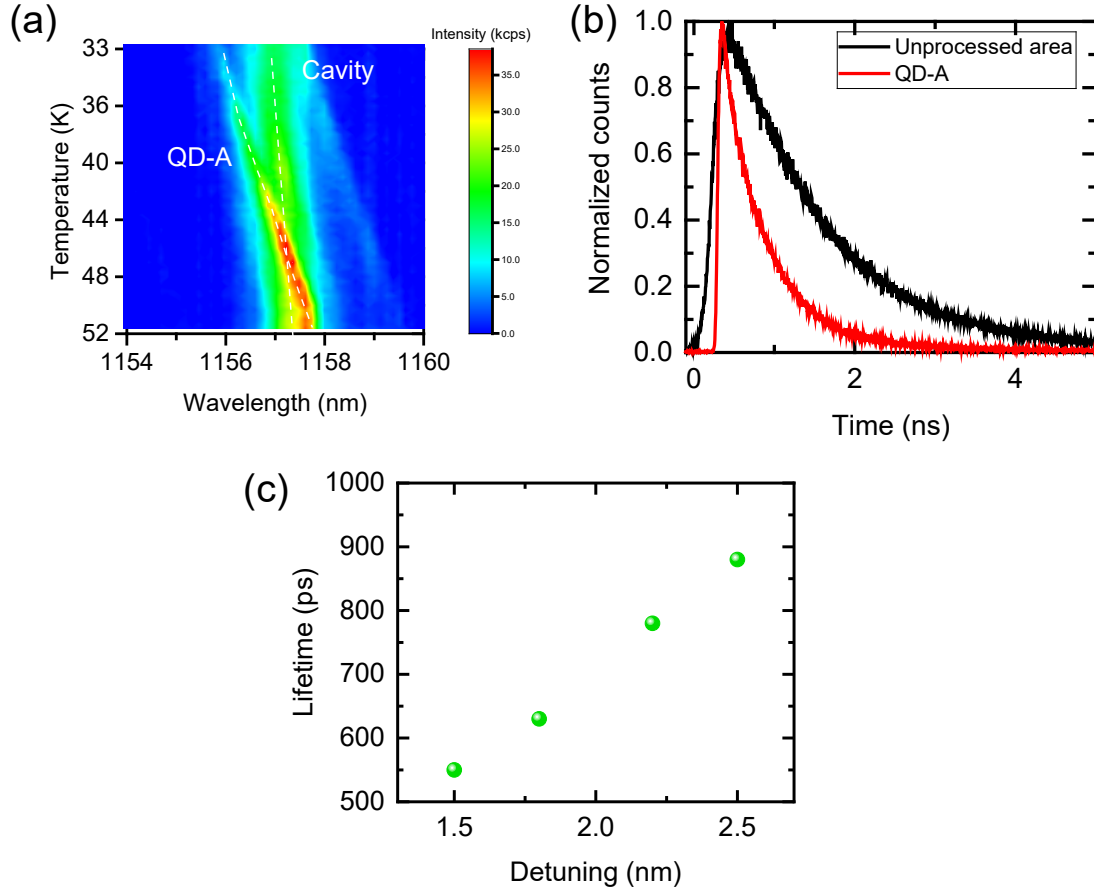


Figure 5.9: (a) Colorplot of the spectra measured by temperature tuning and through the output port. (b) Time-resolved PL spectra that are measured for the QD-A emission at 40 K when QD-A is slightly detuned from the cavity resonance by 1.5 nm (red curve). Black curve: Time-resolved PL spectrum measured for a typical ensemble QD emission inside an unprocessed area of the same wafer. (c) The measured lifetime of QD emission as a function of the QD-cavity detuning.

excited state, the probability takes the following form;

$$\frac{d^2}{dt^2}P_e(t) = -(p + \gamma)\frac{d}{dt}P_e(t) \quad (5.2)$$

If we set the initial condition as $P_g(0) = 1$ and $P_e(0) = 0$, we can obtain

$$P_e(t) = \frac{p}{p + \gamma} [1 - e^{-(p+\gamma)t}]. \quad (5.3)$$

From this equation, $g^{(2)}(t)$ for this model can be expressed as

$$g^{(2)}(t) = \frac{P_e(t)}{P_e(t = \infty)} = 1 - e^{-(p+\gamma)t}. \quad (5.4)$$

By taking into account an imperfection of anti-bunching at zero time delay ($g^{(2)}(0)$), we fitted the obtained data with the following function:

$$g^{(2)}(t) = 1 - [1 - g^{(2)}(0)] \exp(-|t|/\tau), \quad (5.5)$$

where $\tau = 1/(p + \gamma)$ is the decay time of QD-A and t is the delay time. Before this fitting, the obtained data were convolved with the time response of our detection system. The fitted curve using (5.5) was depicted by the red curve in Fig. 5.10(b). An anti-bunching with $g^{(2)}(0) = 0.30$ at $t = 0$ demonstrated single-photon generation from QD-A. The non-zero $g^{(2)}(0)$ value is probably due to the intrusion of background cavity emission supplied by other off-resonant QDs inside the cavity. To quantitatively assess this, we employed a simple expression for $g^{(2)}(0)$ value under the presence of background noise:

$$g^{(2)}(0) = 1 - \left(\frac{\alpha}{\alpha + 1} \right)^2, \quad (5.6)$$

where α is the ratio of the QD emission signal to the noise with Poissonian photon statistics [120]. We deduced α from the measured spectrum of Fig. 5.10(a), after taking into account the spectral bandwidth sent to the single-photon counters. The deduced α is 6.0, which results in a $g^{(2)}(0)$ value of 0.27 according to the equation (5.6). The estimated value coincides well with that measured (0.30) by the intensity autocorrelation measurements. Therefore, we conclude that the degradation of $g^{(2)}(0)$ mainly stems from the contamination by the cavity-related background emission. For the generation of purer single photons, it would be necessary to employ a wafer with a much lower QD density, though the use of deterministic integration approaches [71, 121] might be required to efficiently couple the low-density QDs to nanocavities.

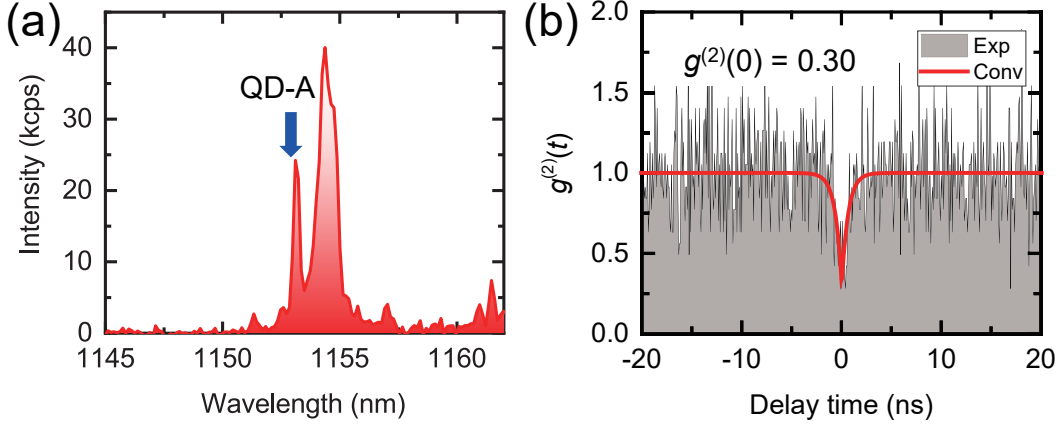


Figure 5.10: (a) PL spectrum measured at one of the output ports when the cavity center is pumped using a CW laser at 860 nm. (b) Normalized second-order autocorrelation function $g^{(2)}(t)$ measured for QD-A.

5.5 Summary

In this chapter, hybrid integration of a QD SPS on a silicon PIC processed by a CMOS foundry was studied. Since the integration of photonic devices is based on van der Waals adhesion, transfer printing enables us to assemble QD SPSs after the completion of the entire CMOS process. To unveil a method to integrate QD SPSs on a silicon CMOS chip, QD SPSs were transfer-printed onto a dry-etched glass surface of a CMOS chip. It was confirmed that integrated QDs were cooled down even on a foundry-processed silicon chip. Intensity autocorrelation measurement also verified single-photon generation from an integrated QD on silicon with $g^{(2)}(0) = 0.30$. Its efficient waveguiding in the CMOS-processed photonic chip with the coupling efficiency of $\sim 70\%$ was also confirmed in experiment. Transfer-printing-based approach will potentially enable the scalable implementation of QD SPSs into a highly-functional silicon CMOS chip.

Chapter 6

In-situ spectral tuning of QD single-photon source on silicon CMOS chip

6.1 Introduction

For many practical quantum applications, on-chip integration of identical SPSs is one of the crucial issues for performing on-chip two-photon interference. For this purpose, encouraging progress has been made in the hybrid integration of QD-based SPSs onto silicon-based photonic platforms [67, 69, 70, 72] as we discussed in chapter 5. However, there remains a challenge in implementing desired QD SPSs on preferred locations on chip, which is hindered by position and spectral randomness inherent in QDs. Some deterministic integration approaches of QDs might be a solution to this issue [43, 71, 121, 122], though their compatibility with advanced PIC technologies (e.g., CMOS foundry processes) has not been intensively studied yet.

To overcome the challenge of this randomness, we have been investigating a new hybrid integration approach based on transfer printing. By pre-characterizing SPSs before the transfer printing process, this approach may enable us to integrate QD SPSs with desired optical properties on arbitrary locations of a CMOS silicon chip at will. Nevertheless, perfect spectral matching among integrated SPSs is still necessary for the scalable operation of dominant quantum photonic information processing protocols that rely on quantum interference among photons. For controlling emission wavelengths of QD SPSs, several methods have been studied including thermal tuning [123, 124], strain tuning [125, 126], magnetic tuning [127] and Stark tuning [128–130]. We note that two-photon interference between two QD

SPSs has recently been demonstrated on a single GaAs chip [58]. The demonstration of two-photon interference between two independent QD SPSs has recently also been shown at telecommunication wavelength by using quantum frequency conversion [131]. However, the interference was performed not on chip but off chip, and the QD SPSs were not integrated into an optical circuit.

In this chapter, we demonstrated in-situ fine wavelength tuning of QD SPSs integrated on a CMOS-processed silicon waveguide. We thermally controlled the emission wavelengths of the integrated QDs by using heater pads that could absorb the heating laser irradiated from the above [58, 123, 124]. We additionally integrated the heater pads onto the silicon-integrated QD SPS. All the hybrid integration processes were conducted using transfer printing, which largely facilitated the 3D stack of the photonic micro/nanostructures. With this approach, we also demonstrated spectral matching between two dissimilar QD sources integrated on a silicon CMOS chip.

6.2 Device structure for on-chip spectral tuning of QD SPS

In this section, we describe the device structure for on-chip spectral tuning of on-silicon QD SPSs. Figure 6.1 illustrates the schematic structure of the investigated device. A QD SPS is placed above a glass-cladded silicon waveguide. A high-Q nanobeam cavity based on a GaAs-based 1D PhC is utilized to support the efficient coupling of the QD emission into the silicon waveguide. To thermally tune the wavelength of the QD emission, a metal pad based on Cr is implemented on the integrated SPS's marginal region. This pad can function as a heater when irradiated with an external heating laser beam, allowing for in-situ fine tuning of the wavelength of the QD emission on chip. The employed device structure was designed to achieve near-unity single-photon coupling of the QD into the silicon waveguide by tuning the vertical cavity-waveguide distance, d (see also the cross-section of the device shown in Fig. 6.1). For $d = 360$ nm, the device supports a calculated emitter-waveguide coupling efficiency of $\eta\beta = 99.3\%$. The detailed numerical calculations of waveguide coupling efficiencies are discussed in chapters 3 and 5.

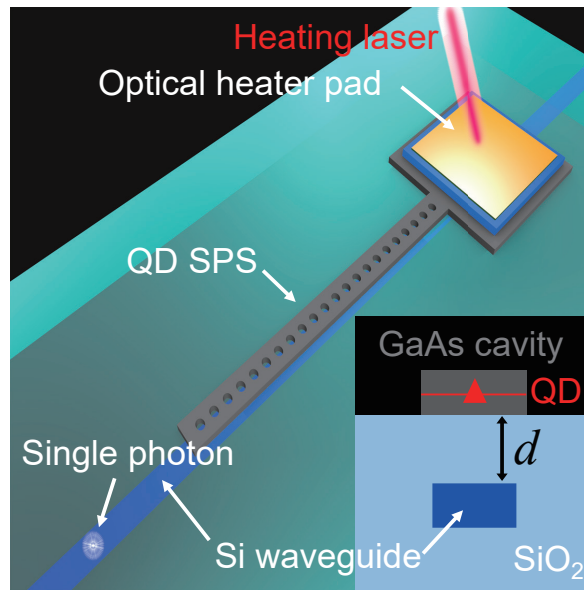


Figure 6.1: Schematic of the investigated device structure. A QD SPS is placed on a glass-cladded silicon waveguide. An optical heater pad is augmented on the marginal region of the integrated SPS (Inset: Schematic of the device cross-section).

6.3 Fabrication of investigated device structure

In this section, we describe the detailed procedure of fabricating the device based on transfer printing. Figures 6.2 show the procedure of fabricating the device based on transfer printing. Based on our transfer printing approach, not only QD SPSs but also optical heater pads can be integrated on a silicon CMOS chip.

6.3.1 Preparation of waveguide-integrated QD SPS

First, we integrated an InAs/GaAs QD SPS onto a silicon waveguide [Figs. 6.2(a) and (b)]. For this purpose, we fabricated 1D PhC-based QD SPSs into a 180 nm-thick GaAs slab embedding one layer of self-assembled InAs QDs. The parameters of the PhC cavities and areal density of QDs were the same as those discussed in the previous chapter. We also employed glass-cladded silicon waveguides processed by a CMOS foundry, the same chip as chapter 5. We reduced the thickness of the SiO₂ clad layer above the silicon waveguide using a dry etching process for efficient single-photon waveguiding. The measured clad thickness above the waveguide was $d = 360$ nm.

We integrated the QD SPS onto the silicon waveguide by utilizing transfer printing. We picked a prepared QD SPS by attaching a PDMS rubber stamp on it and then by rapidly peeling the stamp off [Fig. 6.2(c)]. The picked-up QD SPS was subsequently transferred to the silicon CMOS chip by placing the SPS on the top of the silicon waveguide and slowly releasing the transparent rubber stamp [Fig. 6.2(d)].

6.3.2 Integration of laser-driven heater pad using transfer printing

Next, we implemented an laser-driven heater pad onto the integrated QD SPS. We prepared plates (width = $7.8 \mu\text{m}$, length = $24 \mu\text{m}$) into a 220 nm-thick silicon slab using the standard semiconductor nanofabrication processes [Fig. 6.2(e)]. We performed the dry etching of silicon by inductively coupled plasma ion etching using SF₆ and O₂ gases. We used the etching machine (Samco international, RIE-140Ai), which is shown in Fig. 6.3. Table 6.1 summaries utilized parameters for this work. Then we evaporated 20 nm-thick Cr on the silicon plates, which absorbs heating laser efficiently [Fig. 6.2(f)]. We performed wet etching to form the air-bridge structure of the evaporated plates. For the wet etching of SiO₂, we dipped the sample in HF for 10 minutes at room temperature. The details of HF are shown in chapter 4. Figure

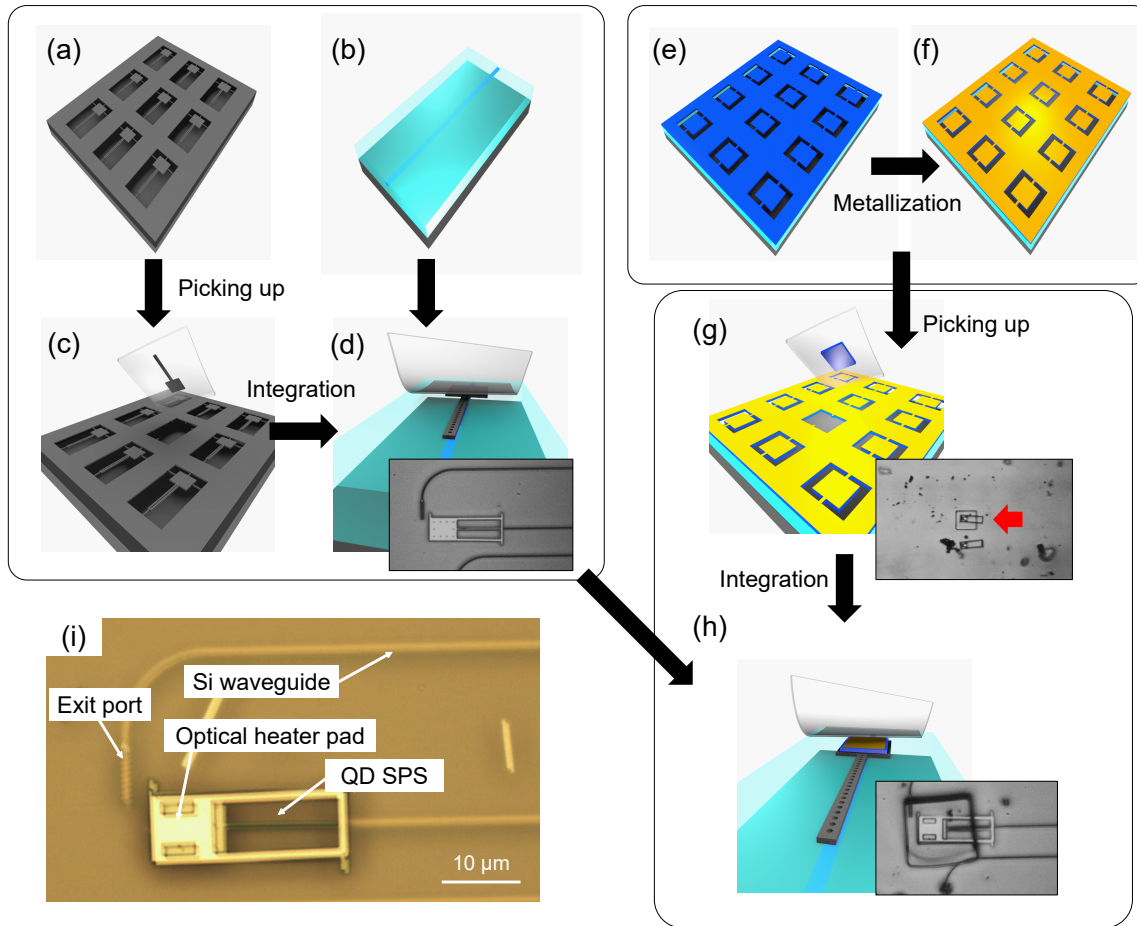


Figure 6.2: Procedure of fabricating the device based on transfer printing. We began with the preparation of (a) InAs/GaAs QD-based SPSs and (b) glass-cladded silicon CMOS waveguides. (c) We picked up one of QD SPSs by placing a PDMS rubber stamp on it and quickly peeling off the rubber stamp. (d) The picked-up QD SPS was then accurately transferred to the top of the silicon waveguide by placing the SPS and slowly peeling off the transparent rubber stamp. In parallel, we prepared (e) silicon plates to fabricate (f) optical heater pads by evaporating 20-nm-thick Cr on the silicon plates. (g) and (h) The heater pad was then transferred onto the marginal region of the integrated SPS by repeating the transfer printing process. (i) Microscope image of a completed device. (Insets: Microscope images obtained at each step of the process.)



Figure 6.3: Photography of the ICP RIE machine used in this study (RIE-140AI).

6.4 shows the microscope image of air-bridge optical heater pads. We note that the separate fabrication of the heaters and SPSs allows us to maintain optical properties of the QD SPSs as the direct evaporation of Cr onto the QD SPS structure may degrade the quality of the QDs.

Table 6.1: Utilized parameters for dry-etching Si slab.

SF ₆	O ₂	Pressure	Bias	Etching time
4.5 sccm	6.0 sccm	0.3 Pa	20 W	3 min

Finally, we transferred the heater pad onto the marginal region of the integrated SPS by repeating the pick-and-place transfer printing process [Figs. 6.2(g) and (h)]. The insets in Fig. 6.2 show microscope images taken at each step of the process, and Fig. 6.2(i) shows a microscope image of a completed device. We emphasize that the simple pick-and-place operation of transfer printing largely facilitates constructing the complicated 3D stack of micro/nanostructures.

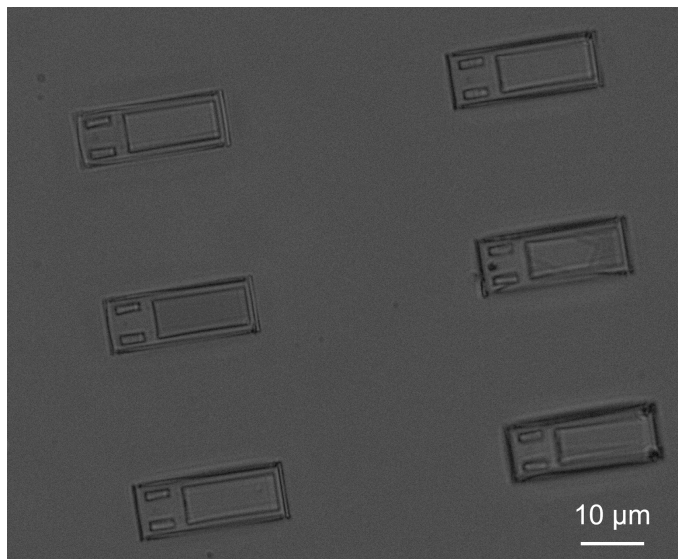


Figure 6.4: Microscope image of air-bridged optical heater pads.

6.4 Optical characterization of the fabricated device

6.4.1 Optical measurement setup

To characterize fabricated devices, we conducted low-temperature μ PL measurements. Figure 6.5 shows a schematic overview of the constructed low temperature μ PL measurement setup utilized in this study. For the optical pumping of the QDs, we used the following laser sources: CW diode laser oscillating at 785 nm (Pigtailed laser diode, Thorlab), pulsed diode laser (PDL 800-B, PicoQuant) and CW Ti:sapphire laser (3900S, Spectra physics). To guide the laser light to the sample, we used a 92/8 pellicle beam splitter. To image the samples, focus a pump laser beam on samples and collect PL signals, we utilized an objective lens with N.A. = 0.65, working distance of 4.5 mm and cover glass correction up to 1.2 mm (LCPLN50XIR, Olympus Corp.). The collected PL was then sent to a grating spectrometer (Acton SP2750, Princeton Instruments) equipped with an InGaAs CCD camera (PIoNIR:640, Princeton instruments). The spectrometer has three gratings with groove densities of 300 mm^{-1} and 900 mm^{-1} and 1350 mm^{-1} , which can be switched by rotating the turret by a motor.

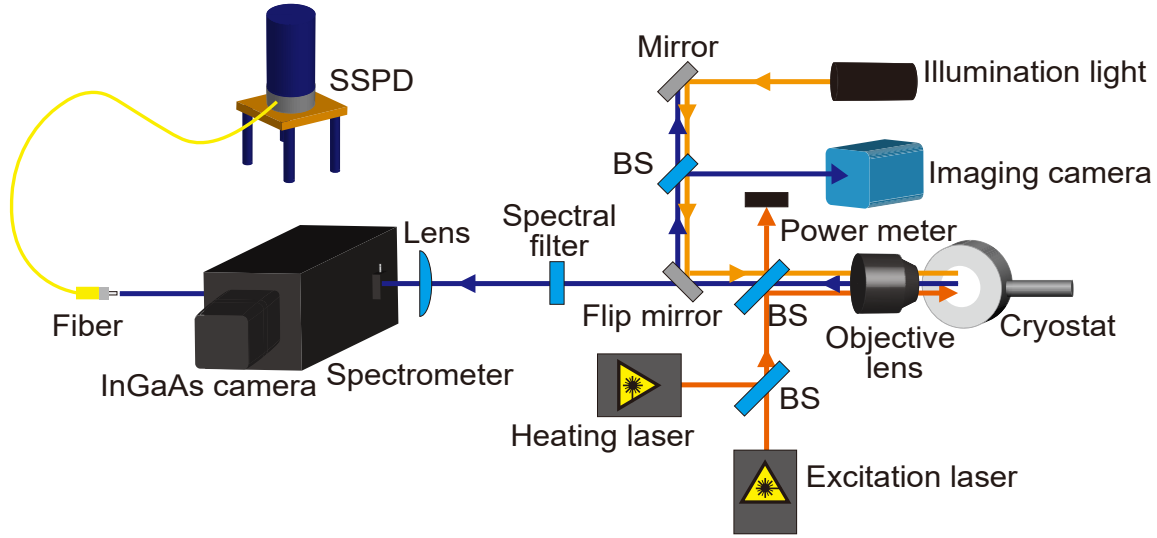


Figure 6.5: Schematic overview of the constructed low temperature μ PL measurement setup utilized in this study.

6.4.2 Tunability of integrated QD SPS

We measured a PL spectrum from the output port when pumping the cavity center using a continuous-wave diode laser oscillating at 785 nm (average pump power of 1 μ W). Figure 6.6(a) displays the obtained PL spectrum at 21 K. We observed a strong peak of cavity resonant mode emission (1161.9 nm) and QD emission (1162.9 nm).

We estimated an experimental cavity-waveguide coupling efficiency (η_{exp}) based on the measured cavity quality factors (see the detailed discussions in chapter 4). From the PL spectrum in Fig. 6.6(a), we deduced the experimental quality factor of the cavity as $Q_{exp} = 2,500$. For comparison, we evaluated the quality factors of the cavities on the plane glass. The average quality factor (Q_{ave}) estimated from 10 bare nanobeam cavities is estimated to be 12,500. Given these values, we deduce an η_{exp} of 80%, demonstrating efficient waveguide coupling of the cavity mode and was comparable to our previous results shown in chapter 5.

Next, we tested the spectral tunability of the fabricated device. For optically heating the sample, we used a continuous-wave Ti:sapphire laser oscillating at 920 nm, which was combined with the pump laser by a 55/45 beam splitter. This wavelength was chosen to suppress the excitation of the QDs by this heating laser. We activated the metal heater pad by irradiating a heating laser. Figure 6.6(b) displays

PL spectra measured from the exit port while increasing the heating laser power. When increasing the power of the heating laser, QD emission was indeed red-shifted. Simultaneously, QD emission linewidth was broadened from 0.15 nm to 0.2 nm. Since the QDs employed in this work has broad linewidths due to strong spectral diffusion, it is difficult to discuss the temperature dependence of QD emission linewidth in detail.

The dependence of the QD detuning on the heating laser power is shown in Fig. 6.6(c). The right y axis in Fig. 6.6(c) expresses the effective temperature of the sample during thermal tuning, which was estimated from experiments with a global heater equipped with the cryostat. The maximum possible tuning range of QD emission wavelength in this study was 0.9 nm. The obtained tuning range is half compared to the previous demonstration for an air-bridge PhC nanocavity [123]. We consider that this narrower tuning range was probably due to the heat dissipation from the GaAs layer into the underneath glass clad. We presume that heat transfer from the transfer-printed heater pad to the GaAs layer is efficient as reported in previous work [97].

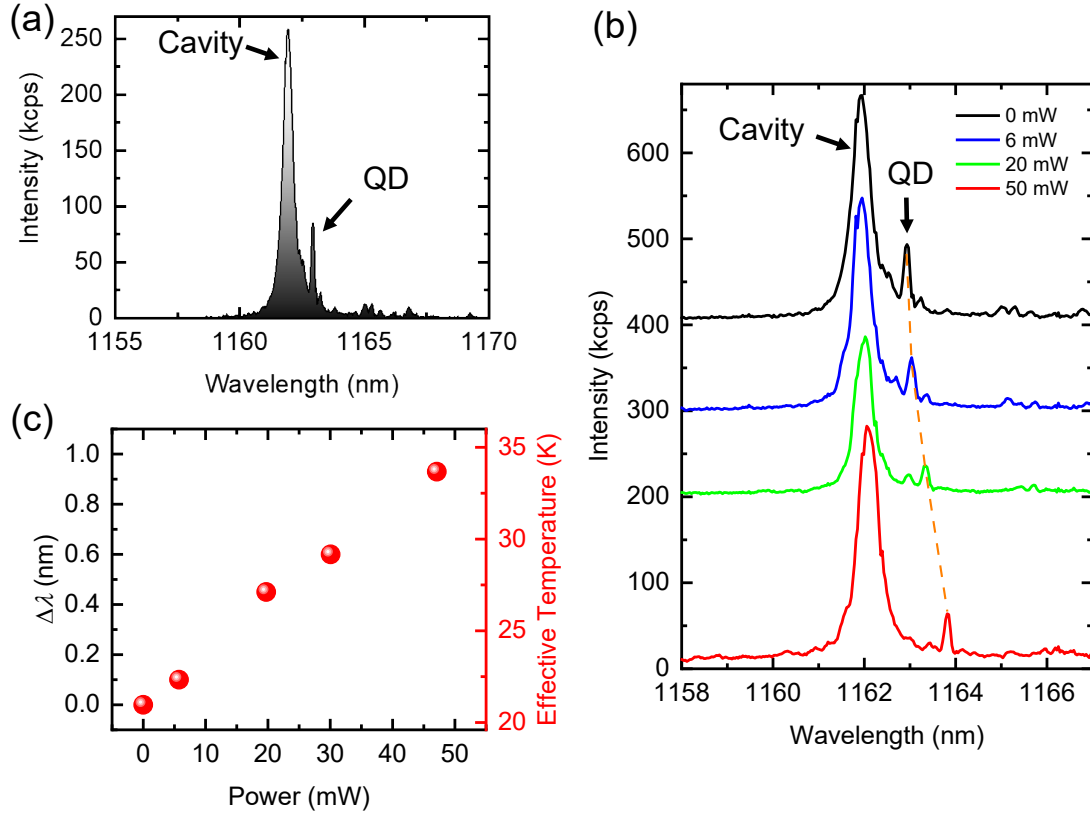


Figure 6.6: (a) PL spectrum measured from the exit port at 21 K. (b) PL spectra measured from the exit port while changing the heating laser power. (c) Dependence of the QD detuning on the heating laser power.

6.4.3 Single-photon generation under heat tuning

To show the compatibility of our local tuning technique with the single-photon generation, we performed an intensity autocorrelation measurement based on a Hanbury Brown-Twiss setup equipped with two superconducting nanowire single-photon detectors (overall system time resolution of ~ 50 ps). We measured a normalized second-order autocorrelation function $g^{(2)}(t)$ for the QD peak under heating with a heating laser power of 6 mW (the PL spectrum is displayed in Fig. 6.7(a)). Figure 6.7(b) shows a normalized $g^{(2)}(t)$ measured with a reduced pump power of 200 nW. We fitted the obtained data with the (5.5), as described in chapter 5. An anti-bunching with $g^{(2)}(0) = 0.34$ at the zero delay time was observed, confirming single-photon generation from QD even under the local tuning. We consider that the non-zero $g^{(2)}(0)$ value was probably due to the background cavity intrusion stemming from other off-resonant QDs inside the cavity.

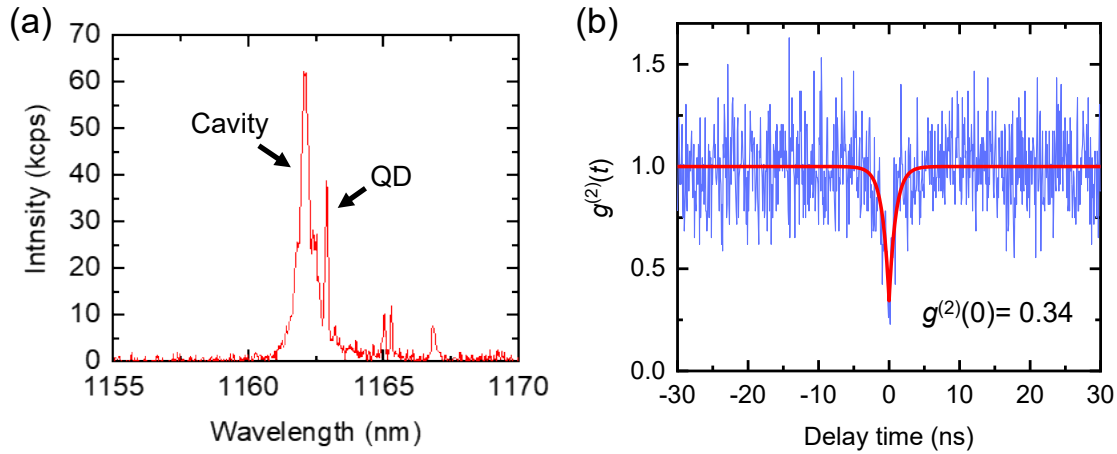


Figure 6.7: (a) PL spectrum measured from the exit port at 21 K with a reduced pump power of 200 nW. (b) Normalized $g^{(2)}(t)$ measured with a reduced pump power of 200 nW.

6.4.4 Stability of the fabricated device

We showed that our thermal tuning is stable during the experiment. Figure 6.8 shows a time trace of QD emission peak with and without optical heating. Emission wavelengths of the QD during the optical heating look very stable under this level of energy resolution.

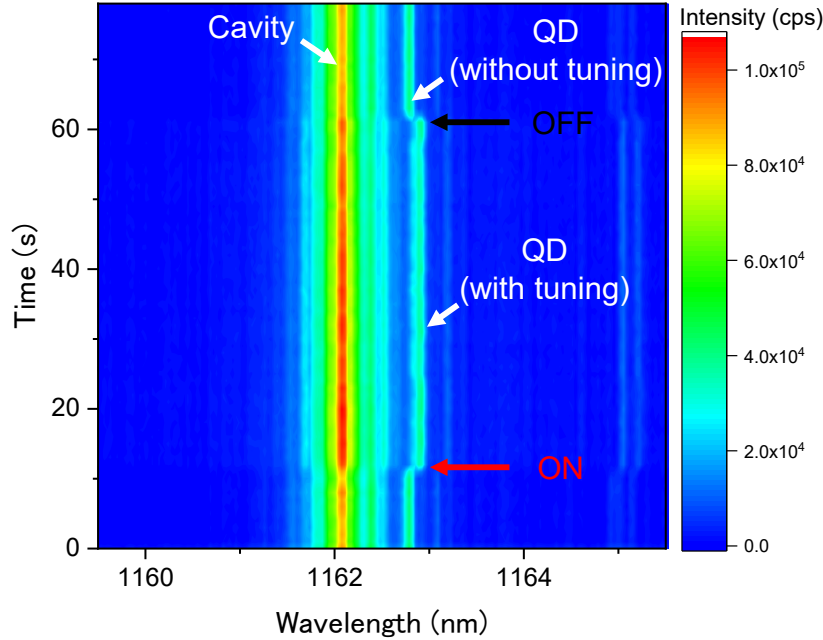


Figure 6.8: Time trace of QD emission wavelength with and without optical heating.

6.5 Spectral matching between dissimilar integrated two QD sources

Finally, we exploited our tuning method for the spectral matching between dissimilar integrated QD sources, which is essential for future demonstration of Hong-Ou-Mandel interference on chip. For this purpose, we first integrated two QD sources onto a single silicon CMOS chip using transfer printing. Then we augmented laser-driven heater pads onto these QD sources by repeating the transfer printing process shown in Fig. 6.2. These waveguides are connected at a 50/50 beam splitter based

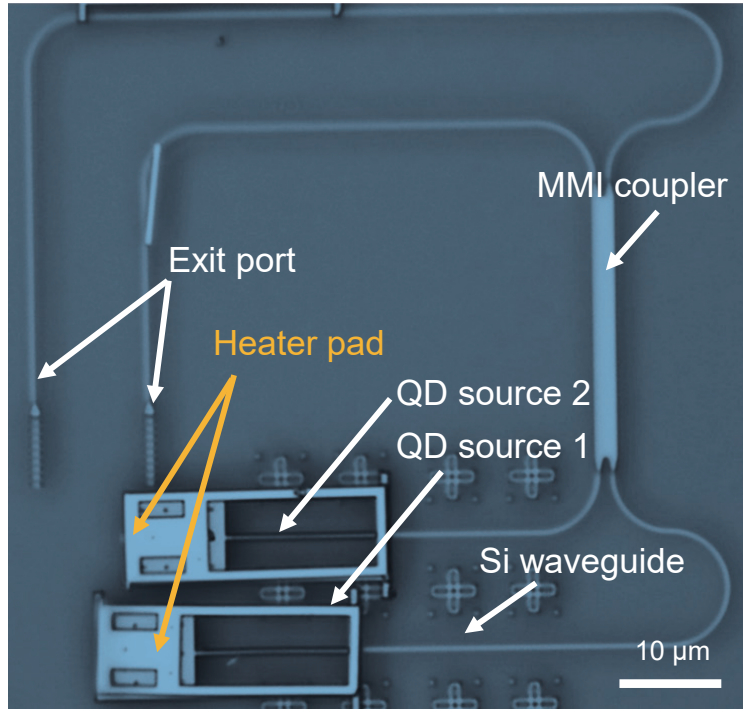


Figure 6.9: Microscope image of the completed device. We first integrated two QD sources onto a single silicon CMOS chip using transfer printing. Then we augmented laser-driven heater pads onto these QD sources by repeating the transfer printing process shown in Fig. 6.2. These waveguides are connected at a 50/50 beam splitter based on a 2×2 MMI coupler, which functions as a 50/50 optical beam splitter.

on a 2×2 multimode interferometer waveguide (MMI) coupler¹, which functions as a 50/50 optical beam splitter. We designed the 50/50 MMI coupler based on [133]. Figure 6.9 displays a microscope image of the completed device.

We characterized the optical property of the two integrated QD sources using μ PL measurements through the exit port. We can observe strong QD emission peaks for both QD sources as shown in Figs. 6.10(a) and (b) (which we labeled as QD1 and QD2, respectively).

We simultaneously pumped both QD1 and QD2 while tuning QD2 with respect to QD1 using the heater pad for QD2. For this particular measurement, we split the

¹An $N \times M$ MMI coupler consists of a multimode waveguide, N input channels and M output channels. MMI couplers are based on the self-imaging principle, by which an input field profile is reproduced in single or multiple images at periodic intervals along the light propagation direction of the waveguide [132].

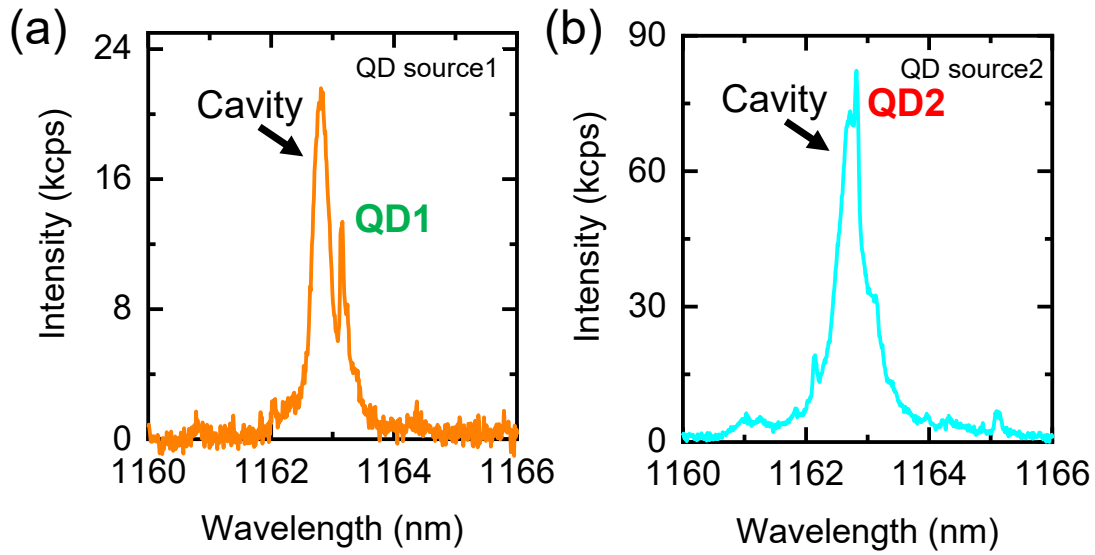


Figure 6.10: (a) and (b) PL spectra measured for QD source 1 and 2 through one of the exit port.

pump laser beam into two paths and then combined by beam splitters, as shown in Fig. 6.11.

Figure 6.12(a) shows PL spectra collected at the exit port where both the signals from QD1 and QD2 exited at the same time. The emission from QD2 exhibited redshifts as the heating laser power was increased. At the heating power of 28 mW, we observed matching of the peaks between QD1 and QD2. Figure 6.12(b) summarizes the peak wavelengths of QD1 and QD2 as a function of heating laser power, confirming the wavelength matching between the integrated two QD sources. This result suggests that we can perform mutual tuning of QD sources in proximity by using the current spectral tuning structure. We note that the slight red-shift of QD1 was probably because of the insufficient thermal separation of QD source 1 from QD source 2, which can be solved by thermal insulation with a trench between the integrated sources.

We note that the thermal tuning technique employed in this work could have the possibility of diminishing photon indistinguishability due to the phonon-induced dephasing [134,135]. Meanwhile, our nanocavity-based device structure can support large Purcell enhancement of the QD radiation, enabling us to overcome the dephas-

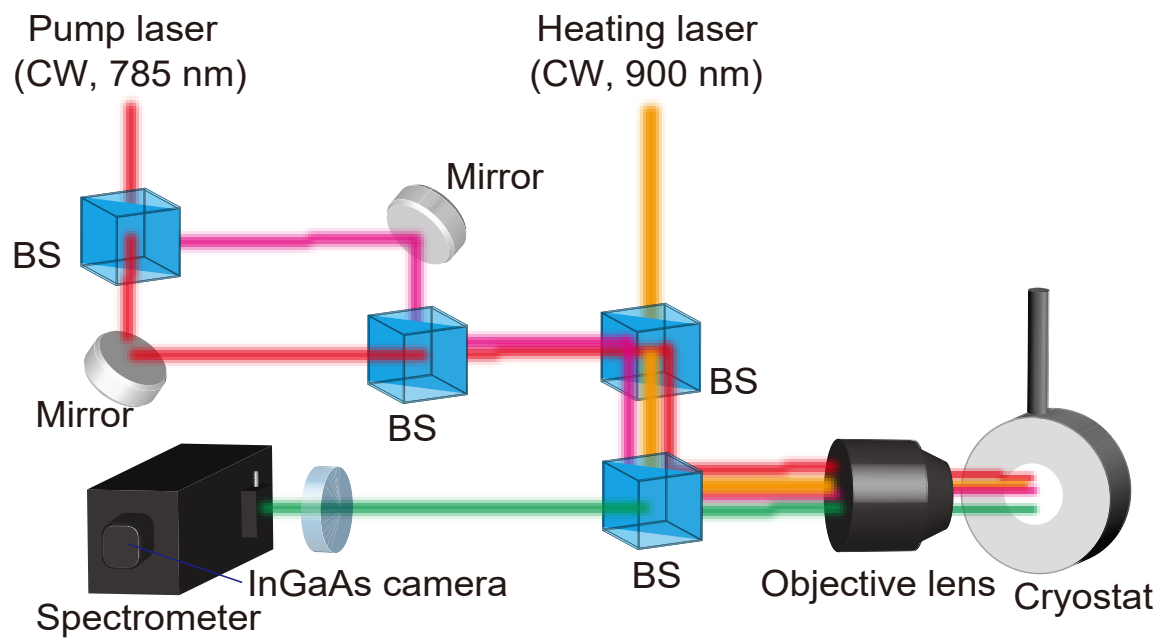


Figure 6.11: Schematics of the μ PL measurement setup for simultaneously pumping both QD1 and QD2 while thermally tuning QD2 with respect to QD1.

ing issue and retrieve high indistinguishability even at elevated temperatures [42,136]. The total dephasing rate of an optical transition is given by

$$\frac{1}{T_2} = \frac{1}{2T_1} + \frac{1}{T_2^*}, \quad (6.1)$$

where $1/T_1 = \Gamma$ is the population decay rate (due to radiative or non-radiative processes) and $1/T_2^* = \gamma^*$ is the pure dephasing rate induced by the solid-state environment (phonons, charge noise, and so on). Photon indistinguishability of cavity-coupled QDs (I) can be theoretically approximated by the following equation;

$$I = \frac{\Gamma_{tot}}{\Gamma_{tot} + \gamma^*} \quad (6.2)$$

where $\Gamma_{tot} = F_p \Gamma$ (F_p : Purcell factor). According to [135], we can assume $\gamma^* = 2$ GHz at the sample temperature of 35 K. When assuming a high Purcell factor of $F_p = 10$ and a standard value for Γ of 1 GHz, the expected indistinguishability is calculated to be $I = 0.71$. If we can obtain the improved Purcell factor (e.g., $F_p = 100$), it would be possible to achieve photon indistinguishability of $I = 0.96$. We can see that high indistinguishability can indeed be recovered thanks to the Purcell enhancement even when the temperature is raised for wavelength tuning. Unfortunately, however, since the QD under concern exhibits a strong linewidth broadening, it is not easy to correctly evaluate its linewidth.

We also consider that other tuning techniques based on electric and strain fields could be powerful alternatives of the presented heat tuning technique, which may hamper the stable operation of future large-scale quantum PICs at low temperature. Among the various approaches, DC Stark tuning could be attractive in terms of the photon indistinguishability since it allows for tuning QDs simply by applying voltage via electrodes. We consider the introduction of required electrodes into the QD SPSs would also be possible by using transfer printing [137,138].

6.6 Summary

In this chapter, in-situ fine wavelength tuning of QD SPSs on a CMOS-processed silicon PIC was demonstrated. Laser-driven heater pads were utilized to tune the emission wavelengths of integrated QDs thermally. Transfer printing enables us to integrate these functional components as well as QD SPSs in a simple pick-and-place manner. The obtained maximum possible tuning range of QD emission wavelength

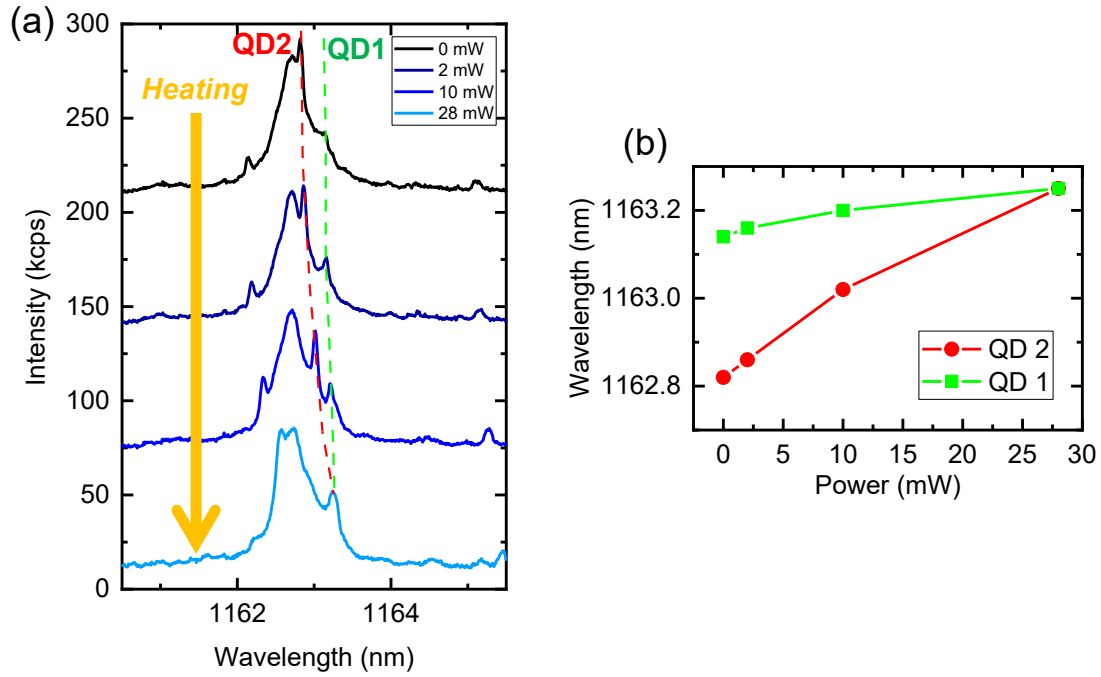


Figure 6.12: (a) PL spectra measured while pumping both QD sources and irradiating the heating laser to the optical heater pad for QD2. The dotted green (red) line shows the peak positions of QD1 (QD2). (b) Summarized emission wavelengths of QD1 and QD2 as a function of the heating laser power.

was 0.9 nm. Furthermore, this approach was leveraged for the spectral matching of two dissimilar integrated QD sources on the same silicon CMOS chip, which is an important step toward on-silicon two-photon interference with dissimilar QD-based SPSs.

Chapter 7

Efficient QD single-photon source transfer-printed on silicon photonic waveguide with unidirectional output

本章については5年以内に雑誌等で刊行予定のため、非公開。

Chapter 8

Fiber-pigtailed QD single-photon source integrated on silicon CMOS chip

8.1 Introduction

Future practical quantum photonic information processing requires efficient fiber coupling of single photons with plug-and-play operation toward the long-distance and secure quantum network. To this end, the development of fiber-pigtailed QD SPSs is a very promising approach, enabling the efficient and stable supply of single photons for quantum applications.

Several previous studies have reported the fiber-coupled QD SPSs based on direct coupling [139–142], evanescent coupling [143, 144] and hybrid integration [145]. However, the challenge of these approaches is the low single-photon coupling efficiencies into optical fibers. Also, none of them have demonstrated fiber coupling of QD SPSs that were integrated on PICs. The development of fiber-pigtailed QD SPSs on hybrid PIC platforms is of great importance to leverage the power of advanced and matured PIC technologies. In particular, silicon photonics can offer well-developed fiber-to-chip couplers: by using lateral couplers based on spot-size converters (SSCs), <1 dB coupling loss has been reported when using lensed fibers [146, 147].

In this chapter, we demonstrated fiber-pigtailed QD SPSs hybrid integrated on a silicon CMOS chip. We succeeded in observing QD emission through the optical fiber and observed the single-photon generation in the fabricated device. This chapter also shows the details of nanofabrication technology to fabricate InP PhC cavities, which is essential for efficient and telecom QD SPSs.

8.2 Device structure for efficient InP based QD SPS on silicon

In this section, we describe the device structure of fiber-pigtailed QD SPSs on a silicon CMOS chip. Figure 8.1 shows a schematic of the investigated device structure. A QD-based SPS is placed on a glass-cladded silicon waveguide. In this work, SPSs are based on InAs/InP QDs, which can emit single photons at telecommunication wavelength. To realize the efficient output of waveguide-coupled photons, a PhC mirror is implemented in the waveguide. The photon is then guided from the waveguide to a lensed fiber installed next to the silicon chip. For the efficient waveguide-fiber coupling, the edges of the waveguide are terminated by SSCs, allowing the efficient waveguide-fiber coupling by adiabatically converting a waveguide propagating mode to a free space mode.

8.2.1 Simulated output efficiency of InP-based QD SPS

We designed the InP-based SPS structure coupled to the underneath silicon waveguides following the discussion of chapter 3. We considered an InP-based nanobeam cavity with a width of 580 nm and a thickness of 300 nm. For the nanobeam cavity, the period of holes is $a = 380$ nm, and the radius of air holes is $r = 0.27a$. We employed the same modulation rule for the cavity center, as discussed in chapter 3, resulting in the formation of a high-Q PhC nanobeam cavity. For the cavity without silicon waveguides, the fundamental mode of the cavity exhibits a high quality factor of $Q = 5.7 \times 10^6$ and a small mode volume of $V = 0.62 \times (\lambda/n)^3$ with resonant wavelength of $\lambda = 1,490$ nm. For the waveguide, we considered a silicon photonic waveguide with a width of 400 nm and a thickness of 210 nm. To achieve efficient single-photon output into the fiber, we implemented a PhC mirror into the waveguide (period of holes: $A = 400$ nm, radius of holes: $R = 0.26A$).

We optimized the unidirectional coupling of the cavity fundamental mode into the silicon waveguide (η_{uni}) by controlling the vertical distance between them (d). For $d = 380$ nm, maximum η_{uni} was simulated to be 98.1% with the quality factor of $Q = 830$. At the same time, we obtained high QD-cavity coupling efficiency β of 99.5% thanks to the large Purcell enhancement facilitated by the very small V . As a result, the overall single-photon coupling efficiency ($\eta_{uni}\beta$) unidirectionally coupled to the waveguide took a maximum value of 97.6%. These numerical results demonstrated that our SPS structure with InP nanobeam cavities is a powerful device design compatible with silicon photonics.

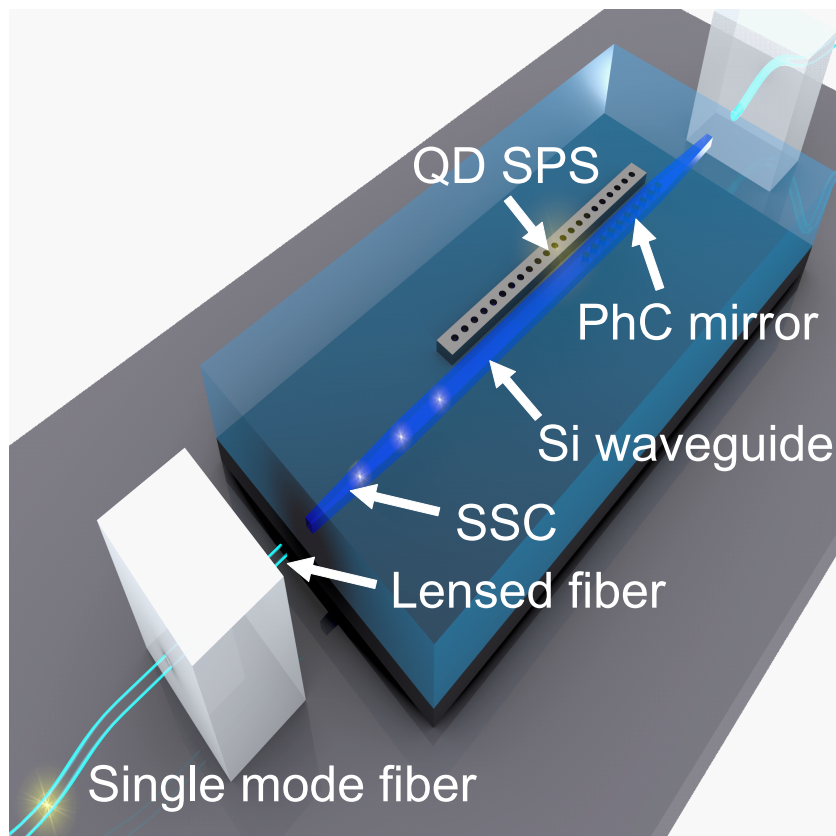


Figure 8.1: Schematic of the investigated fiber-pigtailed QD SPSs on a silicon CMOS chip.

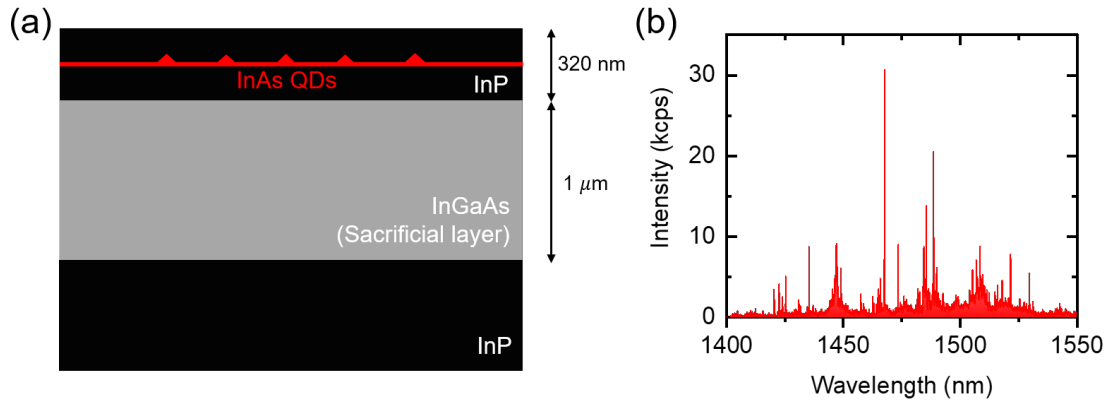


Figure 8.2: (a) The structure of the sample wafer utilized in this study. (b) PL spectrum of our typical InP/InAs QDs sample measured at 6 K.

8.3 Fabrication of InP PhC nanobeam cavity

In this section, we describe the fabrication of QD SPSs based on InP nanobeam cavities. For the efficient fiber output from integrated QDs, the realization of high-Q cavities is of great importance. We developed the fabrication process for InP PhC nanobeam cavities with high Q factors.

8.3.1 Sample growth of InP slab containing InAs QDs

We used a wafer sample of self-assembled InP/InAs QDs by molecular beam epitaxy (MBE). This sample's growth was performed by the University of Kassel group led by Prof. Mohamed Benyoucef in collaboration with Prof. Johann Peter Reithmaier. The single layer of InAs QDs is located at the middle of 320 nm-thick InP slab grown on $\text{In}_{0.532}\text{Ga}_{0.468}\text{As}$ sacrificial layer. Figure 8.2(b) shows a PL spectrum of our typical InP/InAs QDs sample measured at 6 K. We can see the sharp QD peaks homogeneously distributes from 1,400 to 1,530 nm.

8.3.2 Sputtering SiO_2 hard mask

To enhance the etching selectivity, we used SiO_2 as a hard mask. The SiO_2 was deposited by the sputtering process. The thickness of the deposited SiO_2 mask was 200 nm in this work.

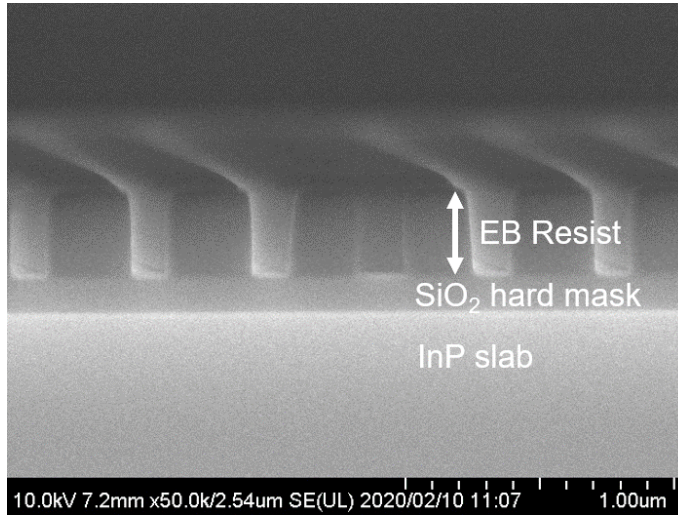


Figure 8.3: SEM image of the cross-section of the sample after the development.

8.3.3 EB Resist for preparing SiO_2 hard mask

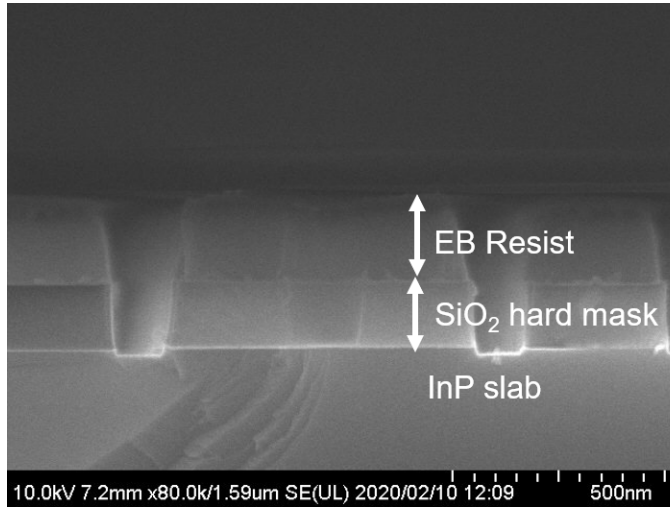
We employed ZEP 520A(ZEON Corp.) as an electron beam (EB) resist. To prepare the mask for dry etching the hard mask, we conducted the same spin coating processes, EB lithography, and development as described in chapter 4. We patterned the PhC nanobeam cavities with the lattice constants of $a = 360, 370$ and 380 nm and radius of $r = 0.265 \times 360$ nm. Figure 8.3 shows an SEM image of the sample's cross-section after the development. We can see the patterned PhC nanobeam cavities in the middle of the image. For the easy evaluation of the PhC air holes on the cleaved sample cross-section, we also patterned the 2D PhC with the lattice constant of $A = 360$ nm and radius of $r = 0.275A$.

8.3.4 Dry etching SiO_2 hard mask

To transfer the pattern from the EB resist to the hard mask, we conducted dry etching by inductively coupled plasma ion etching using CF_4 and Ar gases. We used the etching machine (Samco international, RIE-200iP). Table 8.1 summaries utilized parameters for this work. Figure 8.4 shows an SEM image of the sample's cross-section after the dry etching of the SiO_2 hard mask.

Table 8.1: Utilized parameters for dry-etching SiO_2 hard mask.

CF_4	Ar	Pressure	Bias	ICP	Etching time
5.0 sccm	6.0 sccm	0.75 Pa	500 W	125 W	2 min

Figure 8.4: SEM image of the cross-section of the sample after dry etching SiO_2 hard mask.

8.3.5 Dry-etching InP layer

We dry-etched the sample by using the ICP RIE system. For etching the InP slab, we used BCl_3 and Ar for reactive and inactive gas, respectively [148, 149]. We used the etching machine (Samco international, RIE-101iP), which is shown in Fig. 8.5. To facilitate the chemical etching with BCl_3 gas, the sample was kept at 150°C by using both an oil chiller and He gas flow under the sample-chuck with the pressure of 7×10^2 Pa. Now we describe the details of the etching condition for the InP layer.

Low-pressure operation

To realize high-Q PhC cavities, it is necessary to form a smooth vertical sidewall of air holes in the InP layer. For this purpose, we reduced the pressure of the chamber. We expected that the low-pressure operation increases the mean free path of the accelerated etching species and its anisotropy in the etching, leading to the



Figure 8.5: Photography of the ICP RIE machine used in this study (RIE-101iP).

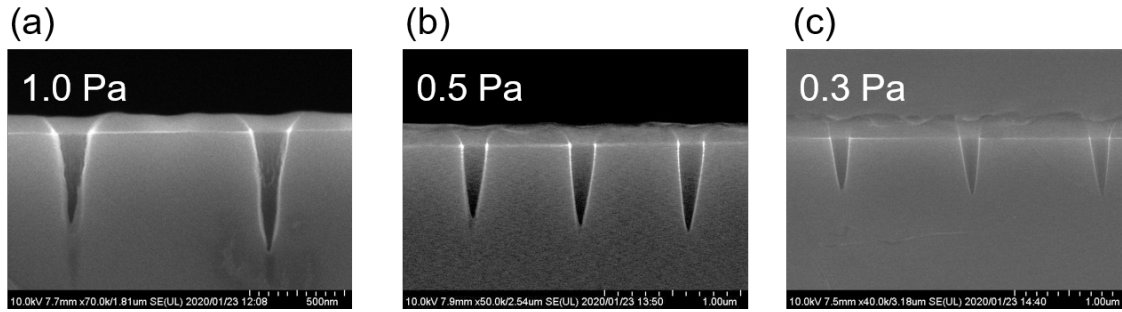


Figure 8.6: SEM images of the cross-section of the sample after the dry etching with the chamber pressure of (a) 1.0 Pa, (b) 0.5 Pa, and (c) 0.3 Pa. Other employed parameters are listed in Table 8.2.

air holes' vertical sidewalls. Also, lower pressure reduces the evacuation of etched products and decreases the possibility of reactant re-deposition, resulting in a smooth sidewall. Figure 8.6 summarizes SEM images of the cross-section of the 2D PhC after the dry etching with the chamber pressure of (a) 1.0 Pa, (b) 0.5 Pa, and (c) 0.3 Pa. The employed parameters are listed in Table 8.2. As the pressure is reduced, we can see the smoother and more vertical sidewall of air holes in the InP slab. Therefore we set the chamber pressure of 0.3 Pa in this study.

Table 8.2: Utilized parameters for dry-etching InP slab while changing the chamber pressure.

BCl_3	Ar	Pressure	Bias	ICP	Etching time
10 sccm	0 sccm	1~0.3 Pa	100 W	300 W	3 min

Optimization of bias power

Next, the bias power was optimized to make the sidewall of air holes more vertical. Figure 8.7 summarizes SEM images of the cross-section of the 2D PhC (upper panels) and nanobeam cavities (lower panels) after the dry etching with the bias power of (a) 75 W, (b) 100 W, (c) 150 W, and (d) 180 W. The employed parameters are listed in Table 8.3. As the bias power increased, we can see the sharp sidewall of air holes in the InP slab. Notably, the resist did not remain on the sample when we further increased the bias power. In this study, we set the bias power of 160 W.

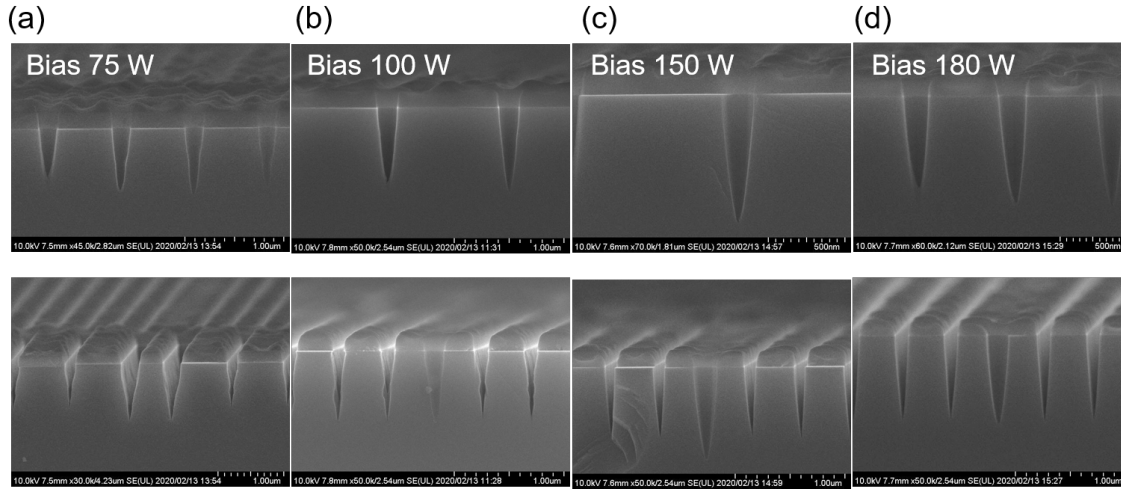


Figure 8.7: SEM images of the cross-section of the sample after the dry etching using the recipe of Table 8.3.

Table 8.3: Utilized parameters for dry-etching InP slab.

BCl_3	Ar	Pressure	Bias	ICP	Etching time
10 sccm	0 sccm	0.3 Pa	75~180 W	200 W	5 min

Employed recipe with Ar

Finally, we added Ar gas for more vertical sidewalls. Figure 8.7 displays an SEM image of the cross-section of the nanobeam cavity after the dry etching with the recipe of Table 8.4. Notably, a higher temperature is preferred for enhancing chemical etching [150], but we could not try the etching at higher temperatures since the RIE machine cannot normally work at a temperature over 160 C°.

Table 8.4: Utilized parameters for dry-etching InP slab.

BCl_3	Ar	Pressure	Bias	ICP	Temperature	Etching time
10 sccm	5 sccm	0.3 Pa	160 W	200 W	160 C°	5 min 5 s

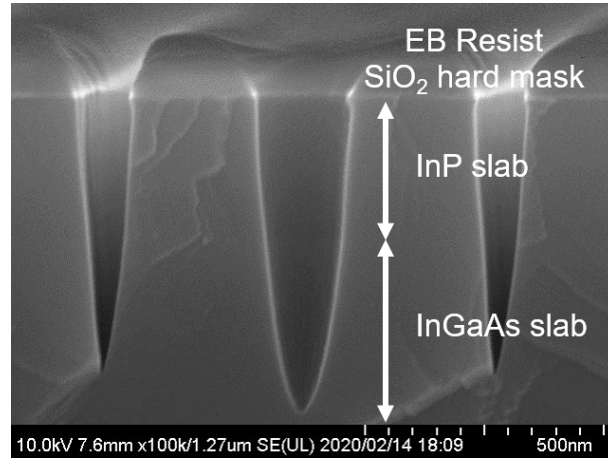


Figure 8.8: SEM image of the cross-section of the sample after the dry etching using the recipe of Table 8.4.

8.3.6 Removing EB resist and SiO₂ hard mask

We removed the EB resist after the entire dry etching process. The process for removing EB resist was the same as that of chapter 4. Next, we removed the SiO₂ hard mask on the sample. We used an HF solution diluted by 10% with high-purity water (HF:H₂O = 1:4). We dipped the sample in this HF solution for 10 minutes at room temperature. Then we rinsed the sample about 10 times using high-purity water.

8.3.7 Wet chemical etching

Finally, we wet etched the sample using a sulfuric acid solution (H₂SO₄, FUJIFILM Wako Pure Chemical Corp.) to form an airbridge sample structure. H₂SO₄ solution was diluted with hydrogen peroxide (H₂O₂) and high-purity water (H₂SO₄:H₂O₂:H₂O = 1:1:10). H₂SO₄-based solution was kept at 5 °C in a cool bath for isotropic etching of the InP layer. We dipped the sample in this solution for 6.5 minutes. Then we rinsed the sample about 10 times using high-purity water.

Figure 8.9 shows an SEM image of the fabricated sample after wet chemical etching. We can see that the sacrificed 1 μ m-thick InGaAs layer is dissolved. We can also confirm the smooth sidewall of the air-holes. We note that the selectivity of InGaAs compared to InP in this process is ~ 24 (170 nm / 7 nm), resulting in the reduced InP slab thickness of 300 nm.

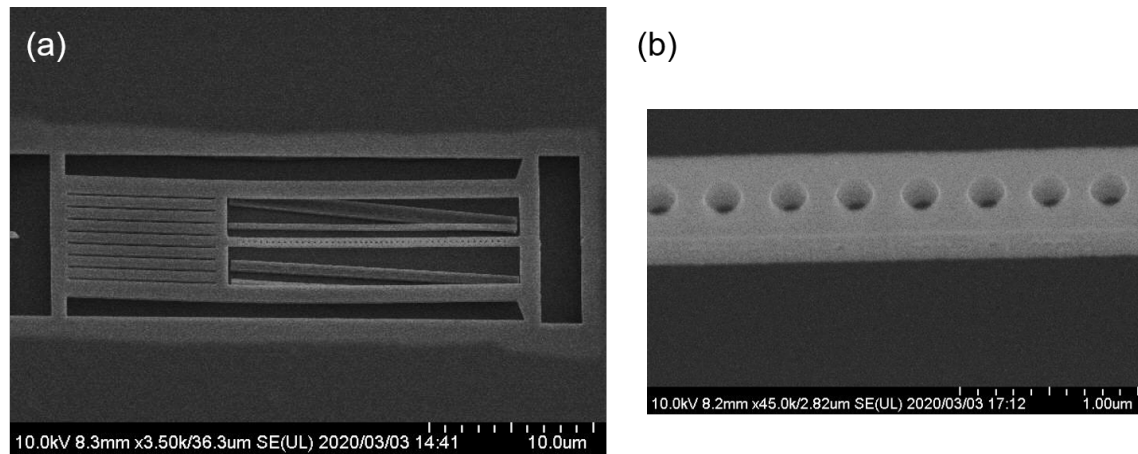


Figure 8.9: SEM image of the fabricated sample after wet chemical etching. (a) Overview, (b) Magnified view.

8.4 Implementation of pigtail fibers into silicon CMOS chip

In this section, we describe the details of fiber-pigtailed silicon CMOS chips. For the efficient waveguide-fiber coupling, we utilized SSCs, which allows the efficient waveguide-fiber coupling by adiabatically converting the waveguide mode to a free space mode. We describe the details of implementing lensed fibers into the silicon chip.

8.4.1 Dry etching clad while protecting SSCs

Before implementing lensed fibers with the silicon chip, we controlled the glass thickness above the silicon waveguide for efficient QD-to-waveguide coupling. For this purpose, we dry-etched the glass layer above the silicon waveguide ($= d$) by using inductively coupled plasma ion etching with CF_4 and Ar gases. We tuned d to 360 nm in this study. To prevent the degradation of SSCs during the etching process (e.g., contamination and destruction of the edge of SSCs), we covered them with a non-toxic polymer (First contact, Photonics Cleaning Technologies). The polymer was coated on the sidewall of the sample chips with the brush. After the dry etching, the polymer was removed by using ZDMAC, the details of which are described in chapter 3. Figure 8.10 shows a microscope image of the SSCs after removing the polymer. We can see a clear image of SSCs without any noticeable

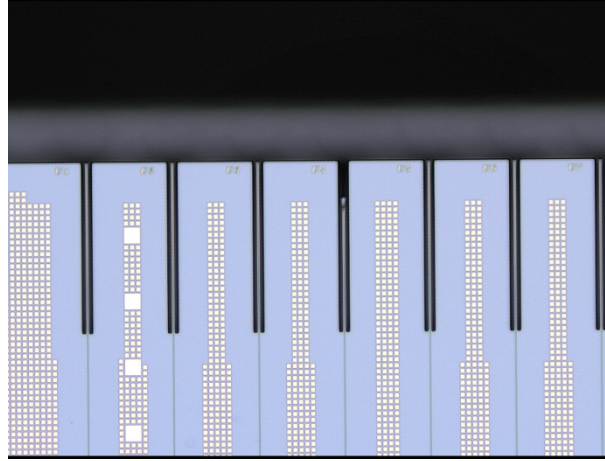


Figure 8.10: Microscope image of the SSCs after removing the polymer.

dust and contamination.

8.4.2 Implementation of lensed fibers into SSCs

Lensed fibers were implemented into the dry-etched silicon CMOS chip. The processes described here were conducted by Adamant Namiki Precision Jewel Co., Ltd. The lensed fibers were fixed on an alumina substrate with glass boxes and ultraviolet curing resin after the alignment of the fibers to the SSCs. Figure 8.11(a) shows a photograph of the silicon CMOS chip implemented with lensed fibers. The fibers were ended with LC-type fiber connectors, whose size is small enough to put the whole sample inside our cryostat. The fiber-to-fiber transmission loss of this sample was measured to be 10.3 (9.8) dB at 1,550 (1,640) nm. To prevent the shift of the implemented fiber under the cryogenic condition, the edge of the fiber was fixed on the silicon chip by ultraviolet curing resin as shown in Fig. 8.11(b). The transmission loss of this sample after this process was measured to be 10.2 (10.0) dB at 1,550 (1,640) nm.

8.5 Fabrication of the device using transfer printing

In this section, we describe the hybrid integration of InAs/InP QD SPSs on the fiber-pigtailed silicon CMOS chip. In this study, we integrated a QD SPS that was

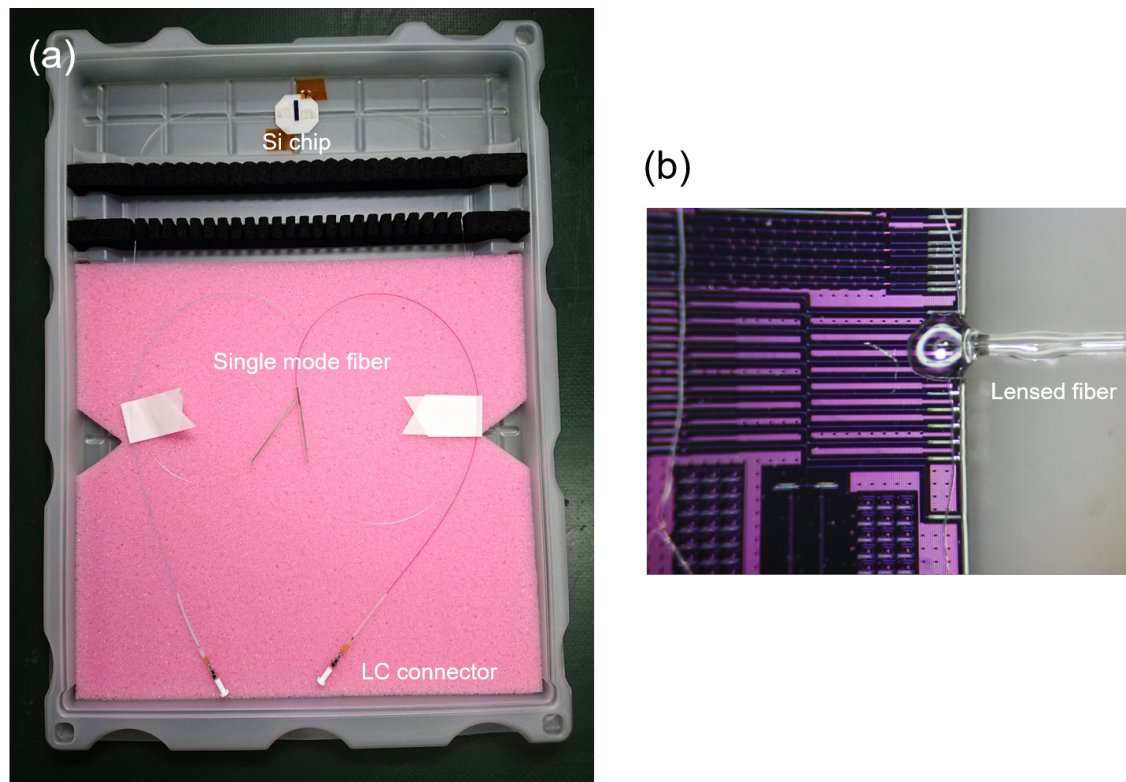


Figure 8.11: (a) Photograph of the silicon CMOS chip implemented with lensed fibers. (b) Photograph of the silicon CMOS chip after fixing the edge of the fiber on the silicon chip by ultraviolet curing resin.

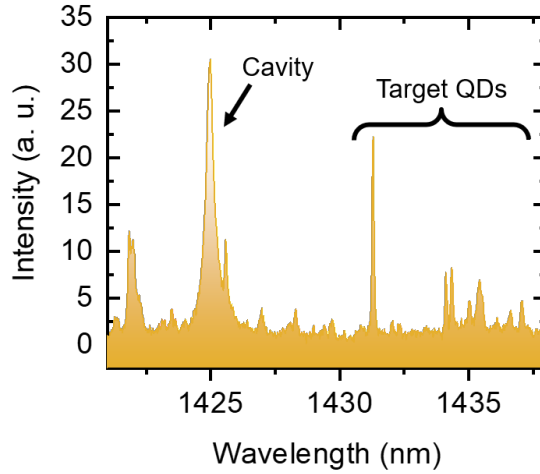


Figure 8.12: PL spectrum measured for Cavity-A at 6 K (pumping power = 1 μ W).

pre-characterized before the transfer printing. The hybrid integration was performed using an improved transfer-printing apparatus.

8.5.1 Pre-characterization of the InP/InAs QD SPS

Before the transfer printing process, we evaluated the optical property of the InP-based nanobeam cavities. We measured PL spectra for the fabricated nanobeam cavities with low-temperature μ PL measurements. We utilized a diode laser oscillating 785 nm for the optical pumping. Figure 8.12 shows the PL spectrum measured at 6 K (pumping power = 1 μ W). We can see that the cavity resonant mode at 1,425 nm (labeled as Cavity-A). Also, QD emission peaks can be seen around 1,435 nm in Fig. 8.12. FDTD simulations revealed that the wavelength of the cavity resonant mode shifts by about 10 nm when they are transferred from the substrate onto the glass. Thus we can expect the resonance of these target QDs with the cavity after the transfer printing process.

8.5.2 Transfer printing with improved machine

We performed the transfer printing with an improved transfer-printing apparatus, a photograph of which is shown in Fig. 8.13. The system was composed of two

movable stages and an optical microscope module (BXFM-A, Olympus). Details of the improved transfer-printing apparatus are described in Appendix A.

8.5.3 Integration of InP/InAs QD SPS on processed silicon chip

We utilized transfer printing to place a preselected QD SPS onto a silicon waveguide. We picked up Cavity-A by placing a PDMS rubber stamp on it and quickly peeling the rubber stamp off as shown in Fig. 8.14(a). Then we placed the picked-up QD SPS precisely on the silicon waveguide. Subsequently, we slowly peeled off the rubber stamp, leaving only the QD SPS on the silicon waveguide as shown in Figs. 8.14(b). Here, we used PDMS films with thicker pillar structure (pillar height $\sim 10 \mu\text{m}$) to further reduce the total contact area with the sample surface and mitigate unwanted strain on the PDMS film. We utilized AZ P4620 (Merck Corp.) as a photoresist. The detailed explanation of fabricating patterned PDMS films is described in chapter 4.

Figure 8.15(a) shows a microscope image of Cavity-A after the transfer printing process. We can see the precise alignment between the top nanobeam cavity and the underlying silicon waveguide. We then placed the sample inside a liquid helium flow cryostat (Fig. 8.15(b)) to cool down the sample around 4 K and keep the quantum nature of the InAs/InP QDs. To put the fibers inside the cryostat, the fibers were attached to the thermal radiation shield with Kapton tapes.

We also utilized a fiber-feedthrough to provide a flexible optical path into a vacuum cryostat, as shown in Fig. 8.15(b). The feedthrough was made by filling the vacuum flange with epoxy resin. The fiber feedthrough had two single-mode fibers, which were terminated with LC and FC fiber connectors. We confirmed that our home-made fiber-feedthrough allows the vacuum condition with little transmission loss.

8.6 Optical characterization of fiber-pigtailed QD SPS

In this section, we experimentally investigated the fabricated device with low-temperature μPL measurements. The setup of the optical measurement is almost the same as that of chapter 6. The signal was collected from the fiber, collimated with an achromatic collimator (N.A. = 0.36, RC04FC-F01, Thorlab), and sent to a grating spectrometer equipped with an InGaAs camera.

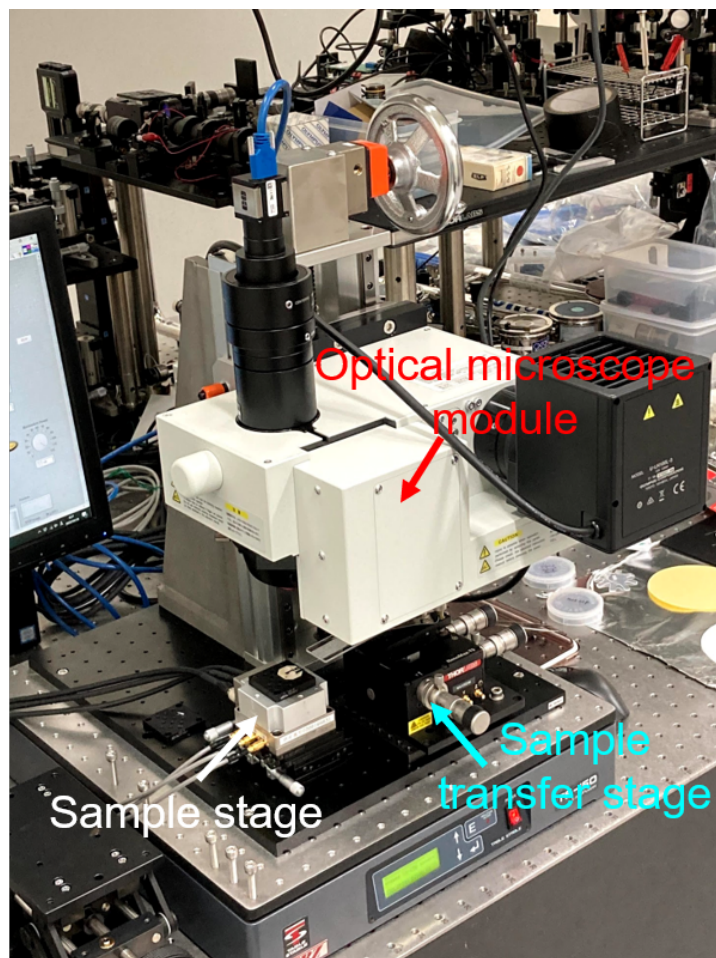


Figure 8.13: Photograph of the improved transfer-printing apparatus. The system was composed of two movable stages and an optical microscope module (BFXM-A, Olympus).

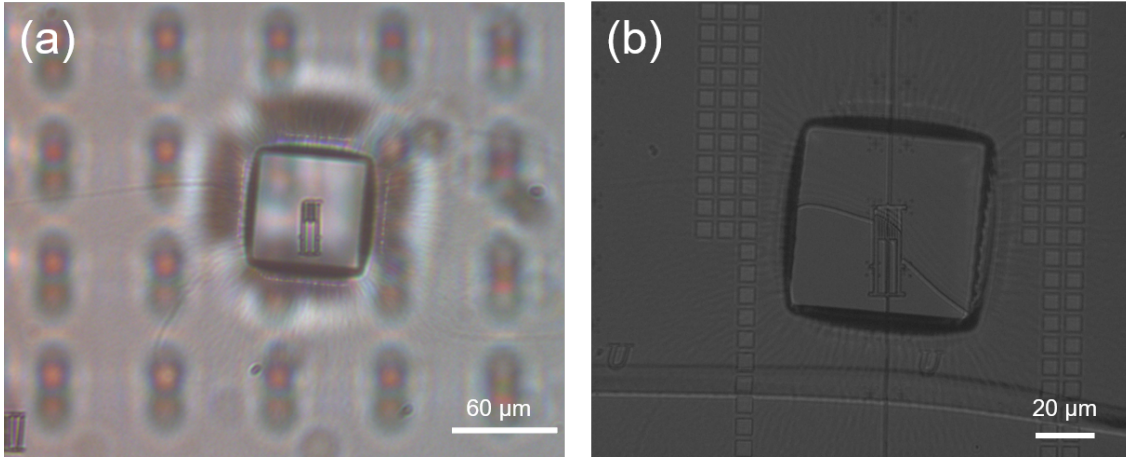


Figure 8.14: Microscope images of the pick-and-place processes. (a) We attached a PDMS film to a selected air-bridged nanobeam cavity and quickly peeled the film off by moving an actuator of sample transfer stage in the vertical direction. (b) We slowly peeled the stamp off to release the cavities on the silicon waveguide.

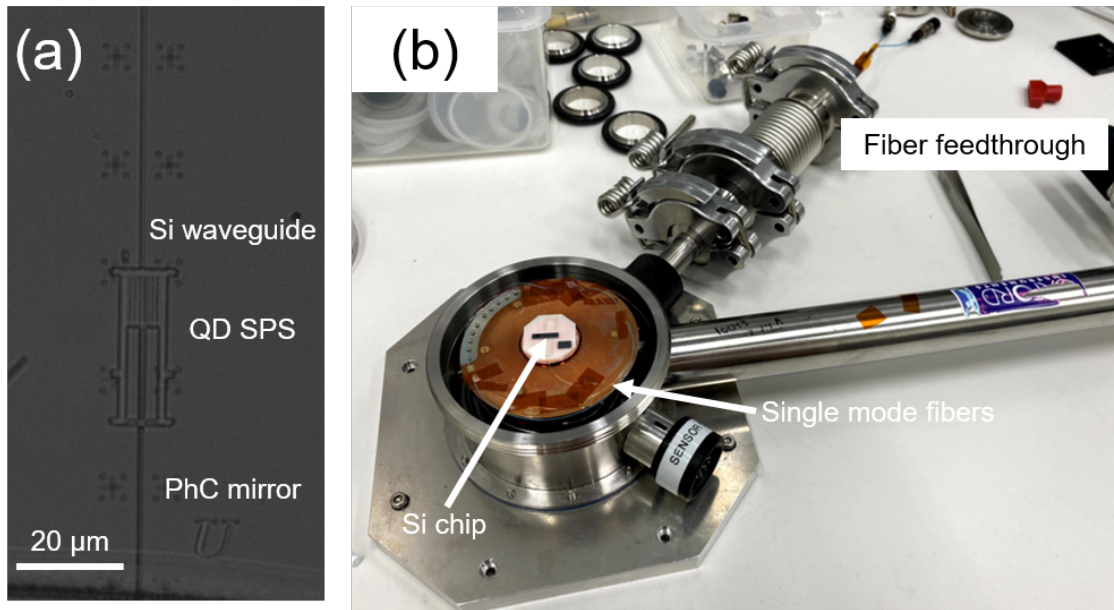


Figure 8.15: (a) Microscope image of Cavity-A after the transfer printing process. (b) Photograph of the sample for low-temperature μ PL measurements.

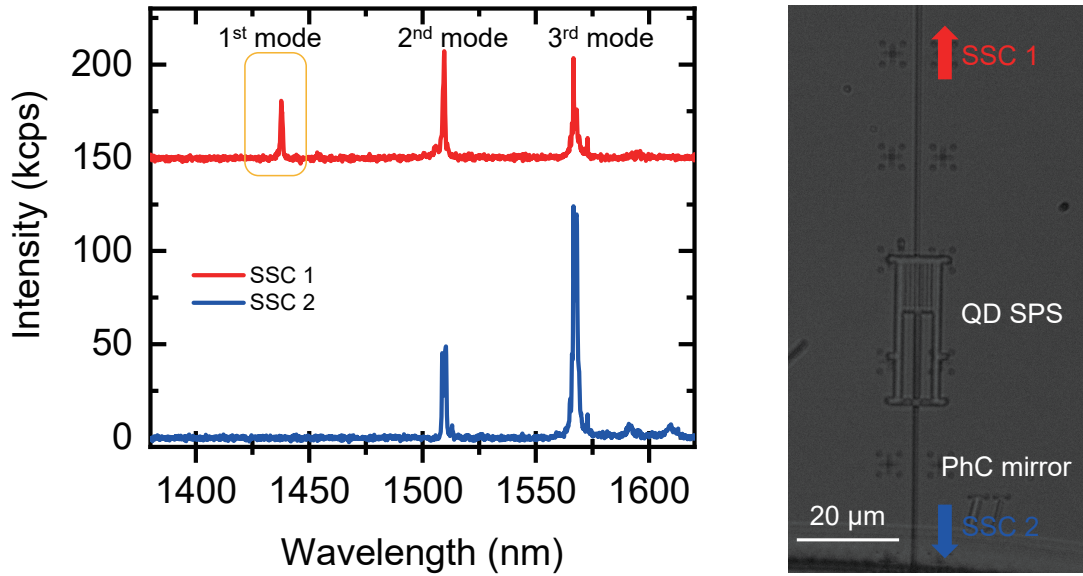


Figure 8.16: Measured PL spectra from fibers (red: SSC 1, blue: SSC 2).

8.6.1 PL spectra extracted from optical fibers

We measured PL spectra from fibers connected to SSC 1 (2) at 5 K for a wide spectral range with a pump power of 300 nW ($1 \mu\text{W}$), as shown in the red (blue) curve in Fig. 8.16. In the red curve in Fig. 8.16, we observed strong peaks of all the cavity resonant mode (first mode: 1,438 nm, second mode: 1,510 nm, third mode: 1,567 nm). On the other hand, we could not observe the peak of the first cavity resonant mode in the blue curve due to the light reflection by the PhC mirror. These results indicate the unidirectional output of the fundamental cavity mode from SSC 1 into the fiber.

To investigate the emission nature of the QDs, we first measured the PL spectrum from the fiber of SSC 1 by using a CW Ti:sapphire laser (above-band excitation, wavelength = 860 nm, excitation power = 200 nW). Figure 8.17(a) shows the PL spectrum measured from the fiber connected to SSC1 at 8 K. We observed a strong peak of the cavity mode emission at 1,438.5 nm, together with cavity-coupled QD emission at 1,439.3 nm (labeled as QD-A). We consider that this QD emission comes from one of the target QDs pre-characterized in the previous section. Besides, we can see no other signals in Fig. 8.17(a), showing that we succeeded in the extraction

of QD emission through the optical fiber.

8.6.2 Observation of Purcell-enhanced QD emission from optical fiber

To confirm the Purcell enhancement of QD-A, we also conducted time-resolved PL measurements for QD-A. For this purpose, we switched the pump laser to a pulsed Ti:sapphire laser oscillating at 860 nm, average pump power of ~ 10 nW, pulse width of ~ 1 ps, and repetition rate of 80.3 MHz. We employed a time-correlated single-photon counting technique with an SNSPD (overall system time resolution of ~ 50 ps). We used the spectrometer as a bandpass filter of the collected PL signal. Then we focused the PL signals on the port of an optical fiber by using an x10 objective lens to send the signals to the SNSPD. We measured the time-resolved PL spectrum for the QD-A peak at 7.4 K, as shown in the red curve in Fig. 8.17(b). Here, we slightly detuned QD-A by 1.5 nm from the cavity resonant wavelength to suppress the intrusion of the cavity background peak. Compared with the emission decay of bare QDs (black curve), we can see a rapid emission decay of QD-A. We fitted the measured curve with double exponential decay curves convolved with a function that reflects the system time response. From the red curve in Fig. 8.17(b), the emission rate of QD-A was measured to be $\gamma_{exp} = 3.1$ GHz (decay lifetime of 320 ps).

8.6.3 Estimation of total fiber output efficiency of single photons

The total fiber output efficiency of single photons (η_{out}) was evaluated as below. First, we estimated an experimental cavity-waveguide coupling efficiency (η_{uni}^{exp}) based on the measured cavity quality factors, whose details are described in chapter 4. From the PL spectrum in Fig. 8.16(a), we deduced the experimental quality factor of the cavity as $Q_{exp} = 2,200$. For comparison, we evaluated the quality factors of the cavities on the plane glass. The average quality factor (Q_{ave}) estimated from 10 bare nanobeam cavities is estimated to be 7,200. Based on the obtained Q_{exp} and Q_{ave} , we deduce an η_{uni}^{exp} of 70%, demonstrating the efficient coupling of the cavity mode into the silicon waveguide.

Next, we estimated the experimental QD-cavity coupling efficiency (β^{exp}) based on γ_{exp} and the obtained emission rates of based QDs, whose detailed discussions are shown in chapter 4. We measured emission decay rates of several QDs in unprocessed area. The averaged decay rate was measured to be 0.43 GHz (corresponding decay lifetime of 2.3 ns), resulting in the decay rate γ_{other} of 0.217 GHz. From these

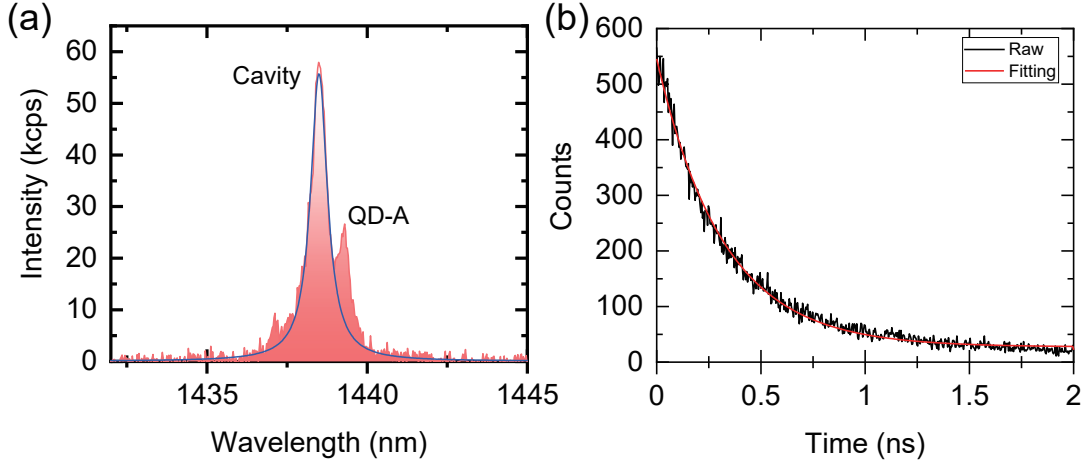


Figure 8.17: (a) PL spectrum measured from the fiber connected to SSC1. (b) Time-resolved PL spectrum measured for the QD-A emission at 7.4 K when QD-A is slightly detuned from the cavity resonance by 1.5 nm.

emission rates and the equation (4.4), the estimated emitter-cavity coupling efficiency from these measurements deduced to be $\beta^{exp} \sim 94\%$. Using the values of $\eta_{uni}^{exp} = 70\%$ and $\beta^{exp} \sim 94\%$, the total single-photon coupling efficiency is estimated to be $\eta_{uni}^{exp} \beta^{exp} \sim 65\%$ with unidirectional output.

Finally, we estimated the fiber output efficiency from the waveguide (η_{fiber}) for this sample. For this purpose, we input CW laser oscillating at 1,600 nm into the fiber of SSC 2 using a wavelength-tunable CW laser (Santec), and measured the output power from the fiber of SSC 1 using a power meter. Under this setup, fiber-to-fiber transmission ratio ($T = \eta_{fiber}^2$) was measured to be 0.013 at 1,600 nm, resulting in η_{fiber} of 0.11. As a whole, the total fiber output efficiency of single photons was deduced to be $\eta_{out} = \eta_{fiber} \eta_{uni}^{exp} \beta^{exp} \sim 7\%$. We consider that this value can be improved by reducing the fiber bending loss.

8.6.4 Quasi-resonant excitation of integrated QD

Next, we performed photoluminescence excitation (PLE) measurements [151] at 3.6 K using a wavelength-tunable CW laser (Santec) to investigate the absorption lines of the investigated QD. Excitation power is kept at 220 μ W during the measurement. Figure 8.18(a) and (b) shows the PL spectrum of the QD and corresponding PLE spectrum measured by changing the excitation wavelength ranging from 1,370

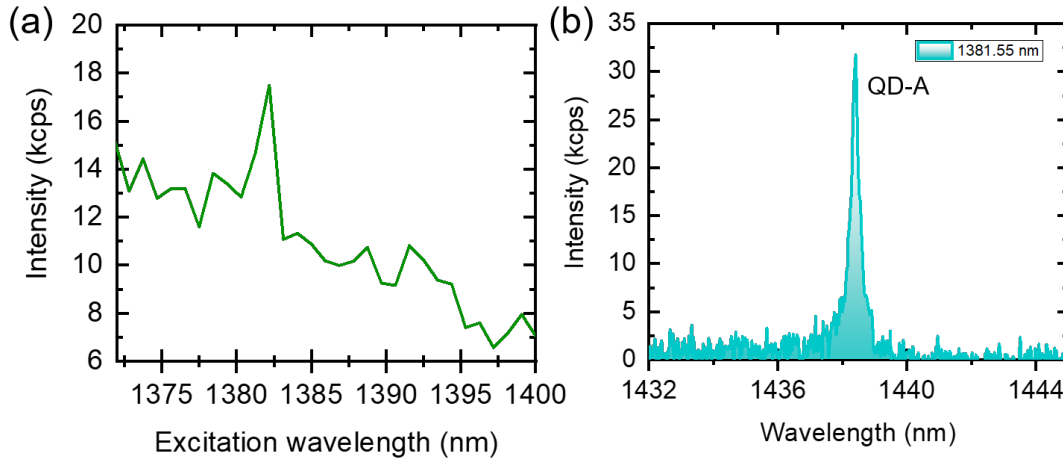


Figure 8.18: (a) PLE spectrum of the QD-A peak. (b) PL spectrum when pumping QD-A with the excitation wavelength of 1,381.55 nm.

to 1,400 nm. The PLE spectrum exhibited a sharp peak ascribed to optical transitions, including those assisted by optical phonons and higher energy levels of QDs. We also observed a broad background across the measurement range of the PLE spectrum. We consider that the nonzero background mainly originated from the intrusion of background cavity emission supplied by other off-resonant QDs or wetting layer inside the cavity.

8.6.5 Observation of single-photon generation

Finally, we conducted second-order correlation measurements based on a Hanbury Brown-Twiss setup when QD-A was slightly detuned from the cavity resonance by 0.46 nm. For this measurement, we added a 50/50 fiber beamsplitter (center wavelength = 1,450 nm, bandwidth = ± 100 nm) and an SNSPD into the photon counting setup. Here, we utilized a CW laser (wavelength = 1,381.6 nm, excitation power = 220 μ W) for the efficient excitation of QD-A.

Figure 8.19(a) shows a PL spectrum measured from the fiber connected to SSC 1. We filtered the emission peak of QD-A at 1,438.5 nm and sent it to the interferometer. Figure 8.19(b) shows the normalized second-order correlation function $g^{(2)}(t)$ measured for the QD-A peak at 3.5 K. We can confirm the raw $g^{(2)}(0)$ value < 0.4 . We also observed bunching phenomena at zero time delay, as observed with quasi-resonant (p-shell) excitation in [152], and could be related to coupling of the

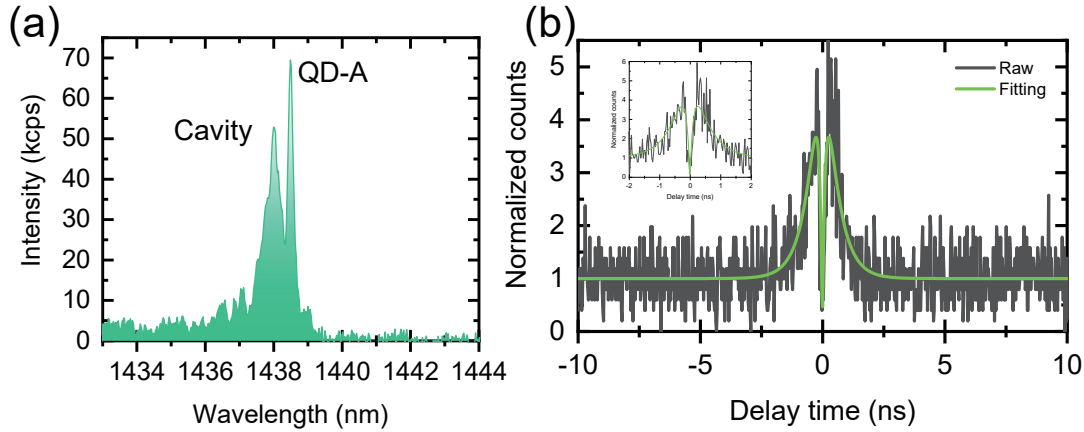


Figure 8.19: (a) PL spectrum measured at one of the output ports when the cavity center is pumped using a CW laser at 1,381.6 nm. (b) Normalized second-order correlation function $g^{(2)}(t)$ measured for QD-A.

radiative excited state to dark states [81]. Relatively large blinking effect of our data is due to the strong excitation power. By taking into account the bunching effect together with an imperfection of anti-bunching at zero time delay ($g^{(2)}(0)$), we fitted the obtained data with the following function:

$$g^{(2)}(t) = 1 - [1 + C - g_{fit}^{(2)}(0)] \exp(-|t|/\tau) + C \exp(-|t|/\tau'), \quad (8.1)$$

where τ is the decay time of QD-A, τ' is the decay time and t is the delay time. The fitted curve was depicted by the green curve in Fig. 8.19(b). An anti-bunching with $g_{fit}^{(2)}(0) < 0.1$ at zero delay demonstrated single-photon generation from QD-A.

8.7 Summary

In this chapter, fiber-pigtailed QD SPSs hybrid integrated on a silicon CMOS chip was presented. To achieve the efficient fiber output of single photons, a telecom QD SPS was hybrid integrated on a fiber-pigtailed silicon CMOS chip using transfer printing, which enables us to take full advantage of mature silicon photonics components. Observation of Purcell-enhanced QD emission through the optical fiber was demonstrated with the single-photon generation in the fabricated device.

Chapter 9

Conclusion and future prospect

9.1 Conclusion

In this thesis, we have developed QD SPSs hybrid integrated on optical circuits toward large-scale integrated quantum photonics. To overcome the challenges of hybrid integrated QD SPSs discussed in chapter 1, we focused on transfer printing. Details of the main achievements are summarized as below.

First, we have developed a hybrid integration technology based on transfer printing. We have theoretically demonstrated that our SPS structure's design enables the coupling of single-photon emission from QDs into the waveguide over 99%. Experimentally, by employing our transfer printing approach, we have demonstrated efficient single-photon coupling into the waveguide, together with the integration of two SPSs into a waveguide. We have also achieved high $\eta_{exp}\beta_{exp}$ of $> 70\%$.

Next, for the first time, we have succeeded in the hybrid integration of a QD SPS on a glass-clad silicon photonic waveguide processed by a CMOS foundry. We numerically showed that the investigated SPS structure could support near-unity coupling of single photons emitted from the QD into the silicon waveguide. We verified single-photon generation from an integrated QD on silicon ($g^{(2)}(0) = 0.30$) and its efficient waveguiding in the CMOS-processed photonic chip with $\eta_{exp}\beta_{exp} \sim 70\%$.

In-situ fine wavelength tuning of QD SPSs on a CMOS-processed silicon waveguide has also been demonstrated. Optically-driven heating pads were utilized to tune the emission wavelengths of integrated QDs thermally. We have obtained the maximum possible tuning range of QD emission wavelength as 0.9 nm. All the necessary hybrid integration processes were performed with transfer printing. We have further demonstrated the spectral matching of two different integrated QD sources on the

same silicon CMOS chip, which is an important step toward scalable silicon quantum photonics to perform two-photon interference with dissimilar identical QD SPSs.

The unidirectional output of QD SPSs hybrid integrated on a silicon waveguide have been demonstrated for efficient single-photon output in PICs. By using a PhC mirror, we have designed the SPS structure to support near-unity efficiency ($> 99\%$) of the QD-to-waveguide coupling with unidirectional light output. By employing an SWG structure as a waveguide, the SPS structure can also support the near-unity efficiency of the single-photon output efficiency in the waveguide, even considering the finite positioning accuracy of hybrid integration by transfer printing. The designed structure has been fabricated using transfer printing. We have demonstrated QD emission's efficient coupling into the silicon SWG waveguide with the output efficiency of $> 70\%$. We have also succeeded in the observation of single-photon generation from an integrated QDs with the $g^{(2)}[0]$ value of 0.28.

Finally, fiber-pigtailed QD SPSs hybrid integrated on a silicon CMOS chip has been demonstrated. We have succeeded in observing Purcell-enhanced QD emission through the optical fiber. Single-photon generation was also verified in the fabricated device.

9.2 Future prospect

We believe that the achievements presented in this thesis will open the possibility toward the realization of scalable integrated optical circuits that leverage cutting-edge PIC technologies. Based on this thesis's experience, we envision several prospects of the hybrid integrated quantum photonics based on our developed technology of on-chip QD-based SPSs. Details of our prospect are summarized in the following text.

9.2.1 On-chip two-photon interference with dissimilar QD SPSs

The above achievements suggest the great potential for the scalable integration of multiple identical QD SPSs onto a CMOS silicon photonic chip. By doing this, we could realize on-chip Hong-Ou-Mandel (HOM) interference with dissimilar QD SPSs on a silicon photonic chip. HOM interference is described as follows. If we send two identical photons simultaneously through the separate input ports of a 50/50 beam splitter, both photons always leave through the same output port due to photons' bosonic nature.

For on-chip HOM interference with dissimilar QD SPSs, our transfer printing approach enables the hybrid integration of two QD SPSs onto a single silicon CMOS chip with desired optical properties as well as the implementation of optically-driven heating pads. The silicon waveguides are combined at a 50/50 optical beam splitter based on a 2×2 MMI coupler. By employing the tuning technology of cavity resonant wavelength based on Xe gas, we could perform fine spectral matching of the integrated nanocavities for QD SPSs. Based on our on-chip thermal tuning technology in chapter 6, we could also perform fine spectral matching of the integrated QD SPSs. We note that for demonstrating HOM interference on chip, it is also important to obtain high indistinguishability between photons from both QDs. For this purpose, it will be necessary to employ resonant [42, 44, 49, 52, 153, 154] or quasi-resonant excitation [46, 50, 155, 156] of integrated QDs.

Toward scalable integrated quantum photonics, it is vital to hybrid integrate not only deterministic QD SPSs but also other functional quantum components on the same PIC [64]. For the case of silicon quantum photonics, efficient and fast single-photon detectors at interesting wavelengths are missing. Quantum memories are also necessary to enable photons to be stored and retrieved with high fidelity [157]. It is of great importance to implement single-photon nonlinearity for efficient photon-photon interaction and deterministic quantum gates [158, 159]. To this end, there are several demonstrations for hybrid integration of these quantum photonic elements. The hybrid integration of superconducting nanowire single-photon detectors on AlN photonics using a nanomanipulator [160] is already reported. Hybrid integration of long-lived diamond quantum memories on Si_3N_4 waveguides is also shown in a pick-and-place manner with a tungsten microprobe [161]. Transfer printing has shown its promise on the on-chip single-photon nonlinearity through the hybrid integration of cavity quantum electrodynamics systems [162]. We believe that transfer printing will be a powerful technology to enable the fusion of these cutting-edge quantum elements and mature modern PIC technologies at will.

9.2.2 Automation of transfer printing

In the current work, the transfer of a QD SPS on a photonic waveguide with high positioning accuracy is done by manual operations and takes approximately 20 minutes on average. To integrate multiple QD SPSs on chip more quickly with higher throughput, the hybrid integration process of transfer printing should be compatible with automation. Several demonstrations have been reported for the automation of transfer printing [163–165]. If our transfer printing system could be automated, it

will be possible to integrate lots of desired QD SPSs on chip in a very short process time.

9.2.3 On-chip boson sampling

If we succeed in the on-chip HOM interference with two dissimilar QD SPSs, the next step is the large-scale photonic quantum simulators, including boson samplers and large-scale entangled photonic cluster states. Boson sampling is considered a strong approach to show quantum supremacy. If we send n identical bosons into an m -mode interferometer and sample from the output distribution, the probability amplitude of the final state is proportional to the permanent of a corresponding $n \times n$ matrix due to the bosonic statistics. Recently, Hui Wang *et al.*, demonstrated boson sampling experiments with 20 photons in a 60 mode fixed interferometer using single photons demultiplexed from a QD [63]. Furthermore, the very recent bulk-optical experiment demonstrated Gaussian boson sampling by sending 50 indistinguishable single-mode squeezed states into a 100-mode ultra low-loss interferometer [166]. If we can extend the above-mentioned approach of on-chip HOM experiment to integrate identical multiple QD-based SPSs on chip with required m -mode interferometer (usually based on the combination of optical beam splitters), we could realize large-scale boson sampling on chip, which will enable us to demonstrate quantum supremacy just on a single chip.

Appendix A

Details of improved transfer printing apparatus

In this chapter, we describe the detailed operation of the new transfer printing machine shown in chapter 8. The system consists of two movable stages and an optical microscope module (BXFM-A, Olympus), as shown in Fig. A.1(a). The system is placed on an anti-vibration table (TS-150, HERZ Corp.).

The sample transfer stage holds a thin glass plate, on which a transparent rubber film is attached. We can manually control the position of the stamp with fine adjusters in the three axes. With the top stage, we can also manually control the pitch and roll of the stamp.

The sample stage holds the sample chips on the top. This stage was equipped with fine adjusters and a three-axis piezo actuator (SFS-H60XYZ(CL), SIGMA KOKI). This piezo stage is connected to the computer via the controller (FINE-503, SIGMA KOKI), enabling us to finely tune the sample positions with Lab View soft. We can manually control the sample rotation by using an incorporated manual rotation stage.

The microscope module consists of a piezo motor of z focus, a white illuminator, the turret equipping several objective lenses (x5, x10, x20, x50, and x100). This module is mounted on the custom stand with the wheel, which allows us to move the module coarsely. This machine allows us to finely focus the sample with electrical control, resulting in a clearer sample image. This module is connected to the computer via the controller (BX-UCB, Olympus). For the quick operation of the transfer printing machine, we used a USB 3.0 CMOS camera (EO-50231, Edmond), which has a high frame rate. The camera image is shown in the right display with the camera viewer, as shown in Fig. A.1(b).

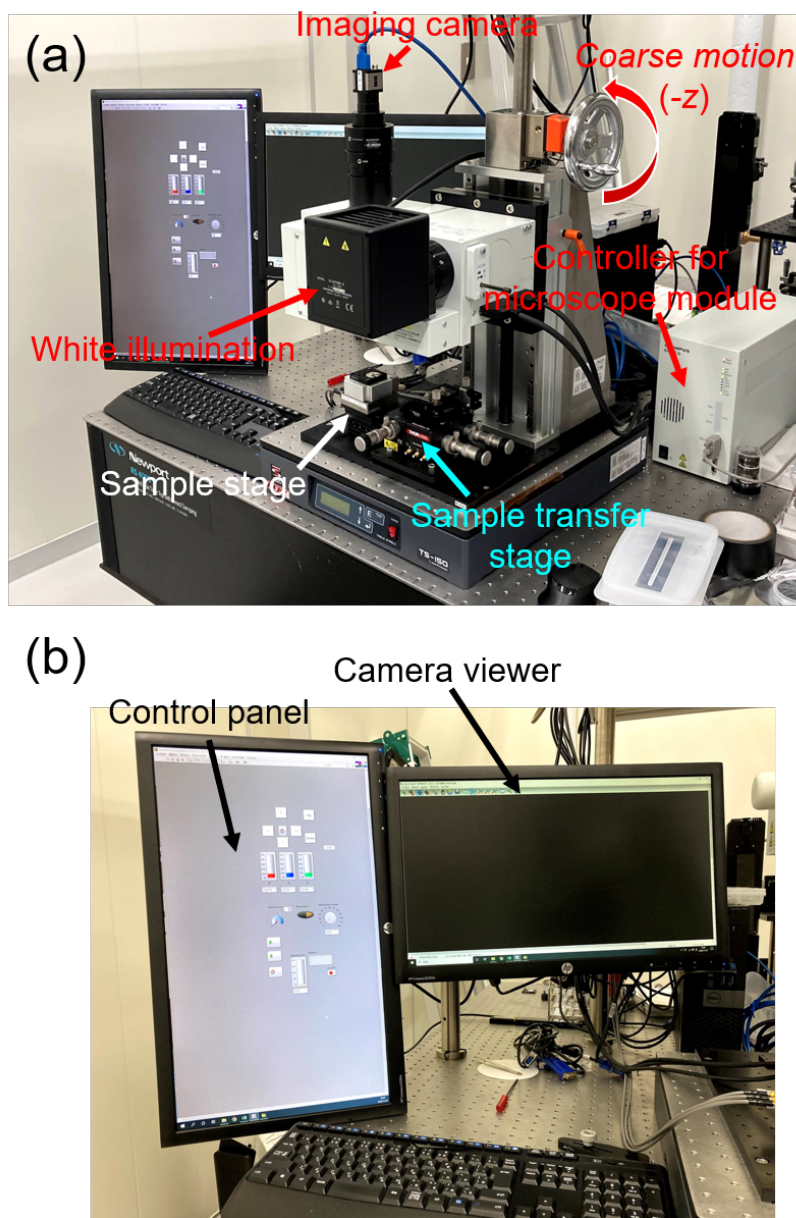


Figure A.1: Photograph of the new transfer-printing apparatus. (a) Overview, (b) The displays of the system.

A.1 Control panel

Figure A.2 shows the Lab View control panel of the new transfer printing machine. The piezo controller is connected to the computer with GPIB cables. The module controller is connected to the computer with a USB cable.

- ① Control panel of the piezo actuators. We can tune the amount of shift in each direction in a single click with the bottom regulators. If press "Up", the sample stage is elevated. If you press "Down", the sample stage is lowered. If we press the button illustrated a house, we can move the stage to the origin.
- ② Control panel of the turret of the objective lenses. 1: x5, 2: x10, 3: x20, 4: x50, 5: x100.
- ③ Control panel of the white illumination. We can tune the power of the illumination with the right regulator.
- ④ Control panel of the objective lens. This controls the position of the objective lens with the piezo actuator implemented in the module. We can tune the amount of shift in a single click with the right yellow regulators. If we press the home button, we can move the stage to the origin.

A.2 Preparation

From now, we describe the operation of the new transfer printing machine. The sample images during the process and after the process are shown in the main text.

1. Turn on the illumination (③).
2. Set sample chips on the sample stage (Fig. A.3) with a paper bond.
3. Cut the home-made PDMS and attach it to the slide glass.
4. Set the slide glass on the sample transfer stage (Fig. A.3). Before the operation, it is better to tune the pitch and roll of the stamp.

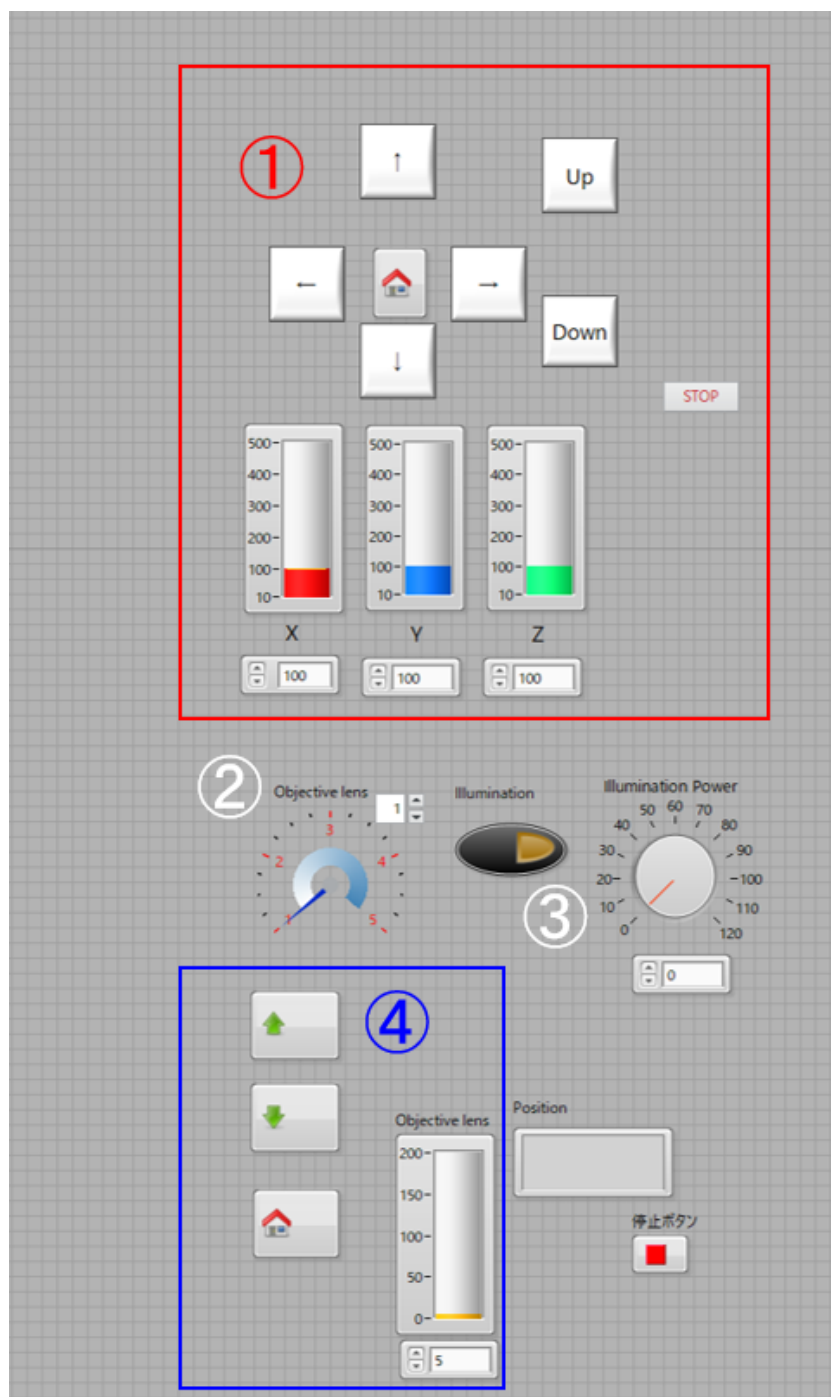


Figure A.2: Lab View control panel of the new transfer printing machine. ① Control panel of the piezo actuators. ② Control panel of the turret of the objective lens. ③ Control panel of the white illumination. ④ Control panel of the objective lens.

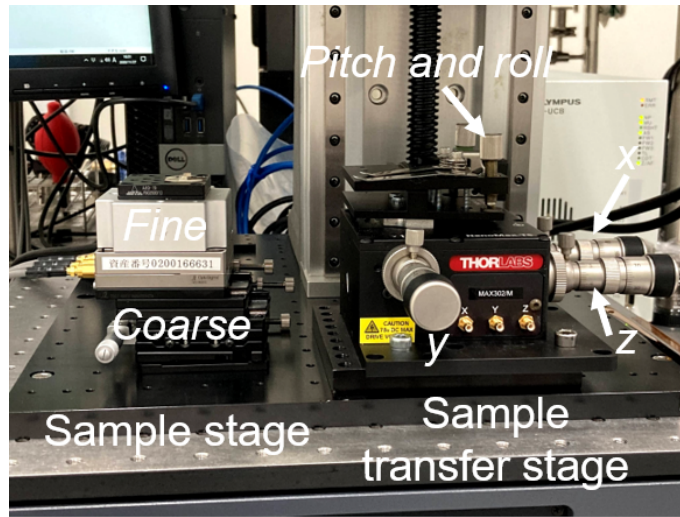


Figure A.3: Photograph of the stages of the new transfer-printing apparatus.

A.3 Operation for pick up

1. To image the sample with low magnification, coarsely move the optical microscope module by turning the wheel.
2. Move to the chip of target QD SPSs.
3. Rapidly turn the z adjuster to peel off the PDMS quickly.

A.4 Operation for placement

1. Move to the chip of target waveguides.
2. Manually align the position of the SPS and waveguide.
3. Approach the PDMS to the target waveguide with the z piezo actuator.
4. Before the printing, change the objective lens from low magnification to x50 or x100 for the precise positioning (②).
5. Electrically align the position of the waveguide (①, ④). Repeat this process for accurate positioning.
6. Smoothly turn the z adjuster to leave the SPSs on the waveguide.

Bibliography

- [1] M. A. Nielsen, I. Chuang, and L. K. Grover, “Quantum Computation and Quantum Information”, *American Journal of Physics*, **70**, 558–559, (2002).
- [2] N. Gisin, G. Ribordy, W. Tittel, and H. Zbinden, “Quantum cryptography”, *Reviews of Modern Physics*, **74**, 145–195, (2002).
- [3] V. Giovannetti, S. Lloyd, and L. Maccone, “Advances in quantum metrology”, *Nature Photonics*, **5**, 222–229, (2011).
- [4] T. D. Ladd, F. Jelezko, R. Laflamme, Y. Nakamura, C. Monroe, and J. L. O’Brien, “Quantum computers”, *Nature*, **464**, 45–53, (2010).
- [5] M. Saffman, “Quantum computing with atomic qubits and Rydberg interactions: progress and challenges”, *Journal of Physics B: Atomic, Molecular and Optical Physics*, **49**, 202001, (2016).
- [6] D. Kielpinski, C. Monroe, and D. J. Wineland, “Architecture for a large-scale ion-trap quantum computer”, *Nature*, **417**, 709–711, (2002).
- [7] Y. Nakamura, Y. A. Pashkin, and J. S. Tsai, “Coherent control of macroscopic quantum states in a single-Cooper-pair box”, *Nature*, **398**, 786–788, (1999).
- [8] J. L. O’Brien, “Optical Quantum Computing”, *Science*, **318**, 1567–1570, (2007).
- [9] J. L. O’Brien, A. Furusawa, and J. Vučković, “Photonic quantum technologies”, *Nature Photonics*, **3**, 687–695, (2009).
- [10] A. Aspuru-Guzik and P. Walther, “Photonic quantum simulators”, *Nature Physics*, **8**, 285–291, (2012).

- [11] F. Arute, K. Arya, R. Babbush, D. Bacon, J. C. Bardin, R. Barends, R. Biswas, S. Boixo, F. G. Brandao, D. A. Buell, B. Burkett, Y. Chen, Z. Chen, B. Chiaro, R. Collins, W. Courtney, A. Dunsworth, E. Farhi, B. Foxen, A. Fowler, C. Gidney, M. Giustina, R. Graff, K. Guerin, S. Habegger, M. P. Harrigan, M. J. Hartmann, A. Ho, M. Hoffmann, T. Huang, T. S. Humble, S. V. Isakov, E. Jeffrey, Z. Jiang, D. Kafri, K. Kechedzhi, J. Kelly, P. V. Klimov, S. Knysh, A. Korotkov, F. Kostritsa, D. Landhuis, M. Lindmark, E. Lucero, D. Lyakh, S. Mandrà, J. R. McClean, M. McEwen, A. Megrant, X. Mi, K. Michielsen, M. Mohseni, J. Mutus, O. Naaman, M. Neeley, C. Neill, M. Y. Niu, E. Ostby, A. Petukhov, J. C. Platt, C. Quintana, E. G. Rieffel, P. Roushan, N. C. Rubin, D. Sank, K. J. Satzinger, V. Smelyanskiy, K. J. Sung, M. D. Trevithick, A. Vainsencher, B. Villalonga, T. White, Z. J. Yao, P. Yeh, A. Zalcman, H. Neven, and J. M. Martinis, “Quantum supremacy using a programmable superconducting processor”, *Nature*, **574**, 505–510, (2019).
- [12] J. G. Ren, P. Xu, H. L. Yong, L. Zhang, S. K. Liao, J. Yin, W. Y. Liu, W. Q. Cai, M. Yang, L. Li, K. X. Yang, X. Han, Y. Q. Yao, J. Li, H. Y. Wu, S. Wan, L. Liu, D. Q. Liu, Y. W. Kuang, Z. P. He, P. Shang, C. Guo, R. H. Zheng, K. Tian, Z. C. Zhu, N. L. Liu, C. Y. Lu, R. Shu, Y. A. Chen, C. Z. Peng, J. Y. Wang, and J. W. Pan, “Ground-to-satellite quantum teleportation”, *Nature*, **549**, 70–73, (2017).
- [13] S.-K. Liao, W.-Q. Cai, J. Handsteiner, B. Liu, J. Yin, L. Zhang, D. Rauch, M. Fink, J.-G. Ren, W.-Y. Liu, Y. Li, Q. Shen, Y. Cao, F.-Z. Li, J.-F. Wang, Y.-M. Huang, L. Deng, T. Xi, L. Ma, T. Hu, L. Li, N.-L. Liu, F. Koidl, P. Wang, Y.-A. Chen, X.-B. Wang, M. Steindorfer, G. Kirchner, C.-Y. Lu, R. Shu, R. Ursin, T. Scheidl, C.-Z. Peng, J.-Y. Wang, A. Zeilinger, and J.-W. Pan, “Satellite-Relayed Intercontinental Quantum Network”, *Physical Review Letters*, **120**, 030501, (2018).
- [14] J. Yin, Y.-H. Li, S.-K. Liao, M. Yang, Y. Cao, L. Zhang, J.-G. Ren, W.-Q. Cai, W.-Y. Liu, S.-L. Li, R. Shu, Y.-M. Huang, L. Deng, L. Li, Q. Zhang, N.-L. Liu, Y.-A. Chen, C.-Y. Lu, X.-B. Wang, F. Xu, J.-Y. Wang, C.-Z. Peng, A. K. Ekert, and J.-W. Pan, “Entanglement-based secure quantum cryptography over 1,120 kilometres”, *Nature*, **582**, 501–505, (2020).
- [15] M. Giustina, M. A. M. Versteegh, S. Wengerowsky, J. Handsteiner, A. Hochrainer, K. Phelan, F. Steinlechner, J. Kofler, J.-Å. Larsson, C. Abellán, W. Amaya, V. Pruneri, M. W. Mitchell, J. Beyer, T. Gerrits, A. E. Lita, L. K. Shalm, S. W. Nam, T. Scheidl, R. Ursin, B. Wittmann, and A. Zeilinger,

- “Significant-Loophole-Free Test of Bell’s Theorem with Entangled Photons”, *Physical Review Letters*, **115**, 250401, (2015).
- [16] B. Hensen, H. Bernien, A. E. Dréau, A. Reiserer, N. Kalb, M. S. Blok, J. Ruitenberg, R. F. L. Vermeulen, R. N. Schouten, C. Abellán, W. Amaya, V. Pruneri, M. W. Mitchell, M. Markham, D. J. Twitchen, D. Elkouss, S. Wehner, T. H. Taminiau, and R. Hanson, “Loophole-free Bell inequality violation using electron spins separated by 1.3 kilometres”, *Nature*, **526**, 682–686, (2015).
- [17] R. Soref, “The Past, Present, and Future of Silicon Photonics”, *IEEE Journal of Selected Topics in Quantum Electronics*, **12**, 1678–1687, (2006).
- [18] D. Dai, J. Bauters, and J. E. Bowers, “Passive technologies for future large-scale photonic integrated circuits on silicon: polarization handling, light non-reciprocity and loss reduction”, *Light: Science & Applications*, **1**, e1–e1, (2012).
- [19] A. Peruzzo, M. Lobino, J. C. F. Matthews, N. Matsuda, A. Politi, K. Poulios, X.-Q. Zhou, Y. Lahini, N. Ismail, K. Worhoff, Y. Bromberg, Y. Silberberg, M. G. Thompson, and J. L. O’Brien, “Quantum Walks of Correlated Photons supplementary”, *Science*, **329**, 1500–1503, (2010).
- [20] A. Aspuru-Guzik and P. Walther, “Photonic quantum simulators”, *Nature Physics*, **8**, 285–291, (2012).
- [21] A. Peruzzo, J. McClean, P. Shadbolt, M.-H. Yung, X.-Q. Zhou, P. J. Love, A. Aspuru-Guzik, and J. L. O’Brien, “A variational eigenvalue solver on a photonic quantum processor”, *Nature Communications*, **5**, 4213, (2014).
- [22] Y.-L. Tang, H.-L. Yin, S.-J. Chen, Y. Liu, W.-J. Zhang, X. Jiang, L. Zhang, J. Wang, L.-X. You, J.-Y. Guan, D.-X. Yang, Z. Wang, H. Liang, Z. Zhang, N. Zhou, X. Ma, T.-Y. Chen, Q. Zhang, and J.-W. Pan, “Measurement-Device-Independent Quantum Key Distribution over 200 km”, *Physical Review Letters*, **113**, 190501, (2014).
- [23] J. Wang, S. Paesani, R. Santagati, S. Knauer, A. A. Gentile, N. Wiebe, M. Petruzzella, J. L. O’Brien, J. G. Rarity, A. Laing, and M. G. Thompson, “Experimental quantum Hamiltonian learning”, *Nature Physics*, **13**, 551–555, (2017).

- [24] J. Carolan, M. Mohseni, J. P. Olson, M. Prabhu, C. Chen, D. Bunandar, M. Y. Niu, N. C. Harris, F. N. C. Wong, M. Hochberg, S. Lloyd, and D. Englund, “Variational quantum unsampling on a quantum photonic processor”, *Nature Physics*, **16**, 322–327, (2020).
- [25] J. Leuthold, C. Koos, and W. Freude, “Nonlinear silicon photonics”, *Nature photonics*, **4**, 535–544, (2010).
- [26] M. J. Collins, C. Xiong, I. H. Rey, T. D. Vo, J. He, S. Shahnian, C. Reardon, T. F. Krauss, M. J. Steel, A. S. Clark, and B. J. Eggleton, “Integrated spatial multiplexing of heralded single-photon sources”, *Nature Communications*, **4**, 1–7, (2013).
- [27] F. Kaneda and P. G. Kwiat, “High-efficiency single-photon generation via large-scale active time multiplexing”, *Science Advances*, **5**, eaaw8586, (2019).
- [28] I. Aharonovich, D. Englund, and M. Toth, “Solid-state single-photon emitters”, *Nature Photonics*, **10**, 631–641, (2016).
- [29] C. Kurtsiefer, S. Mayer, P. Zarda, and H. Weinfurter, “Stable Solid-State Source of Single Photons”, *Physical Review Letters*, **85**, 290–293, (2000).
- [30] D. Englund, B. Shields, K. Rivoire, F. Hatami, J. Vučković, H. Park, and M. D. Lukin, “Deterministic Coupling of a Single Nitrogen Vacancy Center to a Photonic Crystal Cavity”, *Nano Letters*, **10**, 3922–3926, (2010).
- [31] M. Gould, E. R. Schmidgall, S. Dadgostar, F. Hatami, and K.-M. C. Fu, “Efficient Extraction of Zero-Phonon-Line Photons from Single Nitrogen-Vacancy Centers in an Integrated GaP-on-Diamond Platform”, *Physical Review Applied*, **6**, 011001, (2016).
- [32] N. H. Wan, T.-J. Lu, K. C. Chen, M. P. Walsh, M. E. Trusheim, L. De Santis, E. A. Bersin, I. B. Harris, S. L. Mouradian, I. R. Christen, E. S. Bielejec, and D. Englund, “Large-scale integration of artificial atoms in hybrid photonic circuits”, *Nature*, **583**, 226–231, (2020).
- [33] S. Castelletto, B. C. Johnson, V. Ivády, N. Stavrias, T. Umeda, A. Gali, and T. Ohshima, “A silicon carbide room-temperature single-photon source”, *Nature Materials*, **13**, 151–156, (2014).

- [34] D. M. Lukin, C. Dory, M. A. Guidry, K. Y. Yang, S. D. Mishra, R. Trivedi, M. Radulaski, S. Sun, D. Vercruysse, G. H. Ahn, and J. Vučković, “4H-silicon-carbide-on-insulator for integrated quantum and nonlinear photonics”, *Nature Photonics*, **14**, 330–334, (2020).
- [35] A. Högele, C. Galland, M. Winger, and A. Imamoğlu, “Photon Antibunching in the Photoluminescence Spectra of a Single Carbon Nanotube”, *Physical Review Letters*, **100**, 217401, (2008).
- [36] S. Khasminskaya, F. Pyatkov, K. Słowik, S. Ferrari, O. Kahl, V. Kovalyuk, P. Rath, A. Vetter, F. Hennrich, M. M. Kappes, G. Gol’tsman, A. Korneev, C. Rockstuhl, R. Krupke, and W. H. P. Pernice, “Fully integrated quantum photonic circuit with an electrically driven light source”, *Nature Photonics*, **10**, 727–732, (2016).
- [37] Y.-M. He, G. Clark, J. R. Schaibley, Y. He, M.-C. Chen, Y.-J. Wei, X. Ding, Q. Zhang, W. Yao, X. Xu, C.-Y. Lu, and J.-W. Pan, “Single quantum emitters in monolayer semiconductors”, *Nature Nanotechnology*, **10**, 497–502, (2015).
- [38] P. Tonndorf, O. Del Pozo-Zamudio, N. Gruhler, J. Kern, R. Schmidt, A. I. Dmitriev, A. P. Bakhtinov, A. I. Tartakovskii, W. Pernice, S. Michaelis De Vasconcellos, and R. Bratschitsch, “On-Chip Waveguide Coupling of a Layered Semiconductor Single-Photon Source”, *Nano Letters*, **17**, 5446–5451, (2017).
- [39] S. Buckley, K. Rivoire, and J. Vučković, “Engineered quantum dot single-photon sources”, *Reports on Progress in Physics*, **75**, 126503, (2012).
- [40] P. Senellart, G. Solomon, and A. White, “High-performance semiconductor quantum-dot single-photon sources”, *Nature Nanotechnology*, **12**, 1026–1039, (2017).
- [41] S. Hepp, M. Jetter, S. L. Portalupi, and P. Michler, “Semiconductor Quantum Dots for Integrated Quantum Photonics”, *Advanced Quantum Technologies*, **2**, 1900020, (2019).
- [42] N. Somaschi, V. Giesz, L. De Santis, J. C. Loredó, M. P. Almeida, G. Hornecker, S. L. Portalupi, T. Grange, C. Antón, J. Demory, C. Gómez, I. Sagnes, N. D. Lanzillotti-Kimura, A. Lemaître, A. Auffeves, A. G. White, L. Lanco, and P. Senellart, “Near-optimal single-photon sources in the solid state”, *Nature Photonics*, **10**, 340–345, (2016).

- [43] S. Unsleber, Y.-M. He, S. Gerhardt, S. Maier, C.-Y. Lu, J.-W. Pan, N. Gregersen, M. Kamp, C. Schneider, and S. Höfling, “Highly indistinguishable on-demand resonance fluorescence photons from a deterministic quantum dot micropillar device with 74% extraction efficiency”, *Optics Express*, **24**, 8539, (2016).
- [44] X. Ding, Y. He, Z.-C. Duan, N. Gregersen, M.-C. Chen, S. Unsleber, S. Maier, C. Schneider, M. Kamp, S. Höfling, C.-Y. Lu, and J.-W. Pan, “On-Demand Single Photons with High Extraction Efficiency and Near-Unity Indistinguishability from a Resonantly Driven Quantum Dot in a Micropillar”, *Physical Review Letters*, **116**, 020401, (2016).
- [45] G. Kiršanskė, H. Thyrrestrup, R. S. Daveau, C. L. Dreeßen, T. Pregolato, L. Midolo, P. Tighineanu, A. Javadi, S. Stobbe, R. Schott, A. Ludwig, A. D. Wieck, S. I. Park, J. D. Song, A. V. Kuhlmann, I. Söllner, M. C. Löbl, R. J. Warburton, and P. Lodahl, “Indistinguishable and efficient single photons from a quantum dot in a planar nanobeam waveguide”, *Physical Review B*, **96**, 165306, (2017).
- [46] T. Miyazawa, K. Takemoto, Y. Nambu, S. Miki, T. Yamashita, H. Terai, M. Fujiwara, M. Sasaki, Y. Sakuma, M. Takatsu, T. Yamamoto, and Y. Arakawa, “Single-photon emission at 1.5 μm from an InAs/InP quantum dot with highly suppressed multi-photon emission probabilities”, *Applied Physics Letters*, **109**, 132106, (2016).
- [47] L. Hanschke, K. A. Fischer, S. Appel, D. Lukin, J. Wierzbowski, S. Sun, R. Trivedi, J. Vučković, J. J. Finley, and K. Müller, “Quantum dot single-photon sources with ultra-low multi-photon probability”, *npj Quantum Information*, **4**, 43, (2018).
- [48] L. Schweickert, K. D. Jöns, K. D. Zeuner, S. F. Covre da Silva, H. Huang, T. Lettner, M. Reindl, J. Zichi, R. Trotta, A. Rastelli, and V. Zwiller, “On-demand generation of background-free single photons from a solid-state source”, *Applied Physics Letters*, **112**, 093106, (2018).
- [49] H. Wang, Z.-C. Duan, Y.-H. Li, S. Chen, J.-P. Li, Y.-M. He, M.-C. Chen, Y. He, X. Ding, C.-Z. Peng, C. Schneider, M. Kamp, S. Höfling, C.-Y. Lu, and J.-W. Pan, “Near-Transform-Limited Single Photons from an Efficient Solid-State Quantum Emitter”, *Physical Review Letters*, **116**, 213601, (2016).

- [50] G. Kiršanskė, H. Thyrrstrup, R. S. Daveau, C. L. Dreeßen, T. Pregolato, L. Midolo, P. Tighineanu, A. Javadi, S. Stobbe, R. Schott, A. Ludwig, A. D. Wieck, S. I. Park, J. D. Song, A. V. Kuhlmann, I. Söllner, M. C. Löbl, R. J. Warburton, and P. Lodahl, “Indistinguishable and efficient single photons from a quantum dot in a planar nanobeam waveguide”, *Physical Review B*, **96**, 165306, (2017).
- [51] F. Liu, A. J. Brash, J. O’Hara, L. M. P. P. Martins, C. L. Phillips, R. J. Coles, B. Royall, E. Clarke, C. Bentham, N. Prtljaga, I. E. Itskevich, L. R. Wilson, M. S. Skolnick, and A. M. Fox, “High Purcell factor generation of indistinguishable on-chip single photons”, *Nature Nanotechnology*, **13**, 835–840, (2018).
- [52] R. Uppu, F. T. Pedersen, Y. Wang, C. T. Olesen, C. Papon, X. Zhou, L. Midolo, S. Scholz, A. D. Wieck, A. Ludwig, and P. Lodahl, “Scalable integrated single-photon source”, *Science Advances*, **6**, eabc8268, (2020).
- [53] E. Flagg, A. Muller, S. Polyakov, A. Ling, A. Migdall, and G. Solomon, “Interference of Single Photons from Two Separate Semiconductor Quantum Dots”, *Physical Review Letters*, **104**, 137401, (2010).
- [54] P. Gold, A. Thoma, S. Maier, S. Reitzenstein, C. Schneider, S. Höfling, and M. Kamp, “Two-photon interference from remote quantum dots with inhomogeneously broadened linewidths”, *Physical Review B*, **89**, 035313, (2014).
- [55] V. Giesz, S. L. Portalupi, T. Grange, C. Antón, L. De Santis, J. Demory, N. Somaschi, I. Sagnes, A. Lemaître, L. Lanco, A. Auffèves, and P. Senellart, “Cavity-enhanced two-photon interference using remote quantum dot sources”, *Physical Review B*, **92**, 161302, (2015).
- [56] A. Thoma, P. Schnauber, J. Böhm, M. Gschrey, J.-H. H. Schulze, A. Strittmatter, S. Rodt, T. Heindel, and S. Reitzenstein, “Two-photon interference from remote deterministic quantum dot microlenses”, *Applied Physics Letters*, **110**, 011104, (2017).
- [57] J. H. Weber, B. Kambs, J. Kettler, S. Kern, J. Maisch, H. Vural, M. Jetter, S. L. Portalupi, C. Becher, and P. Michler, “Two-photon interference in the telecom C-band after frequency conversion of photons from remote quantum emitters”, *Nature Nanotechnology*, **14**, 23–26, (2019).

- [58] J.-H. Kim, C. J. K. Richardson, R. P. Leavitt, and E. Waks, “Two-Photon Interference from the Far-Field Emission of Chip-Integrated Cavity-Coupled Emitters”, *Nano Letters*, **16**, 7061–7066, (2016).
- [59] K. Takemoto, Y. Nambu, T. Miyazawa, Y. Sakuma, T. Yamamoto, S. Yorozu, and Y. Arakawa, “Quantum key distribution over 120 km using ultrahigh purity single-photon source and superconducting single-photon detectors.”, *Scientific reports*, **5**, 14383, (2015).
- [60] Z.-C. Duan, J.-P. Li, J. Qin, Y. Yu, Y.-H. Huo, S. Hoeffling, C. Lu, N. Liu, K. Chen, and J.-W. Pan, “Demonstration of compiled Shor’s quantum factoring algorithm using a quantum dot single-photon source”, *Optics Express*, **28**, 18917–18930, (2020).
- [61] J. C. Loredó, M. A. Broome, P. Hilaire, O. Gazzano, I. Sagnes, A. Lemaitre, M. P. Almeida, P. Senellart, and A. G. White, “Boson Sampling with Single-Photon Fock States from a Bright Solid-State Source”, *Physical Review Letters*, **118**, 130503, (2017).
- [62] H. Wang, Y.-M. He, Y.-H. Li, Z.-E. Su, B. Li, H.-L. Huang, X. Ding, M.-C. Chen, C. Liu, J. Qin, J.-P. Li, Y.-M. He, C. Schneider, M. Kamp, C.-Z. Peng, S. Höfling, C.-Y. Lu, and J.-W. Pan, “High-efficiency multiphoton boson sampling”, *Nature Photonics*, **11**, 361–365, (2017).
- [63] H. Wang, J. Qin, X. Ding, M. C. Chen, S. Chen, X. You, Y. M. He, X. Jiang, L. You, Z. Wang, C. Schneider, J. J. Renema, S. Höfling, C. Y. Lu, and J. W. Pan, “Boson Sampling with 20 Input Photons and a 60-Mode Interferometer in a 1014 -Dimensional Hilbert Space”, *Physical Review Letters*, **123**, 250503, (2019).
- [64] A. W. Elshaari, W. Pernice, K. Srinivasan, O. Benson, and V. Zwiller, “Hybrid integrated quantum photonic circuits”, *Nature Photonics*, **14**, 285–298, (2020).
- [65] J.-H. Kim, S. Aghaeimeibodi, J. Carolan, D. Englund, and E. Waks, “Hybrid integration methods for on-chip quantum photonics”, *Optica*, **7**, 291, (2020).
- [66] J. Lee, V. Leong, D. Kalashnikov, J. Dai, A. Gandhi, and L. A. Krivitsky, “Integrated single photon emitters”, *AVS Quantum Science*, **2**, 031701, (2020).
- [67] J. H. Kim, S. Aghaeimeibodi, C. J. Richardson, R. P. Leavitt, D. Englund, and E. Waks, “Hybrid Integration of Solid-State Quantum Emitters on a Silicon Photonic Chip”, *Nano Letters*, **17**, 7394–7400, (2017).

- [68] S. Aghaeimeibodi, B. Desiatov, J.-H. Kim, C.-M. Lee, M. A. Buyukkaya, A. Karasahin, C. J. K. Richardson, R. P. Leavitt, M. Lončar, and E. Waks, “Integration of quantum dots with lithium niobate photonics”, *Applied Physics Letters*, **113**, 221102, (2018).
- [69] M. Davanco, J. Liu, L. Sapienza, C.-Z. Zhang, J. V. De Miranda Cardoso, V. Verma, R. Mirin, S. W. Nam, L. Liu, and K. Srinivasan, “Heterogeneous integration for on-chip quantum photonic circuits with single quantum dot devices”, *Nature Communications*, **8**, 889, (2017).
- [70] I. E. Zadeh, A. W. Elshaari, K. D. Jöns, A. Fognini, D. Dalacu, P. J. Poole, M. E. Reimer, and V. Zwiller, “Deterministic Integration of Single Photon Sources in Silicon Based Photonic Circuits”, *Nano Letters*, **16**, 2289–2294, (2016).
- [71] P. Schnauber, A. Singh, J. Schall, S. I. Park, J. D. Song, S. Rodt, K. Srinivasan, S. Reitzenstein, and M. Davanco, “Indistinguishable Photons from Deterministically Integrated Single Quantum Dots in Heterogeneous GaAs/Si₃N₄ Quantum Photonic Circuits”, *Nano Letters*, **19**, 7164–7172, (2019).
- [72] A. W. Elshaari, I. E. Zadeh, A. Fognini, M. E. Reimer, D. Dalacu, P. J. Poole, V. Zwiller, and K. D. Jöns, “On-chip single photon filtering and multiplexing in hybrid quantum photonic circuits”, *Nature Communications*, **8**, 379, (2017).
- [73] Y. Arakawa and H. Sakaki, “Multidimensional quantum well laser and temperature dependence of its threshold current”, *Applied Physics Letters*, **40**, 939–941, (1982).
- [74] P. Michler, *Quantum dots for quantum information technologies*, volume 237, Springer, (2017).
- [75] E. M. Purcell, H. C. Torrey, and R. V. Pound, “Resonance absorption by nuclear magnetic moments in a solid”, *Physical review*, **69**, 37, (1946).
- [76] E. Yablonovitch, “Inhibited spontaneous emission in solid-state physics and electronics”, *Physical review letters*, **58**, 2059, (1987).
- [77] K. Sakoda, *Optical properties of photonic crystals*, volume 80, Springer Science & Business Media, (2004).
- [78] R. Loudon, *The quantum theory of light*, OUP Oxford, (2000).

- [79] M. Fox, *Quantum optics: an introduction*, volume 15, OUP Oxford, (2006).
- [80] R. H. Brown and R. Q. Twiss, “Correlation between photons in two coherent beams of light”, *Nature*, **177**, 27–29, (1956).
- [81] M. Davanço, C. S. Hellberg, S. Ates, A. Badolato, and K. Srinivasan, “Multiple time scale blinking in InAs quantum dot single-photon sources”, *Physical Review B*, **89**, 161303, (2014).
- [82] E. Menard, K. J. Lee, D.-Y. Khang, R. G. Nuzzo, and J. A. Rogers, “A printable form of silicon for high performance thin film transistors on plastic substrates”, *Applied Physics Letters*, **84**, 5398–5400, (2004).
- [83] M. A. Meitl, Z.-T. Zhu, V. Kumar, K. J. Lee, X. Feng, Y. Y. Huang, I. Adesida, R. G. Nuzzo, and J. A. Rogers, “Transfer printing by kinetic control of adhesion to an elastomeric stamp”, *Nature Materials*, **5**, 33–38, (2006).
- [84] A. Carlson, A. M. Bowen, Y. Huang, R. G. Nuzzo, and J. A. Rogers, “Transfer Printing Techniques for Materials Assembly and Micro/Nanodevice Fabrication”, *Advanced Materials*, **24**, 5284–5318, (2012).
- [85] J. Yoon, S. M. Lee, D. Kang, M. A. Meitl, C. A. Bower, and J. A. Rogers, “Heterogeneously Integrated Optoelectronic Devices Enabled by Micro-Transfer Printing”, *Advanced Optical Materials*, **3**, 1313–1335, (2015).
- [86] J. Zhang, G. Muliuk, J. Juvert, S. Kumari, J. Goyvaerts, B. Haq, C. Op de Beeck, B. Kuyken, G. Morthier, D. Van Thourhout, R. Baets, G. Lepage, P. Verheyen, J. Van Campenhout, A. Gocalinska, J. O’Callaghan, E. Pelucchi, K. Thomas, B. Corbett, A. J. Trindade, and G. Roelkens, “III-V-on-Si photonic integrated circuits realized using micro-transfer-printing”, *APL Photonics*, **4**, 110803, (2019).
- [87] X. Feng, M. A. Meitl, A. M. Bowen, Y. Huang, R. G. Nuzzo, and J. A. Rogers, “Competing Fracture in Kinetically Controlled Transfer Printing”, *Langmuir*, **23**, 12555–12560, (2007).
- [88] E. Waks and J. Vučković, “Coupled mode theory for photonic crystal cavity-waveguide interaction”, *Optics Express*, **13**, 5064, (2005).
- [89] E. Kuramochi, H. Taniyama, T. Tanabe, K. Kawasaki, Y.-G. Roh, and M. Notomi, “Ultrahigh- Q one-dimensional photonic crystal nanocavities with modulated mode-gap barriers on SiO₂ claddings and on air claddings”, *Optics Express*, **18**, 15859, (2010).

- [90] P. B. Deotare, M. W. McCutcheon, I. W. Frank, M. Khan, and M. Lončar, “High quality factor photonic crystal nanobeam cavities”, *Applied Physics Letters*, **94**, 121106, (2009).
- [91] R. Ohta, Y. Ota, M. Nomura, N. Kumagai, S. Ishida, S. Iwamoto, and Y. Arakawa, “Strong coupling between a photonic crystal nanobeam cavity and a single quantum dot”, *Applied Physics Letters*, **98**, 173104, (2011).
- [92] Y. Ota, R. Ohta, N. Kumagai, S. Iwamoto, and Y. Arakawa, “Vacuum Rabi Spectra of a Single Quantum Emitter”, *Physical Review Letters*, **114**, 143603, (2015).
- [93] Y. Halioua, A. Bazin, P. Monnier, T. J. Karle, G. Roelkens, I. Sagnes, R. Raj, and F. Raineri, “Hybrid III-V semiconductor/silicon nanolaser”, *Optics Express*, **19**, 9221, (2011).
- [94] Y. Xu, J. S. Vučković, R. K. Lee, O. J. Painter, A. Scherer, and A. Yariv, “Finite-difference time-domain calculation of spontaneous emission lifetime in a microcavity”, *Journal of the Optical Society of America B*, **16**, 465, (1999).
- [95] R. Ohta, *Fabrication of Tunable Q Photonic Crystal Nanobeam Cavities for the Control of Light Matter Interaction*, Doctoral thesis, The University of Tokyo, (2014).
- [96] A. Faraon, I. Fushman, D. Englund, N. Stoltz, P. Petroff, and J. Vuckovic, “Dipole induced transparency in waveguide coupled photonic crystal cavities”, *Optics Express*, **16**, 12154, (2008).
- [97] J. Justice, C. Bower, M. Meitl, M. B. Mooney, M. A. Gubbins, and B. Corbett, “Wafer-scale integration of group III–V lasers on silicon using transfer printing of epitaxial layers”, *Nature Photonics*, **6**, 610–614, (2012).
- [98] Y. Ota, S. Iwamoto, N. Kumagai, and Y. Arakawa, “Spontaneous Two-Photon Emission from a Single Quantum Dot”, *Physical Review Letters*, **107**, 233602, (2011).
- [99] K. Kuruma, Y. Ota, M. Kakuda, S. Iwamoto, and Y. Arakawa, “Surface-passivated high- Q GaAs photonic crystal nanocavity with quantum dots”, *APL Photonics*, **5**, 046106, (2020).

- [100] U. Hohenester, A. Laucht, M. Kaniber, N. Hauke, A. Neumann, A. Mottashami, M. Seliger, M. Bichler, and J. J. Finley, “Phonon-assisted transitions from quantum dot excitons to cavity photons”, *Physical Review B*, **80**, 201311, (2009).
- [101] S.-I. Park, Y. Xiong, R.-H. Kim, P. Elvikis, M. Meitl, D.-H. Kim, J. Wu, J. Yoon, C.-J. Yu, Z. Liu, Y. Huang, K.-c. Hwang, P. Ferreira, X. Li, K. Choquette, and J. A. Rogers, “Printed Assemblies of Inorganic Light-Emitting Diodes for Deformable and Semitransparent Displays”, *Science*, **325**, 977–981, (2009).
- [102] A. De Groote, P. Cardile, A. Z. Subramanian, A. M. Fecioru, C. Bower, D. Delbeke, R. Baets, and G. Roelkens, “Transfer-printing-based integration of single-mode waveguide-coupled III-V-on-silicon broadband light emitters”, *Optics Express*, **24**, 13754, (2016).
- [103] S. Mosor, J. Hendrickson, B. Richards, J. Sweet, G. Khitrova, H. Gibbs, T. Yoshie, A. Scherer, O. Shchekin, and D. Deppe, “Scanning a photonic crystal slab nanocavity by condensation of xenon”, *Applied Physics Letters*, **87**, 141105, (2005).
- [104] S. Bogdanov, M. Y. Shalaginov, A. Boltasseva, and V. M. Shalaev, “Material platforms for integrated quantum photonics”, *Optical Materials Express*, **7**, 111, (2017).
- [105] M. Hochberg and T. Baehr-Jones, “Towards fabless silicon photonics”, *Nature Photonics*, **4**, 492–494, (2010).
- [106] J. W. Silverstone, D. Bonneau, J. L. O’Brien, and M. G. Thompson, “Silicon Quantum Photonics”, *IEEE Journal of Selected Topics in Quantum Electronics*, **22**, 390–402, (2016).
- [107] J. C. Adcock, J. Bao, Y. Chi, X. Chen, D. Bacco, Q. Gong, L. K. Oxenlowe, J. Wang, and Y. Ding, “Advances in Silicon Quantum Photonics”, *IEEE Journal of Selected Topics in Quantum Electronics*, **27**, 1–24, (2021).
- [108] V. Scarani, H. Bechmann-Pasquinucci, N. J. Cerf, M. Dušek, N. Lütkenhaus, and M. Peev, “The security of practical quantum key distribution”, *Reviews of Modern Physics*, **81**, 1301–1350, (2009).

- [109] P. Sibson, C. Erven, M. Godfrey, S. Miki, T. Yamashita, M. Fujiwara, M. Sasaki, H. Terai, M. G. Tanner, C. M. Natarajan, R. H. Hadfield, J. L. O'Brien, and M. G. Thompson, "Chip-based quantum key distribution", *Nature Communications*, **8**, 13984, (2017).
- [110] J. Wang, S. Paesani, Y. Ding, R. Santagati, P. Skrzypczyk, A. Salavrakos, J. Tura, R. Augusiak, L. Mančinska, D. Bacco, D. Bonneau, J. W. Silverstone, Q. Gong, A. Acín, K. Rottwitt, L. K. Oxenløwe, J. L. O'Brien, A. Laing, and M. G. Thompson, "Multidimensional quantum entanglement with large-scale integrated optics", *Science*, **360**, 285–291, (2018).
- [111] E. Knill, R. Laflamme, and G. J. Milburn, "A Scheme for efficient Quantum Computation with linear optics", *Nature*, **409**, 46, (2001).
- [112] X. Qiang, X. Zhou, J. Wang, C. M. Wilkes, T. Loke, S. O'Gara, L. Kling, G. D. Marshall, R. Santagati, T. C. Ralph, J. B. Wang, J. L. O'Brien, M. G. Thompson, and J. C. F. Matthews, "Large-scale silicon quantum photonics implementing arbitrary two-qubit processing", *Nature Photonics*, **12**, 534–539, (2018).
- [113] D. Llewellyn, Y. Ding, I. I. Faruque, S. Paesani, D. Bacco, R. Santagati, Y.-J. Qian, Y. Li, Y.-F. Xiao, M. Huber, M. Malik, G. F. Sinclair, X. Zhou, K. Rottwitt, J. L. O'Brien, J. G. Rarity, Q. Gong, L. K. Oxenlowe, J. Wang, and M. G. Thompson, "Chip-to-chip quantum teleportation and multi-photon entanglement in silicon", *Nature Physics*, **16**, 148–153, (2020).
- [114] J. B. Spring, B. J. Metcalf, P. C. Humphreys, W. S. Kolthammer, X.-M. Jin, M. Barbieri, A. Datta, N. Thomas-Peter, N. K. Langford, D. Kundys, J. C. Gates, B. J. Smith, P. G. R. Smith, and I. A. Walmsley, "Boson Sampling on a Photonic Chip", *Science*, **339**, 798–801, (2013).
- [115] J. Leuthold, C. Koos, and W. Freude, "Nonlinear silicon photonics", *Nature Photonics*, **4**, 535–544, (2010).
- [116] T. Miyazawa, K. Takemoto, Y. Sakuma, S. Hirose, T. Usuki, N. Yokoyama, M. Takatsu, and Y. Arakawa, "Single-Photon Generation in the 1.55- μm Optical-Fiber Band from an InAs/InP Quantum Dot", *Japanese Journal of Applied Physics*, **44**, L620–L622, (2005).
- [117] M. Benyoucef, M. Yacob, J. P. Reithmaier, J. Kettler, and P. Michler, "Telecom-wavelength (1.5 μm) single-photon emission from InP-based quantum dots", *Applied Physics Letters*, **103**, 162101, (2013).

- [118] M. D. Birowosuto, H. Sumikura, S. Matsuo, H. Taniyama, P. J. van Veldhoven, R. Nötzel, and M. Notomi, “Fast Purcell-enhanced single photon source in 1,550-nm telecom band from a resonant quantum dot-cavity coupling”, *Scientific Reports*, **2**, 321, (2012).
- [119] K. D. Zeuner, M. Paul, T. Lettner, C. Reuterskiöld Hedlund, L. Schweickert, S. Steinhauer, L. Yang, J. Zichi, M. Hammar, K. D. Jöns, and V. Zwiller, “A stable wavelength-tunable triggered source of single photons and cascaded photon pairs at the telecom C-band”, *Applied Physics Letters*, **112**, 173102, (2018).
- [120] S. Kako, C. Santori, K. Hoshino, S. Götzinger, Y. Yamamoto, and Y. Arakawa, “A gallium nitride single-photon source operating at 200K”, *Nature Materials*, **5**, 887–892, (2006).
- [121] A. Dousse, L. Lanco, J. Suffczyński, E. Semenova, A. Miard, A. Lemaître, I. Sagnes, C. Roblin, J. Bloch, and P. Senellart, “Controlled Light-Matter Coupling for a Single Quantum Dot Embedded in a Pillar Microcavity Using Far-Field Optical Lithography”, *Physical Review Letters*, **101**, 267404, (2008).
- [122] P. Schnauber, J. Schall, S. Bounouar, T. Höhne, S.-I. Park, G.-H. Ryu, T. Heindel, S. Burger, J.-D. Song, S. Rodt, and S. Reitzenstein, “Deterministic Integration of Quantum Dots into on-Chip Multimode Interference Beamsplitters Using in Situ Electron Beam Lithography”, *Nano Letters*, **18**, 2336–2342, (2018).
- [123] A. Faraon, D. Englund, I. Fushman, J. Vučković, N. Stoltz, and P. Petroff, “Local quantum dot tuning on photonic crystal chips”, *Applied Physics Letters*, **90**, 213110, (2007).
- [124] A. Faraon and J. Vučković, “Local temperature control of photonic crystal devices via micron-scale electrical heaters”, *Applied Physics Letters*, **95**, 25–27, (2009).
- [125] A. W. Elshaari, E. Büyükközer, I. E. Zadeh, T. Lettner, P. Zhao, E. Schöll, S. Gyger, M. E. Reimer, D. Dalacu, P. J. Poole, K. D. Jöns, and V. Zwiller, “Strain-Tunable Quantum Integrated Photonics”, *Nano Letters*, **18**, 7969–7976, (2018).
- [126] Y. Chen, J. Zhang, M. Zopf, K. Jung, Y. Zhang, R. Keil, F. Ding, and O. G. Schmidt, “Wavelength-tunable entangled photons from silicon-integrated III–V quantum dots”, *Nature Communications*, **7**, 10387, (2016).

- [127] R. M. Stevenson, R. J. Young, P. Atkinson, K. Cooper, D. A. Ritchie, and A. J. Shields, “A semiconductor source of triggered entangled photon pairs”, *Nature*, **439**, 178–182, (2006).
- [128] M. Petruzzella, S. Birindelli, F. M. Pagliano, D. Pellegrino, Ž. Zobenica, L. H. Li, E. H. Linfield, and A. Fiore, “Quantum photonic integrated circuits based on tunable dots and tunable cavities”, *APL Photonics*, **3**, 106103, (2018).
- [129] R. B. Patel, A. J. Bennett, I. Farrer, C. A. Nicoll, D. A. Ritchie, and A. J. Shields, “Two-photon interference of the emission from electrically tunable remote quantum dots”, *Nature Photonics*, **4**, 632–635, (2010).
- [130] S. Aghaeimeibodi, C.-M. Lee, M. A. Buyukkaya, C. J. K. Richardson, and E. Waks, “Large stark tuning of InAs/InP quantum dots”, *Applied Physics Letters*, **114**, 071105, (2019).
- [131] J. H. Weber, B. Kambs, J. Kettler, S. Kern, J. Maisch, H. Vural, M. Jetter, S. L. Portalupi, C. Becher, and P. Michler, “Two-photon interference in the telecom C-band after frequency conversion of photons from remote quantum emitters”, *Nature Nanotechnology*, **14**, 23–26, (2019).
- [132] L. B. Soldano and E. C. M. Pennings, “Optical multi-mode interference devices based on self-imaging: principles and applications”, *Journal of Lightwave Technology*, **13**, 615–627, (1995).
- [133] D. Bonneau, E. Engin, K. Ohira, N. Suzuki, H. Yoshida, N. Iizuka, M. Ezaki, C. M. Natarajan, M. G. Tanner, R. H. Hadfield, S. N. Dorenbos, V. Zwiller, J. L. O’Brien, and M. G. Thompson, “Quantum interference and manipulation of entanglement in silicon wire waveguide quantum circuits”, *New Journal of Physics*, **14**, 045003, (2012).
- [134] T. Grange, N. Somaschi, C. Antón, L. De Santis, G. Coppola, V. Giesz, A. Lemaître, I. Sagnes, A. Auffèves, and P. Senellart, “Reducing Phonon-Induced Decoherence in Solid-State Single-Photon Sources with Cavity Quantum Electrodynamics”, *Physical Review Letters*, **118**, 253602, (2017).
- [135] A. Thoma, P. Schnauber, M. Gschrey, M. Seifried, J. Wolters, J.-H. Schulze, A. Strittmatter, S. Rodt, A. Carmele, A. Knorr, T. Heindel, and S. Reitzenstein, “Exploring Dephasing of a Solid-State Quantum Emitter via Time- and Temperature-Dependent Hong-Ou-Mandel Experiments”, *Physical Review Letters*, **116**, 033601, (2016).

- [136] J. Iles-Smith, D. P. S. McCutcheon, A. Nazir, and J. Mørk, “Phonon scattering inhibits simultaneous near-unity efficiency and indistinguishability in semiconductor single-photon sources”, *Nature Photonics*, **11**, 521–526, (2017).
- [137] Y. L. Loo, R. L. Willett, K. W. Baldwin, and J. A. Rogers, “Interfacial chemistries for nanoscale transfer printing”, *Journal of the American Chemical Society*, **124**, 7654–7655, (2002).
- [138] Y.-L. Loo, D. V. Lang, J. A. Rogers, and J. W. P. Hsu, “Electrical Contacts to Molecular Layers by Nanotransfer Printing”, *Nano Letters*, **3**, 913–917, (2003).
- [139] D. Cadeddu, J. Teissier, F. R. Braakman, N. Gregersen, P. Stepanov, J.-M. Gérard, J. Claudon, R. J. Warburton, M. Poggio, and M. Munsch, “A fiber-coupled quantum-dot on a photonic tip”, *Applied Physics Letters*, **108**, 011112, (2016).
- [140] A. Schlehahn, S. Fischbach, R. Schmidt, A. Kaganskiy, A. Strittmatter, S. Rodt, T. Heindel, and S. Reitzenstein, “A stand-alone fiber-coupled single-photon source”, *Scientific Reports*, **8**, 1340, (2018).
- [141] A. Musiał, K. Żołnacz, N. Srocka, O. Kravets, J. Große, J. Olszewski, K. Poturaj, G. Wójcik, P. Mergo, K. Dybka, M. Dyrkacz, M. Dłubek, K. Lauritsen, A. Bültner, P. Schneider, L. Zschiedrich, S. Burger, S. Rodt, W. Urbančzyk, G. Sęk, and S. Reitzenstein, “Plug&Play Fiber-Coupled 73 kHz Single-Photon Source Operating in the Telecom O - Band”, *Advanced Quantum Technologies*, **3**, 2000018, (2020).
- [142] L. Bremer, K. Weber, S. Fischbach, S. Thiele, M. Schmidt, A. Kaganskiy, S. Rodt, A. Herkommer, M. Sartison, S. L. Portalupi, P. Michler, H. Giessen, and S. Reitzenstein, “Quantum dot single-photon emission coupled into single-mode fibers with 3D printed micro-objectives”, *APL Photonics*, **5**, 106101, (2020).
- [143] M. Davano, M. T. Rakher, W. Wegscheider, D. Schuh, A. Badolato, and K. Srinivasan, “Efficient quantum dot single photon extraction into an optical fiber using a nanophotonic directional coupler”, *Applied Physics Letters*, **99**, 6–9, (2011).
- [144] R. S. Daveau, K. C. Balram, T. Pregmolato, J. Liu, E. H. Lee, J. D. Song, V. Verma, R. Mirin, S. W. Nam, L. Midolo, S. Stobbe, K. Srinivasan, and

- P. Lodahl, “Efficient fiber-coupled single-photon source based on quantum dots in a photonic-crystal waveguide”, *Optica*, **4**, 178, (2017).
- [145] C.-M. Lee, M. A. Buyukkaya, S. Aghaeimeibodi, A. Karasahin, C. J. K. Richardson, and E. Waks, “A fiber-integrated nanobeam single photon source emitting at telecom wavelengths”, *Applied Physics Letters*, **114**, 171101, (2019).
- [146] M. Pu, L. Liu, H. Ou, K. Yvind, and J. M. Hvam, “Ultra-low-loss inverted taper coupler for silicon-on-insulator ridge waveguide”, *Optics Communications*, **283**, 3678–3682, (2010).
- [147] M. Wood, P. Sun, and R. M. Reano, “Compact cantilever couplers for low-loss fiber coupling to silicon photonic integrated circuits”, *Optics Express*, **20**, 164, (2012).
- [148] Y. Juang, Y. Su, S. Shei, and B. Fang, “Comparing reactive ion etching of III–V compounds in $\text{Cl}_2/\text{BCl}_3/\text{Ar}$ and $\text{CCl}_2\text{F}_2/\text{BCl}_3/\text{Ar}$ discharges”, *Journal of Vacuum Science & Technology A: Vacuum, Surfaces, and Films*, **12**, 75–82, (1994).
- [149] K. Lee, S. Guilet, G. Patriarche, I. Sagnes, and A. Talneau, “Smooth sidewall in InP-based photonic crystal membrane etched by N_2 -based inductively coupled plasma”, *Journal of Vacuum Science & Technology B: Microelectronics and Nanometer Structures Processing, Measurement, and Phenomena*, **26**, 1326–1333, (2008).
- [150] K. H. Lee, S. Guilet, G. Patriarche, I. Sagnes, and A. Talneau, “Smooth sidewall in InP-based photonic crystal membrane etched by N_2 -based inductively coupled plasma”, *Journal of Vacuum Science and Technology B: Microelectronics and Nanometer Structures*, **26**, 1326–1333, (2008).
- [151] Y. Toda, O. Moriwaki, M. Nishioka, and Y. Arakawa, “Efficient Carrier Relaxation Mechanism in InGaAs/GaAs Self-Assembled Quantum Dots Based on the Existence of Continuum States”, *Physical Review Letters*, **82**, 4114–4117, (1999).
- [152] C. Santori, D. Fattal, J. Vučković, G. S. Solomon, E. Waks, and Y. Yamamoto, “Submicrosecond correlations in photoluminescence from InAs quantum dots”, *Physical Review B*, **69**, 205324, (2004).

- [153] H. Wang, Y.-M. He, T.-H. Chung, H. Hu, Y. Yu, S. Chen, X. Ding, M.-C. Chen, J. Qin, X. Yang, R.-Z. Liu, Z.-C. Duan, J.-P. Li, S. Gerhardt, K. Winkler, J. Jurkat, L.-J. Wang, N. Gregersen, Y.-H. Huo, Q. Dai, S. Yu, S. Höfling, C.-Y. Lu, and J.-W. Pan, “Towards optimal single-photon sources from polarized microcavities”, *Nature Photonics*, **13**, 770–775, (2019).
- [154] T. Huber, M. Davanço, M. Müller, Y. Shuai, O. Gazzano, G. S. Solomon, M. Davanco, M. Müller, Y. Shuai, O. Gazzano, and G. S. Solomon, “Filter-free single-photon quantum dot resonance fluorescence in an integrated cavity-waveguide device”, *Optica*, **7**, 380, (2020).
- [155] S. Ates, S. M. Ulrich, S. Reitzenstein, A. Löffler, A. Forchel, and P. Michler, “Post-Selected Indistinguishable Photons from the Resonance Fluorescence of a Single Quantum Dot in a Microcavity”, *Physical Review Letters*, **103**, 167402, (2009).
- [156] O. Gazzano, S. M. De Vasconcellos, C. Arnold, A. Nowak, E. Galopin, I. Sagnes, L. Lanco, A. Lemaître, and P. Senellart, “Bright solid-state sources of indistinguishable single photons”, *Nature communications*, **4**, 1–6, (2013).
- [157] C. Simon, M. Afzelius, J. Appel, A. B. de La Giroday, S. Dewhurst, N. Gisin, C. Hu, F. Jelezko, S. Kröll, J. Müller, et al., “Quantum memories”, *The European Physical Journal D*, **58**, 1–22, (2010).
- [158] A. Javadi, I. Söllner, M. Arcari, S. L. Hansen, L. Midolo, S. Mahmoodian, G. Kiršanskė, T. Pregonato, E. H. Lee, J. D. Song, S. Stobbe, and P. Lodahl, “Single-photon non-linear optics with a quantum dot in a waveguide”, *Nature Communications*, **6**, 8655, (2015).
- [159] L. De Santis, C. Antón, B. Reznichenko, N. Somaschi, G. Coppola, J. Senellart, C. Gómez, A. Lemaître, I. Sagnes, A. G. White, L. Lanco, A. Auffèves, and P. Senellart, “A solid-state single-photon filter”, *Nature Nanotechnology*, **12**, 663–667, (2017).
- [160] F. Najafi, J. Mower, N. C. Harris, F. Bellei, A. Dane, C. Lee, X. Hu, P. Kharel, F. Marsili, S. Assefa, K. K. Berggren, and D. Englund, “On-chip detection of non-classical light by scalable integration of single-photon detectors”, *Nature Communications*, **6**, 5873, (2015).
- [161] S. L. Mouradian, T. Schröder, C. B. Poitras, L. Li, J. Goldstein, E. H. Chen, M. Walsh, J. Cardenas, M. L. Markham, D. J. Twitchen, M. Lipson, and

- D. Englund, “Scalable Integration of Long-Lived Quantum Memories into a Photonic Circuit”, *Physical Review X*, **5**, 031009, (2015).
- [162] A. Osada, Y. Ota, R. Katsumi, M. Kakuda, S. Iwamoto, and Y. Arakawa, “Strongly coupled single-quantum-dot–cavity system integrated on a CMOS-processed silicon photonic chip”, *Physical Review Applied*, **11**, 024071, (2019).
- [163] N. Ahmed, A. Carlson, J. A. Rogers, and P. M. Ferreira, “Automated micro-transfer printing with cantilevered stamps”, *Journal of Manufacturing Processes*, **14**, 90–97, (2012).
- [164] S. Masubuchi, M. Morimoto, S. Morikawa, M. Onodera, Y. Asakawa, K. Watanabe, T. Taniguchi, and T. Machida, “Autonomous robotic searching and assembly of two-dimensional crystals to build van der Waals superlattices”, *Nature Communications*, **9**, 4–6, (2018).
- [165] J. McPhillimy, D. Jevtics, B. J. Guilhabert, C. Klitis, A. Hurtado, M. Sorel, M. D. Dawson, and M. J. Strain, “Automated nanoscale absolute accuracy alignment system for transfer printing”, *ACS applied nano materials*, **3**, 10326–10332, (2020).
- [166] H.-S. Zhong, H. Wang, Y.-H. Deng, M.-C. Chen, L.-C. Peng, Y.-H. Luo, J. Qin, D. Wu, X. Ding, Y. Hu, et al., “Quantum computational advantage using photons”, *Science*, **370**, 1460–1463, (2020).

Research achievement

International Journal

- [1] **R. Katsumi**, Y. Ota, M. Kakuda, S. Iwamoto, and Y. Arakawa, “Transfer-printed single-photon sources coupled to wire waveguides”, *Optica* **5**, 691-694 (2018).

**This article is selected as “Top-Cited Articles on Quantum Information from Optica”.*

- [2] **R. Katsumi**, Y. Ota, A. Osada, T. Yamaguchi, T. Tajiri, M. Kakuda, S. Iwamoto, H. Akiyama, and Y. Arakawa, “Quantum-dot single-photon source on a CMOS silicon photonic chip integrated using transfer printing”, *APL Photonics* **4**, 036105 (2019).

**This article is selected as “Featured Article”, and also highlighted in Scilight.*

- [3] **R. Katsumi**, Y. Ota, A. Osada, T. Tajiri, T. Yamaguchi, M. Kakuda, S. Iwamoto, H. Akiyama, and Y. Arakawa, “In-situ wavelength tuning of quantum-dot single-photon sources integrated on a CMOS-processed silicon waveguide”, *Appl. Phys. Lett.* **116**, 041103 (2020).

**This article is selected as “Editor’s Pick”.*

International Conference and Workshop

- [1] **R. Katsumi**, Y. Ota, K. Kuruma, A. Tamada, M. Kakuda, T. Miyazawa, K. Takemoto, S. Iwamoto, and Y. Arakawa, “Quantum dot-nanocavity-waveguide coupled systems fabricated by transfer printing”, International Conference on

Nano-photonics and Nano-optoelectronics (ICNN2017), ICNN1-2, Yokohama, Japan, April (2017).

- [2] **R. Katsumi**, Y. Ota, K. Kuruma, A. Tamada, M. Kakuda, T. Miyazawa, K. Takemoto, S. Iwamoto, and Y. Arakawa, “Fabrication of quantum dot-nanocavity-waveguide coupled systems via transfer printing method”, International Nano-Optoelectronics Workshop (iNOW2017), WeP8, Tianjin-Qian’an-Chengde, China, August (2017).

**This poster was selected as First Prize Best Poster Award.*

- [3] **R. Katsumi**, Y. Ota, M. Kakuda, T. Miyazawa, K. Takemoto, S. Iwamoto, and Y. Arakawa, “Observation of optical coupling in a quantum dot-nanocavity-waveguide coupled system fabricated by transfer printing”, International Symposium on Photonics and Electronics Convergence (ISPEC2017), P-43, Komaba, Japan, December (2017).
- [4] **R. Katsumi**, Y. Ota, M. Kakuda, S. Iwamoto, and Y. Arakawa, “Transfer-printed Quantum-dot Single Photon Sources for Efficient Waveguide Coupling”, International Conference on Nano-photonics and Nano-optoelectronics (ICNN2018), ICNN1-2, Yokohama, Japan, April (2018).
- [5] **R. Katsumi**, Y. Ota, M. Kakuda, S. Iwamoto, and Y. Arakawa, “Quantum dot single photon sources transfer-printed on wire waveguides”, Conference on Lasers and Electro-Optics (CLEO 2018), FM1H.5., San Jose, USA, May (2018).
- [6] **R. Katsumi**, Y. Ota, M. Kakuda, S. Iwamoto, and Y. Arakawa, “Integration of multiple quantum-dot single-photon sources on a photonic waveguide by transfer printing”, 10th Biannual Conference on Quantum Dots (QD 2018), Mo3-03, Toronto, Canada, June (2018).
- [7] **R. Katsumi**, Y. Ota, A. Osada, T. Yamaguchi, T. Tajiri, M. Kakuda, S. Iwamoto, and Y. Arakawa, “Quantum-dot single-photon source transfer-

printed on a CMOS-processed silicon waveguide”, Conference on Lasers and Electro-Optics (CLEO 2019), FM1M.2, San Jose, USA, May (2019).

****The author was selected as the finalists of Maiman Student Paper Competition.***

- [8] **R. Katsumi**, Y. Ota, M. Kakuda, S. Iwamoto, and Y. Arakawa, “Quantum-dot-based single-photon source on a photonic waveguide integrated using transfer printing”, Frontiers in Quantum Materials and Devices workshops (FQMD 2019), P-8, Komaba, Japan, December (2019).

- [9] **R. Katsumi**, Y. Ota, A. Osada, T. Yamaguchi, T. Tajiri, M. Kakuda, S. Iwamoto, and Y. Arakawa, “Local tuning of transfer-printed quantum-dot single-photon sources on a CMOS silicon chip”, Microoptics Conference (MOC2019), Toyama, Japan, November (2019).

****This presentation was selected as Poster Award.***

- [10] **R. Katsumi**, Y. Ota, A. Osada, T. Yamaguchi, T. Tajiri, M. Kakuda, S. Iwamoto, and Y. Arakawa, “Hybrid integration of a quantum-dot single-photon emitter on a CMOS-processed Si waveguide using transfer printing”, International Symposium on Photonics and Electronics Convergence (ISPEC2019), P-30, Komaba, Japan, December (2019).

- [11] **R. Katsumi**, “Quantum-dot single-photon sources transfer-printed on a CMOS Si photonic chip”, The 1st SNU-UT Workshop on Nanophotonics, Seoul National University, Seoul, Korea, January (2020).

- [12] **R. Katsumi**, Y. Ota, T. Tajiri, M. Kakuda, S. Iwamoto, H. Akiyama and Y. Arakawa, “Efficient single photon sources transfer-printed on Si with unidirectional light output”, Conference on Lasers and Electro-Optics (CLEO 2020), FF2D.3, San Jose, USA, May (2020).

Domestic conference

- [1] **勝見亮太**, 太田泰友, 車一宏, 玉田晃均, 角田雅弘, 宮澤俊之, 竹本一矢, 岩本敏, 荒川泰彦, “転写プリント法による量子ドット-ナノ共振器-細線導波路結合系の作製とその評価”, 第64回応用物理学会春季学術講演会 (横浜パシフィコ), 15a-E205-12, 2017年3月

- [2] **勝見亮太**, 太田泰友, 角田雅弘, 宮澤俊之, 竹本一矢, 岩本敏, 荒川泰彦, “量子ドット-ナノ共振器-細線導波路結合系における単一光子発生の観測”, 第78回応用物理学会秋季学術講演会 (福岡国際会議場), 6p-A405-5, 2017年9月

- [3] **勝見亮太**, 太田泰友, 角田雅弘, 岩本敏, 荒川泰彦, “転写プリント法による量子ドット単一光子源の複数集積”, 第65回応用物理学会春季学術講演会 (早稲田大学・西早稲田キャンパス), 18p-A402-4, 2018年3月

- [4] **勝見亮太**, 太田泰友, 長田有登, 田尻武義, 車一宏, 山口拓人, 角田雅弘, 岩本敏, 秋山英文, 荒川泰彦, “転写プリント法によるシリコン導波路上への量子ドット単一光子源の集積”, 第79回応用物理学会秋季学術講演会 (名古屋国際会議場), 21a-143-3, 2018年9月

- [5] **勝見亮太**, 太田泰友, 長田有登, 田尻武義, 車一宏, 山口拓人, 角田雅弘, 岩本敏, 秋山英文, 荒川泰彦, “Si光回路上に集積された複数量子ドット光源の局所発光波長制御”, 第66回応用物理学会春季学術講演会 (東京工業大学), 12a-W631-6, 2019年3月

- [6] **勝見亮太**, 太田泰友, 岩本敏, 秋山英文, 荒川泰彦, “一方向出射が可能なSi光導波路集積型量子ドット単一光子源の設計”, 第80回応用物理学会秋季学術講演会 (北海道大学), 19a-E208-2, 2019年9月

- [7] **勝見亮太**, 太田泰友, 田尻武義, 角田雅弘, 岩本敏, 秋山英文, 荒川泰彦, “一方向出射が可能なSi上集積量子ドット単一光子源の作製と評価”, 第67回応用物理学会春季学術講演会 (上智大学), 14p-B415-10, 2020年3月

- [8] 勝見亮太, 太田泰友, 田尻武義, 岩本敏, 秋山英文, J. P. Reithmaier, M. Benyoucef, 荒川泰彦, “転写プリント法による通信波長帯量子ドット単一光子源のSi導波路上集積”, 第81回応用物理学会秋季学術講演会 (同志社大学), 10a-Z18-1, 2020年9月

Related of Publication

International Journal

- [1] A. Osada, Y. Ota, **R. Katsumi**, K. Watanabe, S. Iwamoto, and Y. Arakawa, “Transfer-printed quantum-dot nanolasers on a silicon photonic circuit”, *Appl. Phys. Express* **11**, 072002 (2018).
- [2] Y. Ota, **R. Katsumi**, K. Watanabe, S. Iwamoto, and Y. Arakawa, “Topological photonic crystal nanocavity laser”, *Commun. Phys.* **1**, 86 (2018).
- [3] A. Osada, Y. Ota, **R. Katsumi**, M. Kakuda, S. Iwamoto, and Y. Arakawa, “Strongly coupled single quantum dot-cavity system integrated on a CMOS-processed silicon photonic chip”, *Phys. Rev. Appl.* **11**, 024071 (2019).
- [4] Y. Ota, F. Liu, **R. Katsumi**, K. Watanabe, K. Wakabayashi, Y. Arakawa, and S. Iwamoto, “Photonic crystal nanocavity based on a topological corner state”, *Optica* **6**, 786-789 (2019).
- [5] T. Yamaguchi, Y. Ota, **R. Katsumi**, K. Watanabe, S. Ishida, A. Osada, Y. Arakawa and S. Iwamoto, “GaAs valley photonic crystal waveguide with light-emitting InAs quantum dots”, *Appl. Phys. Express* **12**, 62005 (2019).

International Conference and Workshop

- [1] S. Iwamoto, I. Kim, Y. Ota, **R. Katsumi**, and Y. Arakawa, “Topological Localized States in Quasi-1D Photonic and Phononic Crystals”, International workshop “Variety and universality of bulk-edge correspondence in topological phases: From solid state physics to transdisciplinary concepts” (BEC2018), Tsukuba Univ., Ibaraki, Japan, January (2018).

-
- [2] A. Osada, Y. Ota, **R. Katsumi**, K. Watanabe, S. Iwamoto, and Y. Arakawa, “Quantum-Dot Nanolaser Integrated on a Silicon Waveguide Buried in Silicon Dioxide by Transfer Printing”, International Conference on Nano-photonics and Nano-optoelectronics (ICNN2018), Pacico Yokohama, Japan, April (2018).
 - [3] Y. Ota, **R. Katsumi**, K. Watanabe, S. Iwamoto, and Y. Arakawa, “Lasing in a topological photonic crystal nanocavity”, Conference on Lasers and Electro-Optics (CLEO 2018), San Jose, USA, May (2018).
 - [4] A. Osada, Y. Ota, **R. Katsumi**, K. Watanabe, S. Iwamoto, and Y. Arakawa, “Quantum-dot nanolasers on Si photonic circuits”, Conference on Lasers and Electro-Optics (CLEO 2018), San Jose, USA, May (2018).
 - [5] S. Iwamoto, Y. Ota, **R. Katsumi**, K. Watanabe, and Y. Arakawa, “Topological Localized State in Photonic Crystal Nanobeam”, Progress In Electromagnetics Research Symposium (PIERS2018), Toyama, Japan, August (2018).
 - [6] Y. Ota, **R. Katsumi**, A. Osada, M. Kakuda, S. Iwamoto, and Y. Arakawa, “Chip-integrated Quantum-dot Single Photon Sources Fabricated by Transfer Printing”, Progress In Electromagnetics Research Symposium (PIERS2018), Toyama, Japan, August (2018).
 - [7] A. Osada, Y. Ota, **R. Katsumi**, K. Watanabe, S. Iwamoto, and Y. Arakawa, “Transfer-printed quantum-dot nanolasers on a silicon waveguide”, International Nano-Optoelectronics Workshop (iNOW2018), Berkeley, USA, August (2018).
 - [8] T. Yamaguchi, **R. Katsumi**, A. Osada, Y. Ota, S. Ishida, S. Iwamoto, and Y. Arakawa, “Observation of topologically protected light propagation in a slab-type valley photonic crystal waveguide”, Microoptics Conference (MOC2018), Taipei, Taiwan, October (2018).
 - [9] S. Iwamoto, Y. Ota, K. Kuruma, T. Tajiri, S. Takahashi, **R. Katsumi**, M. Kakuda, K. Watanabe, and Y. Arakawa, “Tailored disorders in photonic crys-

- tals for laser and cavity QED applications”, The 2018 Fall Meeting of the Materials Research Society (MRS2018), Boston, USA, November (2018).
- [10] A. Osada, Y. Ota, **R. Katsumi**, T. Yamaguchi, M. Kakuda, S. Iwamoto, and Y. Arakawa, “On-chip excitation of single quantum dots using a silicon waveguide”, International Symposium on Photonics and Electronics Convergence (ISPEC2018), Komaba, Japan, December (2018).
- [11] Y. Ota, **R. Katsumi**, K. Watanabe, S. Iwamoto, and Y. Arakawa, “Demonstration of a Topological Photonic Crystal Nanocavity Laser with Quantum Dot Gain”, International Symposium on Photonics and Electronics Convergence (ISPEC2018), Komaba, Japan, December (2018).
- [12] T. Yamaguchi, Y. Ota, **R. Katsumi**, S. Ishida, A. Osada, S. Iwamoto, and Y. Arakawa, “Observation of light propagation through sharp bends in a slab-type valley photonic crystal waveguide”, International Symposium on Photonics and Electronics Convergence (ISPEC2018), Komaba, Japan, December (2018).
- [13] B. Y. Jang, Y. Ota, **R. Katsumi**, J. K. Kwoen, N. Morais, and Y. Arakawa, “Demonstration of a Quantum Dot Laser on Silicon using Transfer Printing”, 8th international symposium on photonics and electronics convergence (ISPEC 2018), Tokyo, Japan, December (2018).
- [14] T. Yamaguchi, Y. Ota, **R. Katsumi**, A. Osada, S. Ishida, Y. Arakawa, and S. Iwamoto, “Observation of light transmission in a GaAs slab valley photonic crystal waveguide with sharp bends”, International workshop “Variety and universality of bulk-edge correspondence in topological phases: From solid state physics to transdisciplinary concepts” (BEC2018X), Tokyo, Japan, December (2018).
- [15] Y. Ota, **R. Katsumi**, K. Watanabe, F. Liu, K. Wakabayashi, S. Iwamoto, and Y. Arakawa, “Nanocavity based on a topological corner state in a two-dimensional photonic crystal”, Conference on Lasers and Electro-Optics (CLEO 2019), SW4J.1., San Jose, USA, May (2019).

- [16] A. Osada, Y. Ota, **R. Katsumi**, M. Kakuda, S. Iwamoto, and Y. Arakawa, “Strongly-coupled single quantum dot-cavity system on a silicon waveguide”, International Conference on Nano-photonics and Nano-optoelectronics (ICNN2019), Pacico Yokohama, Japan, April (2019).
- [17] Y. Ota, F. Liu, **R. Katsumi**, K. Watanabe, K. Wakabayashi, Y. Arakawa, and S. Iwamoto, “Observation of a topological corner state in a two-dimensional photonic crystal in the optical regime”, International Workshop on New Trends in Topological Insulators 2019 & Variety and Universality of Bulk-edge Correspondence in Topological Phases (NTTI2019 and BEC2019), PP-26, Hiroshima, Japan, July (2019).
- [18] Y. Ota, **R. Katsumi**, A. Osada, M. Kakuda, S. Iwamoto, and Y. Arakawa, “Hybrid integration of quantum/classical light sources on Si using transfer printing”, 2019 International Conference on Solid State Devices and Materials (SSDM2019), B-1-01, Nagoya, Japan, September (2019).
- [19] Y. Ota, **R. Katsumi**, A. Osada, M. Kakuda, S. Iwamoto, and Y. Arakawa, “Hybrid integration of quantum dot-nanocavity systems on silicon”, Frontiers in Optics + Laser Science APS/DLS, FM3D.4, Washington, DC, USA, September (2019).
- [20] Y. Ota, F. Liu, **R. Katsumi**, K. Watanabe, K. Wakabayashi, Y. Arakawa, and S. Iwamoto, “Light Trapping in a Higher-Order Topological Corner State”, The 9th International Symposium on Photonics and Electronics Convergence-Advanced Nanophotonics and Silicon Device Systems-(ISPEC2019), P-28, Tokyo, Japan, November (2019).
- [21] Y. Ota, **R. Katsumi**, A. Osada, M. Kakuda, S. Iwamoto, and Y. Arakawa, “Hybrid-integrated silicon quantum photonics toward scalable photonic quantum information processing”, The 42nd Photonics & Electromagnetics Research Symposium (PIERS) in Xiamen, Xiamen, China, December (2019).
- [22] H.Yoshimi, T.Yamaguchi, R.Katsumi, Y.Ota, Y.Arakawa, and S.Iwamoto, “Slow Light Waveguide Based on Topological Edge States in Valley Photonic

Crystals”, Conference on Lasers and Electro-Optics (CLEO), San Jose, USA, May (2020).

Domestic conference

- [1] 太田泰友, 勝見亮太, 渡邊克之, 岩本敏, 荒川泰彦, “トポロジカル 1 次元ナノビームフォトリック結晶共振器の作製と評価”, 第 78 回応用物理学会秋季学術講演会 (福岡国際会議場) (2017).
- [2] 長田有登, 勝見亮太, 角田雅弘, 太田泰友, 岩本敏, 荒川泰彦, “量子光回路応用に向けた量子ドットのオンチップ光励起の検討”, 第 78 回応用物理学会秋季学術講演会 (福岡国際会議場) (2017).
- [3] 不破麻里亜, 田尻武義, 勝見亮太, 石田丈, 玉田晃均, 渡邊克之, 太田泰友, 岩本敏, 荒川泰彦, “転写プリント法を用いたフォトリックナノ構造の作製と評価”, 第 78 回応用物理学会秋季学術講演会 (福岡国際会議場) (2017).
- [4] 岩本敏, 太田泰友, 勝見亮太, 荒川泰彦, “一次元ナノビームフォトリック結晶におけるトポロジカル局在状態”, 新学術領域「ハイブリッド量子科」第 6 回領域会議 (NTT 物性科学基礎研究所) (2018).
- [5] 太田泰友, 勝見亮太, 渡邊克之, 岩本敏, 荒川泰彦, “トポロジカル 1 次元フォトリック結晶ナノ共振器におけるレーザ発振”, 第 65 回応用物理学会春季学術講演会 (早稲田大学・西早稲田キャンパス) (2018).
- [6] 長田有登, 太田泰友, 勝見亮太, 角田雅弘, 岩本敏, 荒川泰彦, “転写プリント法によるシリコン導波路結合型量子ドットナノレーザの実現”, 第 65 回応用物理学会春季学術講演会 (早稲田大学・西早稲田キャンパス) (2018).
- [7] 山口拓人, 勝見亮太, 長田有登, 太田泰友, 石田悟己, 岩本敏, 荒川泰彦, “三角形状空気孔を有するバレーフォトリック結晶の作製と評価”, 第 65 回応用物理学会春季学術講演会 (早稲田大学・西早稲田キャンパス) (2018).

- [8] 長田有登, 太田泰友, **勝見亮太**, 角田雅弘, 岩本敏, 荒川泰彦, “ シリコン光回路上に集積された量子ドットナノ共振器強結合系の実現”, 第 79 回応用物理学会秋季学術講演会 (名古屋国際会議場) (2018).
- [9] 山口拓人, **勝見亮太**, 長田有登, 太田泰友, 石田悟己, 荒川泰彦, 岩本敏, “急峻曲げを有するスラブ型バレーフォトンニック結晶導波路における光伝搬の観測”, 第 79 回応用物理学会秋季学術講演会 (名古屋国際会議場) (2018).
- [10] 張奉鎔, 太田泰友, **勝見亮太**, 權晋寛, 荒川泰彦, “転写プリント法により作製したシリコン基板上電流注入型量子ドットレーザ”, 第 79 回応用物理学会秋季学術講演会 (名古屋国際会議場) (2018).
- [11] 太田泰友, Feng Liu, **勝見亮太**, 渡邊克之, 若林克法, 荒川泰彦, 岩本敏, “トポロジカルコーナー状態によるフォトンニック結晶ナノ共振器の実現”, 第 66 回応用物理学会春季学術講演会 (東京工業大学) (2019).
- [12] 吉見拓展, 山口拓人, **勝見亮太**, 太田泰友, 荒川泰彦, 岩本敏, “ バレーフォトンニック結晶 Bearded 界面によるスローライト導波路”, 新学術領域「ハイブリッド量子科学」第 9 回領域会議 (北陸先端科学技術大学院大学) (2019).
- [13] 太田泰友, 山口拓人, 吉見拓展, **勝見亮太**, 渡邊克之, 荒川泰彦, 岩本 敏, “アクティブ材料を融合した集積トポロジカルフォトンクス”, 電子情報通信学会ソサイエティ大会 (大阪大学) (2019).
- [14] 太田泰友, **勝見亮太**, 長田有登, 玉田晃均, 角田雅弘, 岩本敏, 荒川 泰彦, “ハイブリッド集積シリコン量子フォトンクスの可能性”, 第 80 回応用物理学会秋季学術講演会 (北海道大学) (2019).
- [15] 吉見拓展, 山口拓人, **勝見亮太**, 太田泰友, 荒川泰彦, 岩本敏, “ バレーフォトンニック結晶 Bearded 界面導波路における光伝搬の観測”, 第 80 回応用物理学会秋季学術講演会 (北海道大学) (2019).

- [16] 吉見拓展, 山口拓人, 勝見亮太, 太田泰友, 荒川泰彦, 岩本敏, “Si バレーフォトリック結晶 Bearded 界面導波路における光伝搬の観測”, 第3回電子材料若手交流会研究(つくばセミナーハウス) (2019).
- [17] 吉見拓展, 山口拓人, 勝見亮太, 太田泰友, 荒川泰彦, 岩本敏, “バレーフォトリック結晶におけるスローライトエッジ状態の光伝搬の観測”, 第67回応用物理学会春季学術講演会(上智大学) (2020).
- [18] 吉見拓展, 山口拓人, 勝見亮太, 太田泰友, 荒川泰彦, 岩本敏, “Si スラブバレーフォトリック結晶スローライトエッジ状態における群屈折率評価” KOSEN SC 第2回 VR 学術講演会(オンライン)(2020).
- [19] 吉見拓展, 山口拓人, 勝見亮太, 太田泰友, 荒川泰彦, 岩本敏, “バレーフォトリック結晶スローライトエッジ状態の観測”, 第5回フォトリックスワークショップ「光の多様性を探求する」(オンライン) (2020).
- [20] 吉見拓展, 山口拓人, 勝見亮太, 太田泰友, 荒川泰彦, 岩本敏, “トポロジカルバレーフォトリック結晶スローライト導波路における群屈折率評価”, 第3回結晶工学×ISYSE 合同研究会「コロナ下・コロナ禍でも進める研究活動・就職活動」(オンライン) (2020).

Patent

- [1] 宮澤俊之, 太田泰友, 勝見亮太, 竹本一矢, 高津求, 荒川泰彦, 岩本敏, “光デバイス及びその製造方法” 特開 2019-39984